https://doi.org/10.1070/RCR4979

Electrode materials based on complex d-metal oxides for symmetrical solid oxide fuel cells

Sergey Ya. Istomin,[a, b]* Nikolay V. Lyskov,[c] Galina N. Mazo,[a] Evgeny V. Antipov [a]

[a] *Department of Chemistry, Lomonosov Moscow State University, Leninskie Gory 1, stroenie 3, 119992 Moscow, Russian Federation*
[b] *HSE University, ul. Myasnitskaya 20, 101000 Moscow, Russian Federation*
[c] *Institute of Problems of Chemical Physics, Russian Academy of Sciences, prosp. Akademika Semenova 1, Chernogolovka, 142432 Moscow Region, Russian Federation*

The review addresses and highlights the main results of research on the physicochemical properties of single-phase and composite materials based on transition metal oxides in relation to their practical application as electrode materials for symmetrical solid oxide fuel cells. The electronic structures and thermodynamic stability of transition metal oxides with the perovskite structure are discussed. A detailed consideration is given to the thermal behaviour, chemical stability, electrical conductivity and electrochemical properties of a broad range of electrode materials based on iron-, chromium- and manganese-containing perovskite-like oxides and oxides that crystallize in other structure types. The analysis revealed the most promising compositions of electrode materials for symmetrical solid oxide fuel cells and effective approaches to the improvement of their functional characteristics.
The bibliography includes 202 references.

Contents

1. Introduction 644
2. Solid oxide fuel cell: electrode materials and electrochemical processes 645
 2.1. Solid oxide fuel cell 645
 2.2. Electrochemical reduction of oxygen in a solid oxide fuel cell 646
 2.3. Electrochemical oxidation of hydrogen in a solid oxide fuel cell 647
 2.4. Selection of an electrode material: a single-phase material or a composite? 648
3. Crystal structures of oxides with perovskite-like structures 649
4. Thermodynamic stability of perovskites containing 3d-metal cations 651
5. Electronic structure of oxides with the perovskite structure 653
6. Electrode materials for symmetrical solid oxide fuel cells based on oxides with the perovskite structure and of other structure types 655
 6.1. Materials based on iron-containing perovskites $A(Fe,B)O_{3-\delta}$ 655
 6.2. Electrode materials based on double perovskites $A_2(B,Mo)_2O_{6-\delta}$, where A = Sr; B = Fe, Co 661
  6.2.1. Single-phase oxide electrode materials 661
  6.2.2. Composite SFM-based electrode materials 664
 6.3. Electrode materials based on chromium- and manganese-containing perovskites 665
 6.4. Materials based on oxides with the K_2NiF_4 structure 668
 6.5. Oxides with non-perovskite structures 670
7. Conclusion 671
8. List of acronyms and designations 672

1. Introduction

Solid oxide fuel cells (SOFCs) are one of the most promising types of electrochemical power generators for stationary power plants of various capacities (from a few kilowatts to megawatts). Due to the possibility of using different hydrocarbon fuels and high rates of electrode processes at high

S.Ya.Istomin. PhD in Chemistry, Associate Professor at the Department of Chemistry, MSU.
E-mail: isserge71@gmail.com
Current research interests: crystal chemistry, solid state chemistry, new materials for electrochemical energy sources.
N.V.Lyskov. PhD in Chemistry, Leading Researcher, Head of the Laboratory of Materials Engineering for Solid State Devices, Acting Head of the Department of Functional Materials for Chemical Energy Sources, the IPCP RAS.
E-mail: lyskov@icp.ac.ru
Current research interests: study of electron-transport properties of systems with electron, ion and mixed electron-ion charge transfer; prototype development and testing of high-temperature electrochemical devices with planar and tubular geometries.
G.N.Mazo. PhD in Chemistry, Associate Professor at the Department of Chemistry, MSU.
E-mail: mazo@inorg.chem.msu.ru
Current research interests: new inorganic materials, new energy sources.
E.V.Antipov. Corresponding Member of the RAS, Doctor of Chemical Sciences, Professor, Head of the Division of Electrochemistry, Head of the Laboratory of Inorganic Crystal Chemistry at the Department of Chemistry, MSU.
E-mail: antipov@icr.chem.msu.ru
Current research interests: crystal chemistry, solid state chemistry, chemistry of new inorganic functional materials, materials for electrochemical energy sources.

Translation: T.N.Safonova

Received 13 July 2020

© 2021 Uspekhi Khimii, ZIOC RAS, Russian Academy of Sciences and IOP Publishing Limited

temperatures, electrode materials devoid of expensive noble metals can be employed in SOFCs.[1,2]

The bottleneck to the wide commercialization of SOFCs is their high operating temperature (up to 1000 °C). Chemical reactions of SOFC components at high temperature, resulting in changes in the microstructure of interfaces between the functional layers, reduce the service life of such devices. Besides, high manufacturing and maintenance costs of SOFCs decrease their economic attractiveness. Therefore, the main goals in the Solid Oxide Fuel Cell Program initiated by the United State Department of Energy[3] are as follows:

— achieve the SOFC operating lifetime of five or more years (> 40 000 h) with the lifetime performance degradation of less than 0.2% per 1000 hours,

— meet the SOFC manufacturing cost target of < $225 per kilowatt of generated power.

However, as it was mentioned in the report to the United State Congress on the status of the Solid Oxide Fuel Cell Program in 2019, there are areas that need continued work.[4] The longest tests† of SOFCs were performed at the Jülich Research Centre (Forschungszentrum Jülich), which showed the operation of SOFCs for more than 100 000 h with an average voltage degradation rate of 0.5% per 1000 hours.[5]

One approach to address some of these challenges is the transition from the manufacturing technique for the production of SOFCs, using $Zr_{0.84}Y_{0.16}O_{1.92}$ (YSZ) an electrolyte, Ni–YSZ cermet (see below) as an anode and $La_{1-x}Sr_xMnO_{3-\delta}$ (LSM) as a cathode, to the technique for the fabrication of symmetrical SOFCs (S-SOFCs). Such SOFCs are based on solid electrolytes and chemically the same material as the anode and cathode simultaneously.[6,7] In particular, the use of cathode and anode materials of the same chemical composition and microstructure reduces the energy required for manufacturing the fuel cell due to a decrease in the number of steps of thermal processing. Besides, when using hydrocarbon fuels, S-SOFCs mitigate the problem of sulfur poisoning and coking of the anode[8,9] by fuel oxidation under conditions of a short-term exposure of the anode to cathode gases.[7]

The requirements for S-SOFC electrode materials are rather stringent. These materials should meet a number of conditions imposed on cathode and anode materials. The main conditions are as follows:

— phase stability under an atmosphere of cathode and anode gases;

— the absence of a chemical reaction with the electrolyte during the electrode layer formation and under operating conditions of the fuel cell;

— electrochemical activity of the material towards oxygen reduction and fuel oxidation;

— significant electronic conductivity under oxidizing and reducing atmospheres; the value of 1 S cm^{-1} is considered to be reasonable; however, the conductivity as low as 0.01 S cm^{-1} may be acceptable if the electrode layer is thin enough;

— differences between the thermal expansion coefficients (TECs) of the electrode material and the electrolyte should be negligible and the TEC of the material should depend only slightly on the partial pressure of oxygen.

† The tests were carried out from August 2007 to January 2019.

Besides, materials for intermediate-temperature S-SOFCs (operating in the temperature range of 550–750 °C) should have a significant oxygen-ion conductivity. Mixed oxygen-ion and electronic conducting oxide-based electrode materials (mixed conductors) are highly effective due to changes in the reaction mechanisms of oxygen reduction and fuel oxidation. In the case of such oxides, electrode processes occur not only at the gas phase/electrode material/electrolyte triple phase boundary (TBP) but also involving the surface of the electrode material (gas/electrode double phase boundary).[5]

Only two reviews on electrode materials for S-SOFCs were published in the past decade, the latest review dating back to 2015.[6,7] Our goal is to close this gap since a large number of publications on this issue appeared in the past five years. In this review, we consider not only materials with perovskite-like structures, which were addressed by the majority of case studies, but also oxides that crystallize in other structure types. Taking into account that electrode materials for S-SOFCs can contain a limited range of d-metal cations, the electronic structure and thermodynamic stability of d-metal oxides are considered in relation to perovskites, and their changes depending on the chemical composition of these materials are discussed.

2. Solid oxide fuel cell: electrode materials and electrochemical processes

2.1. Solid oxide fuel cell

A solid oxide fuel cell is a solid-state electrochemical device capable of converting the chemical energy of the reaction directly to the electrical energy without intermediate steps (accompanied by large heat loss) of fuel combustion.[1,10–13] The operating principle of a fuel cell is based on the operation of an electrochemical cell with separated gas chambers, where the energy of the reaction between the fuel and the oxidant, continuously and separately supplied to the electrodes, is directly converted to the electrical energy through two major electrode reactions — the fuel oxidation at the anode and the oxidant reduction at the cathode (Fig. 1). Hydrogen is the most common fuel in SOFCs because it has high electrochemical reactivity and can be generated from different hydrocarbon fuels.

The operating temperature range of SOFCs is > 600 °C (usually, this range is 800–1000 °C), which allows the use of not only hydrogen but also hydrocarbons as the fuel, the latter being converted by high-temperature reforming to gas mixtures composed of H_2 and CO. Oxygen is the most

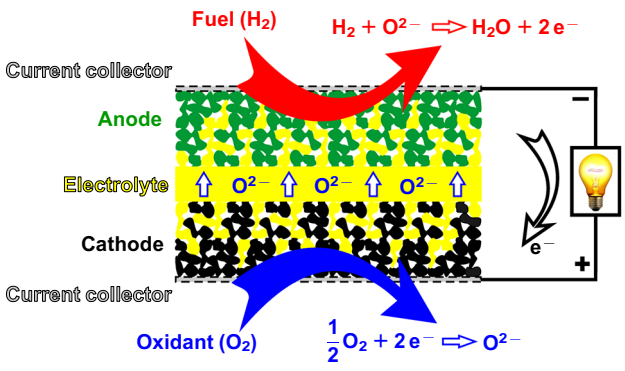


Figure 1. Schematic of the operating principle of SOFCs.

common and readily available oxidant for SOFCs. Oxygen ions, which are generated at the cathode through electrochemical reduction of oxygen, are incorporated into oxygen vacancies of the solid oxygen-conducting electrolyte and migrate under an oxygen chemical potential gradient through the solid electrolyte membrane to the anode of the fuel cell, where they are involved in the electrochemical reduction of the fuel (hydrogen). The electrons thus released go through an external circuit to electric power consumers. Therefore, the electrochemical reactions in SOFCs afford water as the final product

$$H_2\,(\text{gas, anode}) + \frac{1}{2}O_2\,(\text{gas, cathode}) \longrightarrow H_2O\,(\text{gas, anode}) \quad (1)$$

It is worth noting that the difference between the thermodynamic (equilibrium) potentials of electrode reactions determines the voltage (open circuit voltage) of the fuel cell.[2,7]

The maximum power density (P_{max}) evaluated from the voltage – current relations for the fuel cell at a specified temperature is a key parameter characterizing the performance of SOFCs. For a single SOFC, $P_{max} \geqslant 500$ mW cm^{-2} is considered to be reasonably high. To increase the power density, it is necessary to reduce the polarization losses during electric current flow through the fuel cell. The main contribution to polarization losses in SOFCs at low currents is made by activation polarization because of slow chemical electrode reactions. At lower operating temperatures of intermediate-temperature SOFCs, the oxygen reduction at the cathode makes the major contribution to activation polarization losses.[10] The polarization resistance of the electrode material/electrolyte interface (R_η) is a key parameter for evaluating of the efficiency of the electrode process.

The polarization resistance R_η is determined by electrochemical impedance spectroscopy using symmetrical electrochemical cells in electrode/electrolyte/electrode configuration. Generally, the measurements are performed at a minimum polarization voltage at the electrode/electrolyte interface, which is limited by the amplitude of the applied alternating-current overpotential of $\leqslant 10$ mV. The cathodic or anodic polarization resistance can be determined ($R_\eta \approx 0.15-0.20$ Ω cm^2 is considered to be reasonable) depending on the composition of the gas medium, in which the electrochemical cell is placed.[14] The R_η value strongly depends on the nature of the electrode material. For a single-phase electrode material, R_η can be decreased by the optimization of the microstructure of the electrode/electrolyte interface and also using a material with mixed electronic and oxygen-ion conductivity.

Taking into account the aforesaid, the literature data on electrode materials for SOFCs are analyzed using the R_η and P_{max} values as the key parameters for the comparison of the characteristics of different materials. It should be noted that P_{max} largely depends on the SOFC design and primarily on the thickness of the electrolyte as the least conducting element of the fuel cell.

2.2. Electrochemical reduction of oxygen in a solid oxide fuel cell

The charge transfer providing the transformation of both neutral species into ions and of ions into neutral species is one the main rate-limiting steps in electrode reactions, *i.e.*, both electrochemical reactions at SOFC electrodes are associated with electron transfer.[1,2,12]

The oxygen reduction at the cathode/solid electrolyte interface, resulting in the transformation of molecular oxygen into oxygen ions, is a complex multistep electrochemical process involving the simultaneous charge (electron) transfer and mass transfer associated with the migration of oxygen ions from the cathode into the bulk of the solid electrolyte. Depending on the nature of the cathode material (an electronic or mixed ionic – electronic conductor) and the cathode/electrolyte interface configuration (a single-phase or composite cathode) and microstructure, the oxygen reduction can occur through different mechanisms.[15–18] However, despite the diversity of the proposed reaction schemes, it is practically impossible to distinguish a particular scheme as the major one because of the influence of numerous internal (the nature of the cathode material) and external (the microstructure of the cathode) factors. Besides, it is rather difficult to distinguish a single rate-limiting step among several sequential electrode reactions. Nevertheless, the overall cathodic process can be described in terms of a general phenomenological scheme (Fig. 2) involving a sequence of possible steps of the oxygen reduction. As an example, let us consider the following sequence for a cathode material with very low oxygen ion conductivity:

1) adsorption of oxygen molecules from the gas phase on the electrode surface

$$\frac{1}{2}O_2\,(\text{gas}) \longrightarrow \frac{1}{2}O_{2,\,ads}\,(\text{cathode}) \quad (2)$$

2) dissociation of adsorbed oxygen molecules to atomic oxygen

$$\frac{1}{2}O_{2,\,ads}\,(\text{cathode}) \longrightarrow O_{ads}\,(\text{cathode}) \quad (3)$$

3) surface diffusion of adsorbed oxygen atoms to the gas/cathode/electrolyte triple phase boundary

$$O_{ads}\,(\text{cathode}) \longrightarrow O_{ads}\,(\text{TPB}) \quad (4)$$

4) charge transfer to oxygen atoms adsorbed on TPB to form oxygen ions followed by their incorporation into oxygen vacancies ($V_O^{\cdot\cdot}$) in the crystal lattice of the solid electrolyte (hereinafter, the Kröger – Vink notation is used):

$$O_{ads}(\text{TPB}) + 2\,e'(\text{cathode}) + V_O^{\cdot\cdot}(\text{electrolyte}) \longrightarrow O_O^x(\text{electrolyte}) \quad (5)$$

[O_O^x(electrolyte) is an oxygen ion in a regular site of the electrolyte].

When is used a single-phase mixed ionic – electronic conductor is used the cathode, the electrochemical reaction can involve the whole electrode surface, with the possible charge transfer to not only TPB but also the gas/electrode double phase boundary

$$O_{ads}\,(\text{cathode}) + 2\,e'\,(\text{cathode}) + V_O^{\cdot\cdot}\,(\text{cathode}) \longrightarrow O_O^x\,(\text{cathode}) \quad (6)$$

followed by bulk diffusion of oxygen ions through oxygen vacancies in the anion sublattice of the cathode material to the cathode/electrolyte interface and their transfer across this interface and the subsequent incorporation into vacant anion sites in the electrolyte structure

$$O_O^x\,(\text{cathode}) + V_O^{\cdot\cdot}\,(\text{electrolyte}) \longrightarrow V_O^{\cdot\cdot}\,(\text{cathode}) + O_O^x\,(\text{electrolyte}) \quad (7)$$

In this case, the oxygen reduction occurs also on the surface of the particles of the cathode material with oxygen-ion conductivity. This leads to a decrease in the polarization

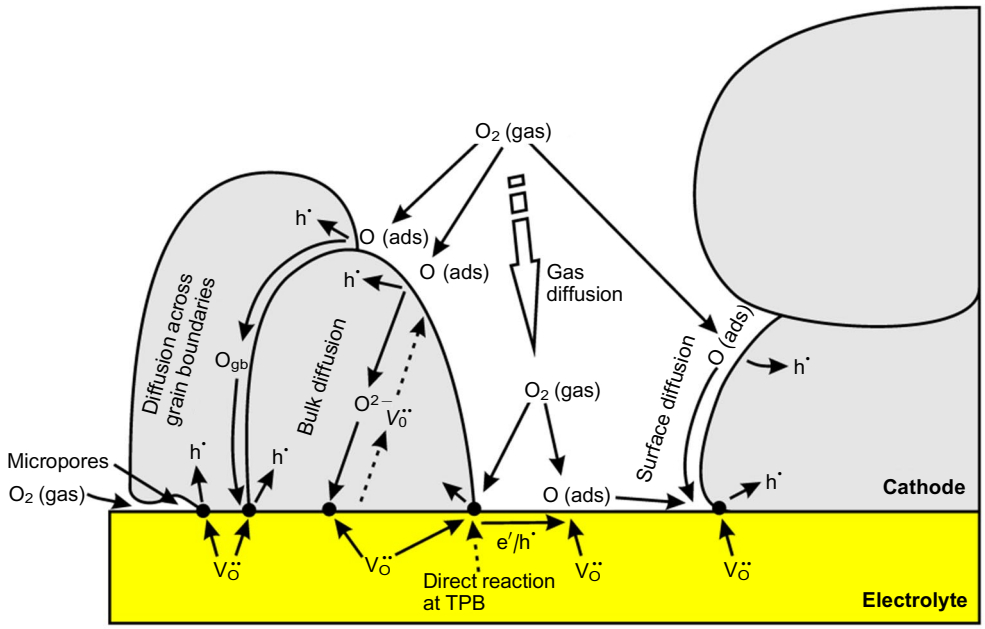


Figure 2. Schematic of possible elementary reaction steps during oxygen reduction at the electrode/electrolyte interface. O (ads) are adsorbed oxygen species, such as $O_{2,ads}$, O_{ads}, O^{-}_{ads} or O^{2-}_{ads}; O_{gb} is atomic oxygen that diffuses across the grain boundary; e' is an electron carrier; $h^{\bullet}$ is a hole charge carrier.[1] Published with the permission of The Elsevier.

resistance of the cathode/electrolyte interface and an increase in the performance of SOFCs based on such materials, particularly, of intermediate-temperature SOFCs.[10]

2.3. Electrochemical oxidation of hydrogen in a solid oxide fuel cell

The electrochemical oxidation of hydrogen is the main reaction at the SOFC anode. The Ni–YSZ cermet, a ceramic–metal composite, containing nickel metal and YSZ solid electrolyte particles is commonly used as an anode material. The presence of YSZ not only prevents thermally induced Ni particle coarsening but is also responsible for the appearance of mixed ionic–electronic conducting properties. Materials for anodes based on oxides with the perovskite structure are being extensively investigated as an alternative to conventional cermets.[19, 20]

The mechanism of anodic oxidation of hydrogen in a system containing Ni metal in contact with YSZ (Fig. 3 *a*) has been studied in most detail. Several mechanisms of this reaction were proposed; however, its kinetics is poorly understood.[1, 11, 12] The kinetics of hydrogen oxidation using the Ni–YSZ cermet is influenced by numerous factors, among which the composition of the fuel gas and the microstructure of the electrode are most important. It was found that the presence of H_2O and CO in the fuel gas mixture and the microstructure of the cermet have a dominant effect on the polarization behaviour of the anode. Besides, the kinetics of the anodic reaction and the performance of the anode may depend on other factors, for example, on the thickness of the electrode layer, which is responsible for gas accessibility of reactants to reaction sites.

Nickel metal plays a key catalytic role in the fuel oxidation. Meanwhile, the presence of YSZ also affects the electrocatalytic oxidation of hydrogen. In the fuel gas flow under reducing conditions, the electronic conductivity of the electrolyte increases, thereby facilitating the increase in the rate of the electrochemical reaction.[21] The electronic conductivity of YSZ leads to an increase in the size of the reaction zone around TPB, resulting in an increase in the concentration of accessible active reaction sites (Fig. 3 *b*). The surface modification of the YSZ electrolyte by introducing an electronic conducting additive or by partial or complete replacement of YSZ in the anode by a mixed ionic–electronic conductor improves the performance characteristics of the anode.[21–23]

The general idea of the anodic electrochemical reaction using the Ni–YSZ cermet is similar to that considered for SOFC cathodes; however, there are some significant differences. One possible mechanism of hydrogen oxidation can include the following elementary steps:[1]

— adsorption of molecular hydrogen on the surface of YSZ or nickel:

$$H_2\,(\text{gas}) \longrightarrow H_{2,\,ads}\,(\text{YSZ or Ni}) \qquad (8)$$

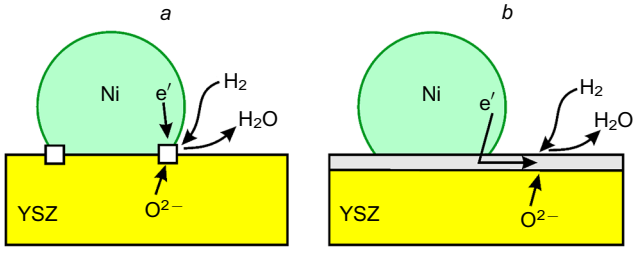


Figure 3. Schematics of the electrochemical oxidation of hydrogen at TPB of the SOFC anode (*a*) and expansion of the reaction zone during electrochemical oxidation of hydrogen in the vicinity of TPB due to electronic conductivity of the solid electrolyte (*b*).[12] Published with the permission of The Elsevier.

— surface diffusion of adsorbed molecular hydrogen to TPB

$$H_{2,\,ads}\,(YSZ\text{ or }Ni) \longrightarrow H_{2,\,ads}\,(TPB) \quad (9)$$

— anodic electrochemical reaction

$$O_O^x\,(YSZ) + H_{2,\,ads}\,(TPB) \longrightarrow \quad (10)$$
$$\longrightarrow H_2O\,(gas) + 2e'\,(anode) + V_O^{\cdot\cdot}\,(YSZ)$$

It is worth noting that the hydrogen oxidation is significantly affected by the presence of water vapour in the fuel giving rise to adsorbed oxygen atoms on the surface of nickel metal particles. Hence, the rate of hydrogen oxidation is related to the activity of oxygen on the metal surface.[24] In this case, the mechanism of oxidation will include the following key steps:

— dissociative decomposition of water

$$H_2O\,(gas) \longrightarrow H_2\,(gas) + O_{ads}\,(Ni) \quad (11)$$

— dissociative adsorption of hydrogen

$$H_2\,(gas) \longrightarrow 2\,H_{ads}\,(YSZ) \text{ — on the YSZ surface} \quad (12)$$

$$H_2\,(gas) \longrightarrow 2\,H_{ads}\,(Ni-O_{ads}) \text{ — on the Ni surface coated with } O_{ads} \quad (13)$$

— charge transfer

$$O_O^x \longrightarrow O_{ads}^{2-}\,(YSZ) + V_O^{\cdot\cdot} \quad (14)$$

$$O_{ads}^{2-}\,(YSZ) + O_{ads}\,(Ni) \longrightarrow O_{ads}\,(YSZ) + O_{ads}^{2-}(Ni) \quad (15)$$

$$O_{ads}^{2-}\,(Ni) \longrightarrow O_{ads}\,(Ni) + 2e' \quad (16)$$

$$2\,H_{ads}\,(YSZ) + O_{ads}\,(YSZ) \longrightarrow H_2O\,(gas) \quad (17)$$

$$2\,H_{ads}\,(Ni-O_{ads}) + O_{ads}\,(Ni) \longrightarrow H_2O\,(gas) \quad (18)$$

Therefore, the efficient anode material should have the mixed oxygen-ion and electronic conductivity. This may be a composite consisting of several phases, one of which is characterized by high electronic conductivity, whereas another phase should have high oxygen-ion conductivity. An alternative approach is the use of a single-phase material — a mixed ionic–electronic conductor. An example of such material is double perovskite $Sr_2Fe_{1.5}Mo_{0.5}O_{6-\delta}$ (see below, Section 6.2).

2.4. Selection of an electrode material: a single-phase material or a composite?

Perovskite like oxides of the general composition ABO_3 containing d-metal cations are the most common single-phase materials for S-SOFCs. On the one hand, they are widely employed because the majority of d-metal cations usually adopt an octahedral coordination environment formed by oxygen ions. On the other hand, infinite three-dimensional frameworks of octahedra connected by sharing all six vertices are energetically more favourable than the frameworks of edge- or face-sharing octahedra, which are observed in other structure types, and they diminish electrostatic repulsions between cations in octahedra. Besides, perovskites are called chemical chameleons because their cationic composition can involve different elements, and practically important properties of these compounds can be varied by iso- and heterovalent cation substitution. Perovskite-like oxides can have a high oxygen-ion conductivity and, consequently, can serve as highly efficient single-phase electrode materials for intermediate-temperature S-SOFCs.

Thermodynamic stability and simultaneously high electrical conductivity in oxidizing and reducing atmosphere are critical requirements for choosing a d-metal cation incorporated in the electrode material for S-SOFCs. Perovskites with 3d-metal cations (titanium, vanadium, chromium, manganese and molybdenum) best meet these requirements. However, perovskites containing one of these cations in the B-site have a very low oxygen-ion conductivity and, consequently, they often show low activity towards oxygen reduction, particularly in an intermediate-temperature mode. Besides, many single-phase oxide materials exhibit much weaker electrochemical activity towards fuel oxidation than the conventional Ni – YSZ cermet.[6, 8, 25] In particular, this is the reason why such oxides are often used as components of composite materials containing, apart from the perovskite phase, an electrolyte material.

Perovskites with late 3d-metal cations (Co, Ni, Cu), having high electrochemical activity towards cathodic oxygen reduction due to oxygen-ion conductivity, are thermodynamically unstable at high temperature in reducing atmosphere of the anode gas. Iron-containing perovskites can be considered separately. On the one hand, they easily form oxygen vacancies in the crystal structure; on the other hand, they are often stable under reducing atmosphere at 500 – 900 °C. Due to these properties, such perovskites have attracted attention as electrode materials for S-SOFCs.

As mentioned above, the electrode/electrolyte interface structure may have a significant impact on the efficiency of electrode processes. The nature of the single-phase material is an obstacle for meeting all requirements for S-SOFC electrode materials. This issue can be addressed using composite electrodes. This approach is commonly used to create conventional SOFC anodes and cathodes. The combined application of two or more phases in a single electrode can give rise to new useful properties or lead to the improvement of properties, thereby making it possible to overcome the limitations associated with the nature of the single-phase material. In recent years, composite electrodes were widely used for the fabrication of S-SOFCs.

The simplest approach to prepare composite electrodes is based on the homogenization of two or more phases with different useful physicochemical properties. This is particularly the case with a combination of electronic and oxygen-ion conductivity, thereby allowing the fabrication of oxygen-ion and electronic conducting electrodes. In these electrodes, electrochemical reactions occur with the involvement of not only TPB but also the total accessible surface of the electrode material. This leads to an increase in the electrode activity towards oxygen reduction (in the case of the cathode) or fuel reduction (in the case of the anode). Consequently, an evident improvement of electrode characteristics can be achieved by using composite materials, particularly, in intermediate-temperature fuel cells.[26, 27]

The microstructure of electrodes is a key parameter responsible for the efficiency of electrochemical processes and high power density of SOFCs. It is a challenge to prepare a composite electrode with an ideal microstructure, which will allow the percolation threshold to be overcome in both the electronic and ionic conducting phases, using the conventional homogenization of components because this technique requires the high-temperature thermal treatment. This process may lead to a change in the microstructure of the composite electrode due to solid-state diffusion processes and different nature of phase sintering.

In recent years, the infiltration (impregnation) of the porous support, which is created using solid electrolyte or electrode materials, with electroactive material particles has

gained wide use for the elimination of detrimental effects caused by high-temperature sintering.[28 – 36] This approach is promising for the fabrication of composite electrodes with a unique microstructure. The main advantage of this approach is that nanoparticles of the electrocatalyst can be formed at temperatures much lower than the sintering temperature of the porous support. This ensures the preservation of the nanostructured state of electroactive additive particles, thereby facilitating a high rate of electrode electrochemical reactions. The key steps in the infiltration are as follows:

— the formation of the densely sintered solid electrolyte membrane of the porous layer on the surface; the sintering of this layer occurring at high temperatures (1100 – 1200 °C) promotes the formation of a strong contact with the surface of the supporting solid electrolyte, which ensures the efficient charge transport and microstructural stability of the electrode under long-term operation;

— the filling of the porous layer with a precursor of the electroactive phase followed by the thermal treatment; a solution containing stoichiometric amounts of required metal salts, a surfactant and special additives can serve as the precursor; the thermal treatment is performed at 450 – 500 °C (which is significantly lower than the sintering temperature of the porous layer), giving a composite structure composed of electroactive nanoparticles within the porous layer.

The application of the infiltration technique has the following advantages over the conventional methods of the formation of the electrode layer, which promotes the enhancement of electrochemical activity towards both the oxygen reduction and fuel oxidation:[28, 33, 36]

— the porous structure of the electrode provides a more extensive interface with the electrolyte compared to the corresponding conventional electrode;

— a mismatch in the thermal expansion coefficients of the electrode and electrolyte materials is diminished;

— stability of mechanical properties is provided by the created porous support;

— small volumes of the electrocatalyst are required for the percolation threshold of the electronic conductor to be formed;

— due to a low temperature of the thermal treatment, more active materials unstable at high temperatures can be employed as catalysts, with the chemical side reactions with the electrolyte, resulting in the decrease in the catalyst performance, being less probable;

— electrode material grains can retain the nanometre size, thereby providing a large active surface area and the extended TPB.

The efficiency of this approach was demonstrated in a number of studies, where it was applied to decrease the polarization resistance of the electrode by an order of magnitude.[28 – 32]

In subsequent parts of the review, the crystal structures of perovskite-like oxides acting as electrocatalysts in S-SOFCs are briefly described. Then the data on the thermodynamic stability of perovskites are analyzed in order to answer the question of which cationic composition will allow the use of these compounds as electrode materials for S-SOFCs. The electronic structures of perovskites and their changes depending on the cationic composition are considered in order to explain why oxides containing late 3d-metal (Fe, Co, Ni and Cu) cations easily form oxygen vacancies in the structure. The final Section addresses the recent data on single-phase and composite electrode materials for S-SOFCs based on perovskite-like oxides and oxides crystallizing in other structure types.

3. Crystal structures of oxides with perovskite-like structures

There are plenty of data on the crystal structures of perovskites.[37 – 39] The crystal structure of cubic perovskite ABO_3 is shown in Fig. 4 *a*. The centres of the ideal octahedra are occupied by small B cations, in particular by d-metal cations. The B – O – B angle between the vertex-sharing BO_6 octahedra is 180°. Large alkali, alkaline-earth and rare-earth metal cations generally serve as A cations that are located at the centre of the unit cell and have the coordination number (CN) of 12 (cuboctahedron).

The cubic perovskite structure is stable only at a certain ionic radius ratio of the A and B cations and oxygens (r_A, r_B and r_O, respectively). This ratio was derived by Goldschmidt[40] from geometric considerations and was called the t factor or the tolerance factor.

$$t = \frac{r_A + r_O}{\sqrt{2}(r_B + r_O)} \qquad (19)$$

For the cubic structure, $t \approx 1$; however, perovskites with $t < 1$ are most widespread. In these compounds, the size of the A cation is smaller than that required for CN 12, which leads to cooperative rotation of BO_6 octahedra, resulting in a decrease in the CN of the A cation. There are several types of distortions of the perovskite structure at $t < 1$.[41 – 44] The most important types are rhombohedral (Fig. 4 *b*) and orthorhombic (Fig. 4 *c*) distortions. The latter type is most often observed in oxides.[45, 46]

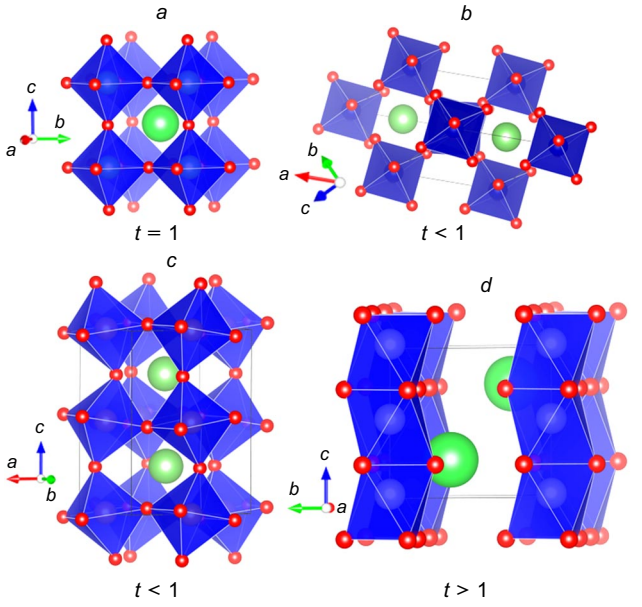


Figure 4. Crystal structures of cubic (*a*), rhombohedrally distorted (*b*) and orthorhombically distorted (*c*) perovskites and the hexagonal analogue of perovskite (2H structure) (*d*). Green spheres represent A cations, small red spheres are oxygen ions, B cations are in BO_6 octahedra (blue). The Figure was prepared by the authors using the data of Ref. 38.

In rhombohedrally distorted perovskites [$LaCoO_3$,[47] $LaNiO_3$ (Ref. 48)], the cooperative rotation of BO_6 octahedra leads to a decrease in the coordination number of the A cations to 9; in the orthorhombically distorted perovskite, to 8. The unit cell parameters of rhombohedrally distorted perovskite (a_h and c_h in the hexagonal setting) are related to the unit cell parameter of cubic perovskite (a_c) as $a_h \approx \sqrt{2}\,a_c$, $c_h \approx \sqrt{3}\,a_c$; for orthorhombically distorted perovskite (a_o, b_o, c_o), as $a_o \approx \sqrt{2}\,a_c$, $b_o \approx \sqrt{2}\,a_c$, $c_o \approx 2\,a_c$. Oxides $LaBO_3$ containing large 3d-metal B cations, such as $LaScO_3$,[49] $LaTiO_3$,[50] $LaVO_3$,[51] $LaCrO_3$,[52] $LaMnO_3$ (Ref. 53) and $LaFeO_3$,[54] have the orthorhombically distorted perovskite structure. The cooperative rotation of BO_6 octahedra leads to a decrease in the angle between the vertex-sharing octahedra and its significant deviation from 180° in the structure of cubic perovskite. Thus, a decrease in the angle between the vertex-sharing BO_6 octahedra is observed in the crystal structures of manganese-containing perovskites $AMnO_3$, from 155.23(3)° for $LaMnO_3$ ($t = 0.91$) to 144.2(1)° for $YMnO_3$ ($t = 0.86$).[55] This leads to the narrowing of the energy band, which affects the electrical conductivity of perovskites (see Section 5).

Hexagonal analogues of the perovskite structure are formed if the tolerance factor is much larger than unity. The structure of cubic perovskite can be described as a three-layer close packing of AO_3 layers. Meanwhile, a two-layer stacking of AO_3 layers is also possible, resulting in the hexagonal symmetry of the oxide crystal lattice (2H structure).[38,39] In this case, the BO_6 octahedra are connected by sharing faces, as opposed to vertex-sharing octahedra in the cubic perovskite structure (Fig. 4*d*). There are a number of intermediate structures between the two- and three-layer close packed arrays of AO_3 layers, in which mixed cubic and hexagonal AO_3 stacking occurs with different ratios of these packing modes. Such oxides contain groups linked both by sharing vertices (if B cations occupy octahedral voids in the three-layer close packing) or faces (if B cations occupy octahedral voids in the two-layer close packing) of BO_6 octahedra. These oxides are called hexagonal analogues of perovskite (not to be confused, as is often the case in the literature, with rhombohedrally distorted perovskites with the unit cell parameters in the hexagonal setting!). Hexagonal analogues of the perovskite structure are formed, as mentioned above, if $t > 1$, which means that these oxides contain large A cations (*e.g.*, Ba^{2+} or Sr^{2}) and highly charged B cations, consequently, with a small ionic radius. Examples of such oxides are $BaMnO_3$ ($t = 1.10$), $BaCoO_3$ ($t = 1.10$) and $BaNiO_3$ ($t = 1.13$) with the 2H structure (see Fig. 4*d*).[56–58] It is worth noting that hexagonal analogues of perovskite with a different number of close-packed $AO_{3-\delta}$ layers in the unit cell can be prepared by varying the synthesis conditions related to changes in the oxygen stoichiometry (δ) of oxide $ABO_{3-\delta}$. For example, this is true for the $BaMnO_{3-\delta}$ system.[59,60]

If an oxide with the perovskite structure contains several A and(or) B cations with significantly different ionic radii or charges, these cations can be ordered in the crystal structure. The structures, in which cations are ordered only in one A- or B-site, are referred to as double perovskites.[38] It should be noted that perovskites containing several B cations are often erroneously called double perovskites, despite the absence of experimental data on the ordering of cations in their structures. The simultaneous cation ordering in both the A- and B-sites occurs in quadruple perovskites. Examples of such phases are the oxides $NaLnMnWO_6$ (Ln = La, Ce, Pr, Nd, Sm, Gd, Dy, Ho) and $NaLnMgWO_6$ (Ln = Ce, Pr, Nd, Sm, Eu, Gd, Tb, Dy, Ho).[61]

The main factors affecting the ordering of B cations in double perovskites are significant differences in the ionic radii and charges and the predominant coordination environment of two different B cations involved in double perovskites $A_2B'BO_6$.[62] The charge difference between two B cations is assumed to be the key factor. Thus, the probability of ordering is high if this difference is $\geqslant 3$. There are different modes of ordering of B cations in double perovskites,[38,61,62] the ordering of B cations in a chess-like fashion being most commonly observed (Fig. 5). The crystal lattice symmetry of such double perovskites, like that of the perovskite structure, depends on the ionic radius ratio of the A and B cations.[38,63] It is worth noting that the degree of the ordering of cations in the B-site and, consequently, certain important physicochemical properties of double perovskites are often determined by the conditions of their synthesis. An example is double perovskite Sr_2FeMoO_6.[64] Partial ordering of B cations can also be observed in the case of the B : B′ ratio of two types of B cations different from 1 : 1. Thus, a double perovskite phase is observed for $Sr_2Fe_{2-x}Mo_xO_6$ in a wide range of compositions ($0.5 \leqslant x \leqslant 1.2$).[65]

The distinguishing feature of oxides with the perovskite structure is that they can contain oxygen vacancies. The formation of oxygen vacancies in perovskites containing d-metal cations depends on the stability of CN < 6 for this B cation. Many perovskites have large oxygen nonstoichiometry. For example, the oxygen nonstoichiometry of iron-containing perovskites $SrFeO_{3-\delta}$ extends from $SrFeO_3$ (Ref. 66) to $SrFeO_2$.[67] There are several $SrFeO_{3-\delta}$ phases, containing different coordination polyhedra of iron cations and characterized by different ordering patterns in the crystal structure, between these end members.[66]

Depending on the concentration of oxygen vacancies and the nature of A and B cations, the latter can be ordered to form various structures.[38,68] The layered ordering is one of the most commonly occurring type of oxygen vacancy ordering in the structures of oxygen-deficient perovskites of general composition $ABO_{2.5}$ ($A_2B_2O_5$). These perovskites contain layers of vertex-sharing BO_6 octahedra alternating with oxygen-deficient layers composed of chains of BO_4 tetrahedra [the structure type of brownmillerite

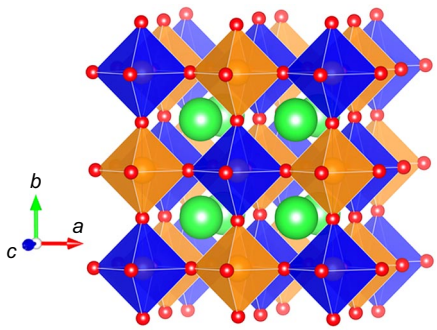


Figure 5. Crystal structure of cubic double perovskite $A_2B'BO_6$ with ordered B cations (blue octahedra) and B′ cations (brown octahedra). The octahedra are arranged in a chess-like fashion. Green spheres represent A cations, small red spheres are oxygen ions. The Figure was prepared by the authors using the data of Ref. 62.

$Ca_2(Fe,Al)_2O_5$, Fig. 6 *a*]. Oxides with the brownmillerite structure are known for manganites A_2MnGaO_5 (Refs 69 and 70) and ferrites $A_2Fe_2O_5$,[71,72] where A = Ca, Sr.

A layered ordering is possible in oxygen-deficient perovskites containing two A cations with different sizes, for example, Y^{3+} (r = 1.019 Å, CN 8)[73] and Ba^{2+} (r = 1.61 Å, CN 12),[73] resulting in the formation of double perovskite RAB_2O_5, where R is a rare-earth metal cation, A = Sr, Ba; B = Mn, Fe, Co (Fig. 6 *b*).[74–76] In this case, the coordination environment of the B cation can be described as a tetragonal pyramid (CN 5), that of the R cation is a cube (CN 8), and that of the A cation is a cuboctahedron (CN 12). It is noteworthy that RAB_2O_5 have large oxygen nonstoichiometry ($RAB_2O_{5+\delta}$), which depends on the degree of the ordering of A and R cations in these phases. The latter is determined by the ionic radius ratio of the A and R cations and by the conditions of the synthesis and subsequent thermal treatment of the oxide. Such double perovskites exhibit an extremely high oxygen-ion conductivity.[77,78]

The formal oxidation state of d-metal cations in oxides with the perovskite structure can be changed not only through the heterovalent cation substitution in the A- and B-sites or variation of the oxygen content but also by a structural modification through the insertion of different charged units into the perovskite structure. For instance, the insertion of the LaO^+ unit with the rock salt structure into $LaMnO_3$ affords the phase La_2MnO_4, in which manganese cations have a lower oxidation state (+2). The average formal oxidation state of manganese cations can be varied by changing the quantitative ratio between the LaO^+ and perovskite units. The general formula of these perovskite-like oxides is $A_{n+1}B_nO_{3n+1}$, where n is the number of BO_2 layers in the perovskite unit (homologous series of Ruddlesden–Popper phases, Fig. 7). The crystal structures of oxides A_2BO_4 with $n = 1$ are also often assigned to the structure type K_2NiF_4. It is noteworthy that these oxides contain interstitial sites in the unit with the rock salt structure, which can be occupied by oxygen ions, and the chemical composition of the oxides corresponds to the formula $A_2BO_{4+\delta}$. The oxygen index (δ) can be rather large; for example, $\delta \approx 0.42$ in $La_{1.2}Sr_{0.8}MnO_{4+\delta}$.[79,80] The oxygen ion mobility in the unit with the rock salt structure is high, resulting in a significant oxygen-ion conductivity of phases $A_2BO_{4+\delta}$ at moderate temperatures.[81–83]

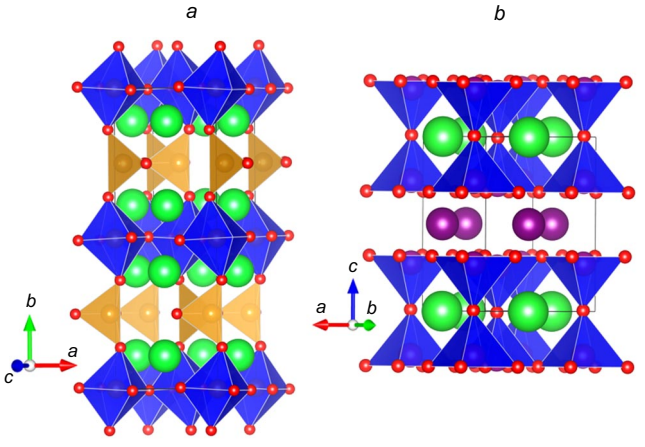


Figure 6. Crystal structures of oxygen-deficient perovskites $ABO_{2.5}$ — brownmillerite $Ca_2(Fe,Al)_2O_5$ (*a*) and double perovskite RAB_2O_5, where R is a rare-earth metal cation; A = Sr, Ba; B = Mn, Fe, Co (*b*). The B cations are in blue and brown polyhedra, A cations are in green, R cations are in purple, and oxygen ions are in red. The Figure was prepared by the authors using the data of Refs 69 and 76.

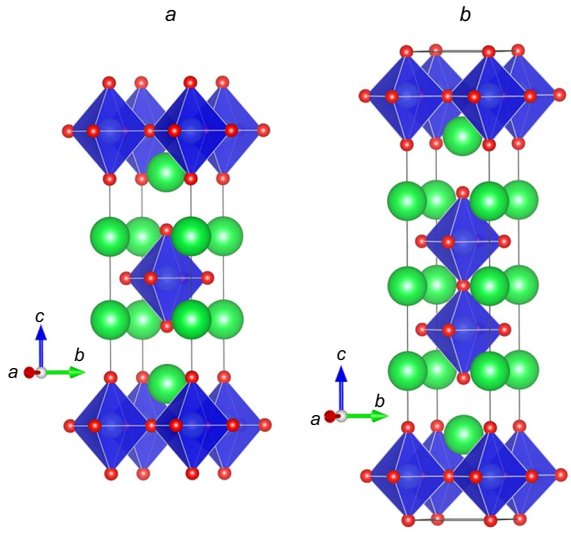


Figure 7. Crystal structures of perovskite-like oxides belonging to the homologous series of Ruddlesden–Popper phases $A_{n+1}B_nO_{3n+1}$, n = 1 (*a*) and 2 (*b*).[38] The A cations are shown as green spheres, oxygen ions are shown as red spheres, B cations are in BO_6 octahedra (blue). The Figure was prepared by the authors using the data of Ref. 38.

Therefore, perovskite-like oxides, used as electrode materials for S-SOFCs, have rich crystal chemistry. It includes phases with a cubic or distorted perovskite structure, phases containing several ordered cations with different ionic radii or charges and phases with the simultaneous ordering of cations and anion vacancies. The modification of the perovskite structure through the insertion of the RO^+ unit with the rock salt structure affords Ruddlesden–Popper phases. The unique feature of these phases is the presence of interstitial sites, which can be occupied by oxygen ions. This leads to high oxygen-ion conductivity. The BO_6 octahedra connected by sharing vertices are the main structural units of perovskite-like oxides. This mode of connection, as shown below (see Section 5), gives rise to wide energy band gaps and high electrical conductivity. To get an insight into how the stability of different perovskites depends on the nature of A and B cations, it is necessary to consider their thermodynamic properties.

4. Thermodynamic stability of perovskites containing 3d-metal cations

Thermodynamic stability of perovskites containing 3d metals as B cations can be evaluated from the enthalpies of their formation ($\Delta_f H^\circ_{298}$) because the entropy of the formation of perovskites from elements has negative values and only slightly depends on the nature of the cations in their structures. The data on the enthalpies of formation of perovskites ABO_3, where A = La, Ca, Sr; B = Sc, Cr, Mn, Fe, Co, Ni, are summarized in Table 1.

These values can be used to analyze the tendencies of changes in stability of perovskites upon variation of the cation composition in hydrogen medium provided that the reaction affords a 3d element in the metallic state and oxides

Table 1. Enthalpies of formation of perovskites ABO_3, where A = La, Ca, Sr; B = Sc, Cr, Mn, Fe, Co, Ni, from elements at 298 K.

Composition	Structure	$\Delta_f H^\circ_{298}$, kJ mol^{-1}	Ref.
$LaScO_3$	O	-1888.85 ± 2.67	84
$LaCrO_3$	O	-1536.21 ± 5.14	85
$LaMnO_3$	O	-1451.1 ± 2.5	86
$La_{0.8}Ca_{0.2}MnO_3$	O	-1401.7	87
$La_{0.2}Ca_{0.8}MnO_3$	O	-1283.6	87
$La_{0.8}Sr_{0.2}MnO_3$	R	-1421.3	87
$La_{0.2}Sr_{0.8}MnO_3$	C	-1285.6	87
$LaFeO_3$	O	-1373.48 ± 2.61	85
$LaCoO_3$	R	-1241.34 ± 2.13	85
$LaNiO_3$	R	-1192.41 ± 2.75	85

Note. The following notations of the perovskite structures are used: O, orthorhombically distorted; R, rhombohedrally distorted; C, cubic.

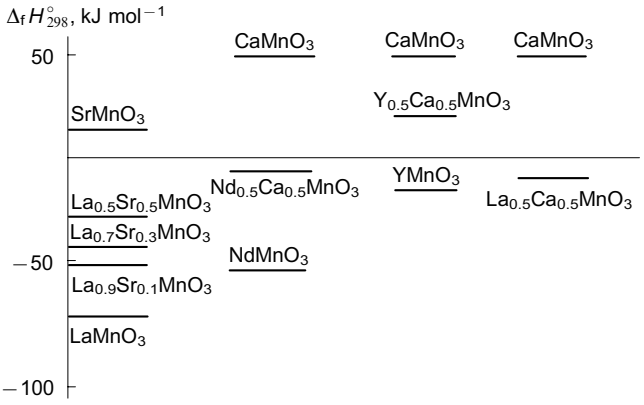


Figure 8. Enthalpies of formation of manganese-containing perovskites $R_{1-x}A_xMnO_3$. The enthalpies are given with respect to the enthalpy of formation of the stoichiometric mixture of oxides $(1-x/2)\,Mn_2O_3 + x\,MnO_2 + (1-x/2)\,R_2O_3 + xAO$, where R = La, Nd, Y and A = Ca, Sr.[86] Published with the permission of The Elsevier.

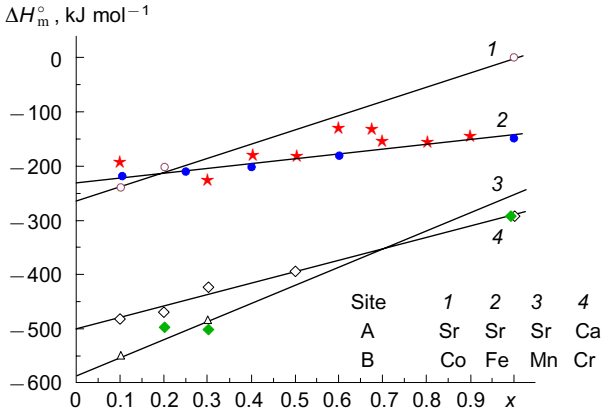


Figure 9. Enthalpy of oxidation (ΔH°_m) of perovskites $La_{1-x}A_xBO_{3-\delta}$, where A = Ca, Sr, B = Mn, Fe, Cr and Co, as a function of the composition (x). Open symbols represent the values calculated from the plots of the oxygen nonstoichiometry of oxides as a function of the partial pressure of oxygen; coloured symbols are calorimetrically determined values.[89] Published with the permission of the Royal Society of Chemistry.

La_2O_3 and AO, where A = Ca, Sr. As can be seen from the reported data, an increase in the atomic number of the 3d element leads to a decrease in the enthalpy of the formation of perovskite $LaBO_3$ (early 3d-metal perovskites are most thermodynamically stable, while late 3d-metal perovskites are least thermodynamically stable). This may be attributed to the known tendency to a decrease in stability of the formal oxidation state +3 in the series of 3d metals from scandium to nickel. Therefore, perovskites containing 3d-metal cations, such as titanium, vanadium, chromium, manganese and iron, are of most interest as electrode materials for S-SOFCs in terms of thermodynamic stability.

The literature data on the thermodynamic stability of perovskites containing different A cations lead to the following conclusions. First, thermodynamic stability correlates with the *t* factor and decreases as the latter decreases. This tendency was found for perovskites $A^{2+}B^{4+}O_3$ and $A^{3+}B^{3+}O_3$.[88] Thus, a decrease in the ionic radius of the rare-earth metal cation and, consequently, in the *t* factor, for example for $RMnO_3$ in the series $R = La^{3+}$ (1.216 Å), Nd^{3+} (1.163 Å), Y^{3+} (1.019 Å) (the radii are given for CN 9),[73] leads to a decrease in thermodynamic stability of manganese-containing perovskites (Fig. 8). This tendency is also observed for the oxides $SrMnO_3$ and $CaMnO_3$. Therefore, perovskites containing large and, consequently, basic A cations are thermodynamically most stable. Second, thermodynamic stability decreases with increasing oxidation state of the d metal. Thus, an increase in the degree of heterovalent substitution of rare-earth metal cations for alkaline-earth metal cations leads to an increase in the enthalpy of formation of $La_{1-x}A_xMnO_3$, where A = Ca, Sr (see Table 1, Fig. 8).

In the review publication,[89] the experimental and calculated thermodynamic data on the enthalpies of oxidation (Fig. 9) of oxygen-deficient perovskites were analyzed according to the equation

$$4\,ABO_{2.5} + O_2 \longrightarrow 4\,ABO_3 \qquad (20)$$

which showed that the thermodynamic propensity to form perovskites with oxygen stoichiometry changes in the following series: Cr > Mn > Fe ≈ Co. Besides, in each series of compositions, the thermodynamic probability of the formation of oxygen-deficient perovskites increases with increasing degree of heterovalent replacement of La^{3+} ions with Sr^{2+} cations. This tendency reflects the above-mentioned decrease in stability of oxides with the perovskite structure with increasing oxidation state of the d metal. It is worth noting that the thermodynamic data are indicative of a much lower stability of oxygen vacancies in oxides with structures of hexagonal analogues of perovskite compared to perovskite-like oxides.[89] This may be attributed to the fact that the strong electrostatic repulsion between B cations, which are located in face-sharing BO_6 octahedra in hexagonal analogues of perovskite, is partially compensated by oxygen anions at these faces of the octahedra. Correspondingly, the partial removal of anions leads to destabilization of the structure and a decrease in stability of the oxide.

Therefore, 3d-metal perovskites containing titanium, vanadium, chromium, manganese and iron cations show the highest thermodynamic stability in the series of perovskites RBO_3, where R is the rare-earth metal cation, and these compounds can be used as electrode materials for S-SOFCs. Iron-containing perovskites are of obvious interest because of the possible presence of oxygen vacancies.

The above-considered thermodynamic data demonstrate that, when choosing the A cation, one should take into account higher stability of oxides containing large A cations. For example, La^{3+} is a rare-earth metal cation of choice, and Sr^{2+} or Ba^{2+} are the preferable alkaline-earth metal cations taking into account the composition stability range of the perovskite phase and the reactivity towards the electrolyte material.

5. Electronic structure of oxides with the perovskite structure

The knowledge of the electronic structure of a complex d-metal oxide with the perovskite structure is required for an informed choice of the chemical composition of the oxide as an electrode material for S-SOFCs. The electronic structure is responsible for electrophysical properties of perovskite and allows the assessment of its stability and the possibility of the formation of oxygen vacancies in the crystal structure.

In oxides with the perovskite structure, d-metal cations occupy the centre of an octahedron formed by oxygen ions. The schematic diagram of σ- and π-interactions between the metal d-orbitals and oxygen 2p-orbitals in the perovskite structure is shown in Fig. 10.

A simplified model of the electronic band structure of perovskite can be constructed by assuming the formation of energy bands in the crystal from the corresponding molecular orbitals of the BO_6 octahedron as the structural unit.[90,91] The resulting electronic structure of perovskite ABO_3 is shown in Fig. 11.

A fragment corresponding to valence bands includes the completely filled bands formed mainly by oxygen 2p-orbitals (overlapped O_{nb} bands, B–O (σ) and B–O (π), in Fig. 11) and narrow B–O (σ*) and B–O (π*) bands formed mainly by e_g- and t_{2g}-orbitals of d metal.

The degree of filling of the B–O (σ*) and B–O (π*) bands is determined by the number of valence electrons of the d-block metal cation, and the band width depends, in particular, on the degree of overlap of t_{2g}- and e_g-orbitals of the d metal with oxygen 2p-orbitals. The degree of overlap in oxides with the perovskite structure is affected by the degree of distortion of the structure determined by the *t* factor, because a strong distortion, as mentioned above (see Section 3), leads to a decrease in the B–O–B angle between the vertex-sharing BO_6 octahedra.

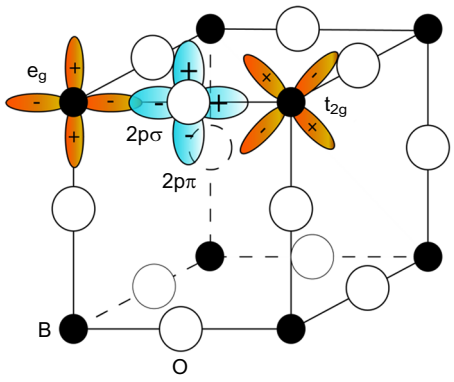


Figure 10. Schematic diagram of σ- and π-interactions between metal d-orbitals and oxygen 2p-orbitals in the perovskite structure. The A cation is omitted for clarity. The e_g-orbitals of the d metal directly pointed towards oxygen ions are involved in the formation of σ-bonds; t_{2g}-orbitals, of π-bonds.

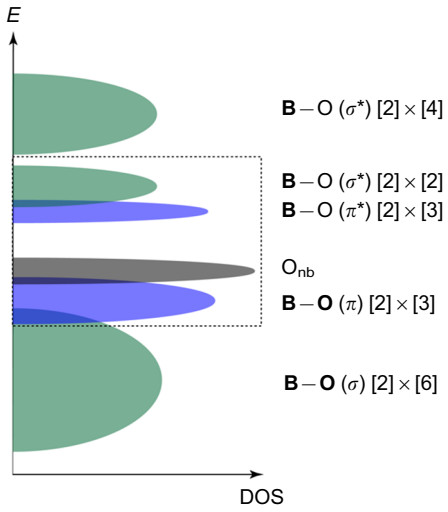


Figure 11. Schematic of the electronic structure of perovskite ABO_3. The bands formed through σ- and π-interactions between 3d-metal and oxygen atomic orbitals of the right symmetry are in green and blue, respectively. The ions that make the main contribution to the formation of the corresponding band are in bold-face. The band formed by oxygen nonbonding (nb) orbitals is highlighted in black. The electron capacity of each band is given in brackets. A fragment of valence bands, which are considered in the description of the electronic structure of perovskite, is enclosed by a dashed-line rectangle. *E* is the energy, DOS is the density of states.

Therefore, for perovskites with the same B cation and containing a rare-earth metal ion as the A cation, the valence band width would be expected to increase with increasing radius of R^{3+}.[92] Perovskites $RNiO_3$ exhibiting the semiconductor to metal transition with increasing radius of the R cation from Sm^{3+} to La^{3+} is a good illustration of this correlation.[93]

In this model, the electron capacity of the B–O (π*) and B–O (σ*) bands is six and four electrons, respectively. Consequently, it could be expected that perovskites containing B cations with an odd number of valence d electrons, for example, in $LaCrO_3$ containing the Cr^{3+} cation with the electronic configuration $[Ar]3d^3$, will have the partially filled valence band [in this example, the half-filled B–O (π*) valence band] and possess metallic conductivity. However, this is not true because the proposed one-electron model of the band structure does not take into account interelectronic interactions, which play a significant role in the case of d metals.

The above-considered one-electron model of the electronic structure of oxides does not take into account strong repulsion between electrons in the d-orbitals of the B cation. This Coulomb interaction can be taken into account using the intra-atomic Hubbard energy (*U*). For the multielectron atom, *U* is the energy required to transfer an electron from one atom to another. This energy is equal to the energy difference between the ionization potential and electron affinity.[94] At high Hubbard energies, the electronic states can be localized, and the oxide will behave as the insulator even if it has an odd number of valence d electrons. This is associated with the splitting of the d band into a lower Hubbard band (LHB) and an upper Hubbard band (UHB) at high *U* values. The schematic of this splitting and the

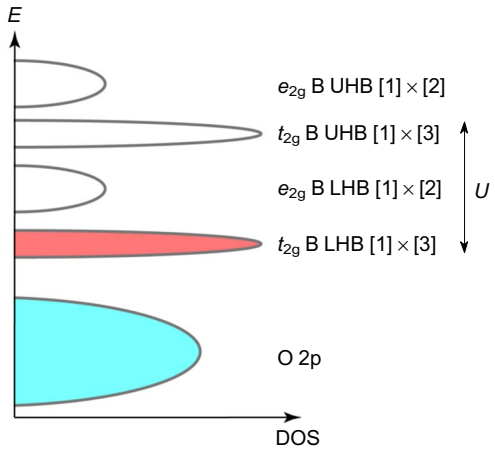


Figure 12. Schematic of the electronic structure of $LaCrO_3$. The completely filled t_{2g} B LHB band can contain only three electrons.

formation of an insulating ground state in relation to perovskite $LaCrO_3$ is shown in Fig. 12.

The electronic structure of valence bands of d-metal oxides depends on the mutual arrangement of the energy levels of oxygen and d metal. According to the scheme proposed by Zaanen, Sawatzky and Allen,[95] d-block metal oxides can be divided into Mott – Hubbard and charge-transfer insulators. If the energy difference between the occupied electronic states of oxygen and vacant states of the d-block metal cation (Δ) is large, being larger than the Hubbard energy (Fig. 13 *a*), the materials are considered as Mott – Hubbard insulators. Chemical redox processes involving these oxides occur with changes in the filling of the electronic levels of the d metal. Early 3d-metal oxides, for example, titanium oxides in low oxidation states ($LaTiO_3$),[96] are Mott – Hubbard insulators. If $U > \Delta$, materials are charge-transfer insulators (Fig. 13 *b*). Redox processes involving such oxides are accompanied by changes in the electronic state of oxygen. Hence, such oxides are prone to form oxygen vacancies in the structure.

Actually, an increase in the average formal oxidation state of the d-metal cation as a result of the heterovalent A cation substitution, for example, in $La_{1-x}Sr_xCoO_3$, will lead to the removal of electrons from the band with a significant contribution of the electronic states of oxygen. This will lead to a change in the charge state of oxygen,

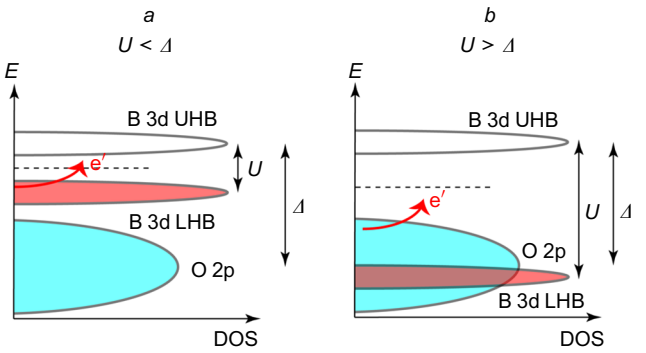


Figure 13. Schematic of the electronic structures of the Mott – Hubbard insulator (*a*) and the charge-transfer insulator (*b*). The Fermi level is indicated by a dashed line.[92]

which finally can result in its partial removal from the structure, *i.e.*, to the formation of oxygen vacancies. From the above it follows, that the position of the energy level of the electronic states of oxygen in oxide should correlate with the ease of the formation of oxygen vacancies. This correlation was described by Lee *et al.*[97] as the dependence of the enthalpy of the formation of oxygen vacancies as a function of the position of the band centre of electronic states of oxygen with respect to the Fermi level [E(O2p)]. The shift of the band centre of the electronic states of oxygen with respect to the Fermi level (Fig. 14), which is indicative of an increase in the fraction of the covalent component in the B – O bond, facilitates the formation of oxygen vacancies in the crystal structure of perovskite. The practically important consequence of this fact is an increase in the catalytic activity of oxide in the high-temperature oxygen reduction at the cathode.[97]

The tendencies of the changes in the U and Δ values for elements of the Periodic table are worth noting. On moving along the row of the Periodic table, the Hubbard energy increases due to the d contraction. Meanwhile, a decrease in the radius of the d-metal cation leads to a decrease in the energy difference between the orbitals of oxygen and d metal (*i.e.*, to an increase in the degree of B – O bond covalence) and a decrease in Δ. Hence, it would be expected that oxides of late 3d elements (Fe, Co, Ni, Cu) are charge-transfer insulators characterized by the formation of oxygen vacancies. While moving down along the group of the Periodic table, the energy difference between the orbitals of oxygen and d metal increases (the degree of B – O bond ionicity increases) and, correspondingly, Δ increases. An increase in the radius of the cation on moving down along the group leads to a decrease in U. Hence, it would be expected that 4d- and 5d-metal oxides will behave as Mott – Hubbard insulators.

The above-considered tendencies of the changes in the U and Δ values are true for oxides containing d-metal cations in the same oxidation state. An increase in the oxidation state of the B cation would be expected to lead to a decrease in the B – O bond length, an increase in the degree of bond

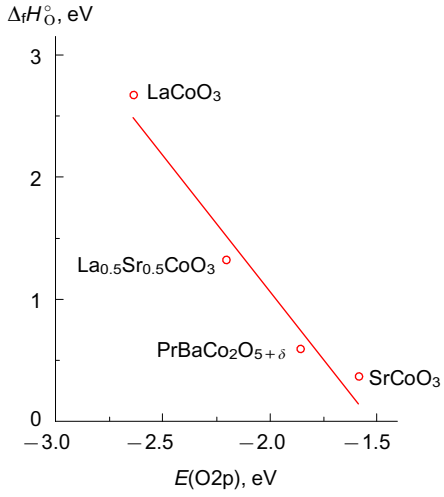


Figure 14. Enthalpies of formation of oxygen vacancies ($\Delta_f H^\circ_O$) in the structures of cobalt-containing perovskites as a function of the energy levels of oxygen (the electron band centre) with respect to the Fermi level.[92]

covalence and the possible change in the behaviour from that typical of Mott – Hubbard insulators to that characteristic of charge-transfer insulators. For example, this transition was shown [98] for perovskites $La_{1-x}Sr_xFe_{2/3}Mo_{1/3}O_3$, where the oxidation state of molybdenum increases from +3 ($x = 0.0$) to +6 ($x = 1.0$) (the oxidation state of iron is close to +3 in the whole composition range).

Therefore, perovskites with a large contribution of a covalent component in the B—O bond (charge-transfer insulators) may be of most interest as electrode materials for S-SOFCs, particularly for intermediate-temperature SOFCs. On the one hand, having wide B—O (σ*) and B—O (π*) bands, these compounds can possess high electronic conductivity. On the other hand, due to the ease of the formation of oxygen vacancies, they can have oxygen-ion conductivity. Such oxides include Fe-, Co-, Ni- and Cu-containing perovskite-like oxides, among which only iron-containing perovskites are stable under reducing atmosphere at high temperature. Manganese-containing perovskites also belong to charge-transfer insulators, and they can contain oxygen vacancies. Besides, as shown above (see Section 4), they are thermodynamically more stable compared to ferrites. It is worth noting that the oxygen exchange kinetics in manganites strongly depends on their crystal structures and, as shown below (see Section 6.3), oxides $RBaMn_2O_{5+\delta}$ with an ordered double perovskite structure (see Fig. 6 *b*) are of great interest as electrode materials for S-SOFCs.

6. Electrode materials for symmetrical solid oxide fuel cells based on oxides with the perovskite structure and of other structure types

Most studies on electrode materials for S-SOFCs address oxides ABO_3 with the perovskite structure containing titanium, vanadium, chromium, manganese and iron cations in the B-site. These perovskites proved to be most stable at high temperatures under an atmosphere of cathode and anode gases. An analysis of the literature data published in the past five years shows that iron-containing perovskites are of most interest. As mentioned above, this is due to the ease of the change in the coordination number from 6 to 4 characteristic of iron cations in the oxygen coordination environment, resulting in the appearance of oxygen-ion conductivity in the electrode material and promoting the change in the mechanism of the electrode reaction. This leads to higher efficiency of such materials for SOFCs and, consequently, many iron-containing perovskites, *e.g.*, $La_{0.6}Sr_{0.4}Co_{0.2}Fe_{0.8}O_{3-\delta}$ (LSCF), are used as conventional cathode materials for intermediate-temperature SOFCs.

Hence, we decide to move away from the existing order of consideration of electrode materials for S-SOFCs, starting from perovskites containing early 3d-metal ions as B cations, and begin with iron-containing perovskites.

6.1. Materials based on iron-containing perovskites $A(Fe,B)O_{3-\delta}$

The main advantage of iron-containing perovskites as electrode materials for S-SOFCs is the oxygen-ion conductivity. Besides, the possibility of the existence of large oxygen nonstoichiometry results in that iron-containing perovskites have large thermal expansion coefficients due to the chemical expansion effect, particularly at high temperatures and under reducing atmosphere (Table 2). Perovskites $R_{1-x}A_xFeO_{3-\delta}$, where R is a rare-earth element and A is an alkaline-earth metal cation, are p-type conductors, and their high-temperature electrical conductivity in air is often higher than 100 S cm^{-1}. On the contrary, the electrical conductivity sharply decreases under reducing atmosphere, and its value is rarely higher than 1 S cm^{-1} (see Table 2).

As opposed to cobalt- and nickel-containing perovskites, perovskite-like ferrites are quite stable under reduc-

Table 2. Electrical conductivities (σ) and TEC values of electrode materials based on iron-containing perovskites $A(Fe,B)O_{3-\delta}$ under oxidizing and reducing atmosphere.

Composition of the material	T, °C	Atmosphere	σ, S cm^{-1}	Thermal expansion		Ref.
				temperature range, °C	TEC × 10^6, K^{-1}	
$La_{0.8}Sr_{0.2}FeO_{3-\delta}$	800	Air	141.1	–	–	99
	800	Wet H_2	0.138	–	–	99
$La_{0.6}Sr_{0.4}Fe_{0.9}Sc_{0.1}O_{3-\delta}$	800	Air	98	–	–	100
	800	H_2	0.69	–	–	100
$La_{0.7}Sr_{0.3}Fe_{0.7}Ga_{0.3}O_{3-\delta}$	800	Air	47.45	200 – 800	13.79	101
	800	Ar + H_2 (5%)	0.422	200 – 800	13.88	101
$LaSr_2Fe_2CrO_{9-\delta}$	800	Air	75	–	–	102
	800	Wet H_2	0.16	–	–	102
$Pr_{0.52}Ca_{0.48}Fe_{0.52}Mg_{0.26}Mo_{0.22}O_3$	900	Air	0.15	25 – 900	12.47	103
	900	Ar + H_2 (8%)	–	25 – 900	11.05	103
$Pr_{0.5}Ca_{0.5}Fe_{0.6}Mg_{0.2}Mo_{0.2}O_3$	900	Air	–	150 – 300	11.7	103
			–	500 – 900	12.95	103
	900	Ar + H_2 (8%)	–	150 – 300	11.7	103
			–	300 – 900	14.96	103
$La_{0.3}Ca_{0.7}Fe_{0.6}Mg_{0.175}Mo_{0.225}O_{3-\delta}$	900	Air	4.6	127 – 900	12.7	104, 105
	900	Ar + H_2 (8%)	25	127 – 427	12.6	104, 105
				427 – 900	17.1	104, 105
$La_{0.3}Ca_{0.7}Fe_{0.55}Co_{0.05}Mg_{0.175}Mo_{0.225}O_{3-\delta}$	900	Air	1	127 – 900	13.1	105
	900	Ar + H_2 (8%)	8.8	–	–	105

Table 2 (continued).

Composition of the material	T, °C	Atmosphere	σ, S cm^{-1}	Thermal expansion		Ref.
				temperature range, °C	TEC × 10^6, K^{-1}	
$Sm_{0.8}Sr_{0.2}Fe_{0.8}Ti_{0.15}Ru_{0.05}O_{3-\delta}$	800	Air	~200	25 – 900	11.09	106
	800	Ar + H_2 (5%)	1.16	25 – 900	11.52	106
$La_{0.6}Sr_{0.4}Co_{0.2}Fe_{0.6}Nb_{0.2}O_{3-\delta}$	800	Air	5.05	30 – 900	14.3	107
	800	Ar + H_2 (5%)	0.37	30 – 900	13.8	107
$(La_{0.6}Sr_{0.4})_{0.95}Co_{0.2}Fe_{0.6}Nb_{0.2}O_{3-\delta}$	800	Air	3.42	30 – 900	13.8	107
	800	Ar + H_2 (5%)	0.46	30 – 900	13.4	107
$(La_{0.6}Sr_{0.4})_{0.9}Co_{0.2}Fe_{0.6}Nb_{0.2}O_{3-\delta}$	800	Air	2.67	30 – 900	13.9	107
	800	Ar + H_2 (5%)	0.59	30 – 900	14.1	107
$La_{0.6}Sr_{0.4}Co_{0.2}Fe_{0.7}Mo_{0.1}O_{3-\delta}$	800	Air	~8.1	30 – 850	12.9	108
	800	Ar + H_2 (5%)	~3.2	30 – 850	13.3	108
$PrBaFe_2O_{5+\delta}$	500	Air	12.6	100 – 300	12.4	109
				300 – 800	19.5	109
$PrBaFe_{1.6}Ni_{0.4}O_{5+\delta}$	350	Air	89	100 – 300	10.1	109
				300 – 800	16.6	109
$La_{0.5}Sr_{0.5}Fe_{0.8}Cu_{0.2}O_{3-\delta}$	–	Air	–	25 – 900	17.7	110
$La_{0.7}Sr_{0.3}Fe_{0.9}Ni_{0.1}O_{3-\delta}$	800	Air	~250	–	–	111
	800	Ar + H_2 (5%)	0.61	–	–	111
$La_{0.6}Ce_{0.1}Sr_{0.3}Fe_{0.9}Ni_{0.1}O_{3-\delta}$	800	Air	~120	–	–	111
	800	Ar + H_2 (5%)	0.45	–	–	111
$Pr_{0.5}Ba_{0.5}Co_{0.25}Fe_{0.75}O_{3-\delta}$	500	Air	~300	–	–	112
	700	Ar + H_2 (5%)	9.92	–	–	112
$Pr_{0.6}Sr_{0.4}Fe_{0.8}Ni_{0.2}O_{3-\delta}$	600	Air	320.8	25 – 700	13.4	113
				700 – 1000	25	113
$Pr_{0.6}Sr_{0.4}Fe_{0.7}Ni_{0.2}Mo_{0.1}O_{3-\delta}$	700	Air	70.1	25 – 700	12.7	113
				700 – 1000	18.3	113
$(Pr_{0.4})_xSr_{0.6}Co_{0.2}Fe_{0.7}Nb_{0.1}O_{3-\delta}$	800	Air	~125	20 – 900	18.02 – 18.07	114
(x = 0.9, 0.95, 1.0, 1.05)	800	Ar + H_2 (5%)	~25		–	114
$Pr_{0.4}Sr_{0.6}(Co_{0.2}Fe_{0.8})O_{3-\delta}$	850	Air	180.4	100 – 500	14.50	115
				500 – 900	26.03	115
$Pr_{0.4}Sr_{0.6}(Co_{0.2}Fe_{0.8})_{0.95}Mo_{0.05}O_{3-\delta}$	850	Air	128.8	–	–	115
$Pr_{0.4}Sr_{0.6}(Co_{0.2}Fe_{0.8})_{0.9}Mo_{0.1}O_{3-\delta}$	850	Air	91.7	100 – 500	14.83	115
				500 – 900	18.92	115
$La_{0.4}Sr_{0.6}Co_{0.2}Fe_{0.7}Nb_{0.1}O_{3-\delta}$	700	Air	271	–	–	116
	700	Ar + H_2 (5%)	35.8	–	–	116
	800	Air	182	–	–	117
$La_{0.4}Sr_{0.6}Co_{0.2}Fe_{0.7}Nb_{0.1}O_{3-\delta}$–GDC (50 : 50 mass %) [a]	800	Air	37	–	–	117
$Ba_{0.5}Sr_{0.5}Fe_{0.8}Cu_{0.1}Ti_{0.1}O_{3-\delta}$	800	Air	~6	50 – 600	19.4	118
	800	Ar	~1.1	600 – 950	42.9	118
$La_{0.5}Ba_{0.5}Fe_{0.5}Ti_{0.5}O_{3-\delta}$	800	Air	~0.3	303 – 923	11.82	119
				923 – 1223	13.26	119
				1223 – 1373	14.11	119
$(La_{0.5}Ca_{0.5})_{0.95}Fe_{0.5}Cr_{0.5}O_{3-\delta}$	800	Air	~30	303 – 923	10.87	119
	950	Ar	~9	923 – 1223	13.3	119
				1223 – 1373	15.2	119

[a] The electrolyte material is $Ce_{0.9}Gd_{0.1}O_{2-\delta}$. Since the oxygen content of CeO_2 strongly depends on the temperature and the partial pressure of oxygen, from here on we give the chemical formulas of doped cerium oxide taking into account the variable oxygen content.

ing atmosphere. However, their stability is limited and depends on the nature of the A cation and on the temperature and composition of the gas atmosphere. The literature data on the stability of these materials in hydrogen are often contradictory. For instance, Tian *et al.*[99] reported that $La_{0.8}Sr_{0.2}FeO_{3-\delta}$ is stable during annealing under wet hydrogen at 800 °C for 10 h; the R_η value of the electrode material/YSZ interface with a buffer GDC layer in air and under wet hydrogen is 0.30 and 0.58 Ω cm^2, respectively (Table 3), and the power density of the model S-SOFC reaches 387 mW cm^{-2} with an electrolyte thickness (L_e) of 400 μm (Table 4). On the contrary, it was stated [100, 121] that $La_{0.9}Ca_{0.1}FeO_{3-\delta}$ and $La_{0.6}Sr_{0.4}FeO_{3-\delta}$ decomposed during annealing under hydrogen atmosphere at 850 °C (4 h) and 800 °C (10 h), respectively, to form ferrites $(La,A)_2FeO_4$. Fan *et al.*[120] demonstrated that $Sm_{0.95}Ce_{0.05}FeO_{3-\delta}$ is stable at 850 °C (10 h) under reducing atmosphere and also towards the reaction with YSZ, Therefore,

Table 3. Polarization resistance values of electrode materials based on iron-containing perovskites $A(Fe,B)O_{3-\delta}$ under oxidizing and reducing atmosphere.

Composition of the material	Electrolyte	T, °C	Atmosphere	R_η, Ω cm^2	Ref.
Materials for symmetrical SOFCs					
$La_{0.8}Sr_{0.2}FeO_{3-\delta}$	YSZ/GDC [a]	800	Air	0.30	99
	YSZ/GDC [a]	800	Wet H_2	0.58	99
$Sm_{0.95}Ce_{0.05}FeO_{3-\delta}$	YSZ	800	Air	0.15	120
	YSZ	800	Ar + H_2 (5%)	0.08	120
$Sm_{0.95}Ce_{0.05}FeO_{3-\delta}$ – YSZ (7 : 3 mass %)	YSZ	800	Air	0.08	120
	YSZ	800	Ar + H_2 (5%)	0.05	120
$La_{0.9}Ca_{0.1}Fe_{0.9}Nb_{0.1}O_{3-\delta}$ (see [b])	SSZ [c]	850	Air	0.66	121
	SSZ [c]	850	H_2	0.12	121
$La_{0.9}Ca_{0.1}Fe_{0.9}Nb_{0.1}O_{3-\delta}$ – SDC [b]	SSZ [c]	850	Air	0.12	121
	SSZ [c]	850	H_2	0.06	121
$La_{0.6}Sr_{0.4}Fe_{0.9}Sc_{0.1}O_{3-\delta}$	LSGM [d]	800	Air	0.015	100
	LSGM [d]	800	Wet H_2	0.29	100
$La_{0.3}Sr_{0.7}Ti_{0.3}Fe_{0.7}O_3$	YSZ/GDC [a]	800	Air	0.11	122
	YSZ/GDC [a]	800	Wet H_2	0.25	122
$LaSr_2Fe_2CrO_{9-\delta}$	LSGM	800	Air	0.29	102
	LSGM	800	Wet H_2	0.57	102
$LaSr_2Fe_2CrO_{9-\delta}$ – GDC (50 : 59 mass %)	LSGM	800	Air	0.24	102
	LSGM	800	Wet H_2	0.36	102
$Sm_{0.9}Sr_{0.1}Fe_{0.9}Ru_{0.1}O_{3-\delta}$	SDC	800	Air	0.16	123
	SDC	800	Wet H_2	0.20	123
$Sm_{0.8}Sr_{0.2}Fe_{0.8}Ti_{0.15}Ru_{0.05}O_{3-\delta}$	SDC	800	Air	0.16	106
	SDC	800	Ar + H_2 (5%)	0.19	106
	SDC	800	Wet H_2	0.65	106
$La_{0.3}Ca_{0.7}Fe_{0.6}Mg_{0.175}Mo_{0.225}O_{3-\delta}$	GDC	900	Air	3.6	105
$La_{0.3}Ca_{0.7}Fe_{0.55}Co_{0.05}Mg_{0.175}Mo_{0.225}O_{3-\delta}$	GDC	900	Air	1.2	105
$La_{0.6}Sr_{0.4}Co_{0.2}Fe_{0.6}Nb_{0.2}O_{3-\delta}$	LSGM/SDC [a]	800	Air	0.355	107
	LSGM/SDC [a]	800	H_2	0.592	107
$(La_{0.6}Sr_{0.4})_{0.95}Co_{0.2}Fe_{0.6}Nb_{0.2}O_{3-\delta}$	LSGM/SDC [a]	800	Air	0.215	107
	LSGM/SDC [a]	800	H_2	0.501	107
$(La_{0.6}Sr_{0.4})_{0.9}Co_{0.2}Fe_{0.6}Nb_{0.2}O_{3-\delta}$	LSGM/SDC [a]	800	Air	0.164	107
	LSGM/SDC [a]	800	H_2	0.382	107
$La_{0.6}Sr_{0.4}Co_{0.2}Fe_{0.7}Mo_{0.1}O_{3-\delta}$	LSGM/SDC [a]	800	Air	0.041	108
	LSGM/SDC [a]	800	H_2	0.266	108
$PrBa(Fe_{0.8}Sc_{0.2})_2O_{5+\delta}$	LSGM	800	Air	0.05	124
	LSGM	800	Wet H_2	0.18	124
$PrBaFe_2O_{5+\delta}$	SDC	650	Air	1.452	109
	SDC	650	H_2	0.075	109
$PrBaFe_{1.6}Ni_{0.4}O_{5+\delta}$	SDC	650	Air	3.89	109
	SDC	650	H_2	0.034	109
Materials for pseudosymmetrical SOFCs					
$LaNi_{0.82}Fe_{0.18}O_3$ – NiO	LSGM	650	Air	0.35	125
	LSGM	650	H_2	0.12	125
$La_{0.6}Ca_{0.4}Fe_{0.8}Ni_{0.2}O_{3-\delta}$ – SDC (70 : 30 mass %)	SDC	800	Air	0.12	126
$Pr_{0.5}Ba_{0.5}Co_{0.25}Fe_{0.75}O_{3-\delta}$ – GDC (60 : 40 mass %)	SSZ/GDC	700	Air	0.04	112
	SSZ/GDC	700	Wet H_2	0.21	112
$Pr_{0.6}Sr_{0.4}Fe_{0.8}Ni_{0.2}O_{3-\delta}$	LSGM/GDC [a]	800	Air	~0.25	113
	LSGM/GDC [a]	800	Wet H_2	~0.25	113
$Pr_{0.6}Sr_{0.4}Fe_{0.7}Ni_{0.2}Mo_{0.1}O_{3-\delta}$	LSGM/GDC [a]	800	Air	~0.5	113
	LSGM/GDC [a]	800	Wet H_2	~0.25	113
$(Pr_{0.4})_xSr_{0.6}Co_{0.2}Fe_{0.7}Nb_{0.1}O_{3-\delta}$	LSGM	850	O_2	0.012 – 0.022	114
(x = 0.9, 0.95, 1.0, 1.05 and 1.1)	LSGM	850	Wet H_2	0.15 – 0.38	114
$Pr_{0.4}Sr_{0.6}(Co_{0.2}Fe_{0.8})_{0.95}Mo_{0.05}O_{3-\delta}$	LSGM	900	Air	0.014	115
	LSGM	900	Wet H_2	0.31	115
$Pr_{0.4}Sr_{0.6}Co_{0.2}Fe_{0.7}Nb_{0.1}O_{3-\delta}$ – GDC	LSGM	800	Air	0.044	127
	LSGM	800	Wet H_2	0.309	127
$La_{0.4}Sr_{0.6}Co_{0.2}Fe_{0.7}Nb_{0.1}O_{3-\delta}$	LSGM	800	Air	0.1	128

Table 3 (continued).

Composition of the material	Electrolyte	T, °C	Atmosphere	R_η, Ω cm^2	Ref.
Materials for pseudosymmetrical SOFCs					
$La_{0.4}Sr_{0.6}Co_{0.2}Fe_{0.7}Nb_{0.1}O_{3-\delta}$ – GDC	YSZ/GDC [a]	800	Air	0.034	129
$La_{0.4}Sr_{0.6}Co_{0.2}Fe_{0.7}Nb_{0.1}O_{3-\delta}$ – GDC (50 : 50 mass %)	YSZ/GDC [a]	800	Air	0.16	117
$La_{0.4}Sr_{0.6}Co_{0.2}Fe_{0.7}Nb_{0.1}O_{3-\delta}$	YSZ/GDC [a]	800	Air	0.62	117
$Ba_{0.5}Sr_{0.5}Fe_{0.8}Cu_{0.1}Ti_{0.1}O_{3-\delta}$	GDC	750	Air	0.013	118

[a] The GDC, $Ce_{0.8}Sm_{0.2}O_{2-\delta}$ (SDC) or $La_{0.4}Ce_{0.6}O_{2-\delta}$ (LCO) protective layer. [b] Impregnated in the porous $Zr_{0.8}Sc_{0.2}O_{1.9}$ (SSZ) layer. [c] A copper metal layer (current collector) was deposited on the support. [d] The three-layer electrolyte $La_{0.9}Sr_{0.1}Ga_{0.8}Mg_{0.2}O_{2.85}$ (LSGM) composed of an 18-μm dense layer between two porous 200-μm LSGM layers.

Table 4. Specific power density of S-SOFCs (P_{max}) with electrode materials based on iron-containing perovskites $A(Fe,B)O_{3-\delta}$.

Composition of the electrode	Electrolyte	Current collector	Fuel	T, °C	P_{max}, mW cm^{-2}	L_e, μm	Ref.
Materials for symmetrical SOFCs							
$La_{0.8}Sr_{0.2}FeO_{3-\delta}$	YSZ/GDC [a]	Ag	Wet H_2	800	387	400	99
$Sm_{0.95}Ce_{0.05}FeO_{3-\delta}$	YSZ	Pt	H_2	800	130	700	120
$Sm_{0.95}Ce_{0.05}FeO_{3-\delta}$ – YSZ (7 : 3 mass %)	YSZ	Pt	H_2	800	193	700	120
$La_{0.9}Ca_{0.1}Fe_{0.9}Nb_{0.1}O_{3-\delta}$ (see [b])	SSZ	Ag	H_2	850	392	60	121
$La_{0.9}Ca_{0.1}Fe_{0.9}Nb_{0.1}O_{3-\delta}$ – SDC [b]	SSZ	Ag	H_2	850	528	60	121
	SSZ	Ag	CO	850	518.7	60	121
	SSZ	Ag	CO + H_2 (1 : 1)	850	523.4	60	121
$La_{0.6}Sr_{0.4}Fe_{0.9}Sc_{0.1}O_{3-\delta}$	LSGM	Ag [c]	Wet H_2	800	540 [d]	–	100
$La_{0.3}Sr_{0.7}Ti_{0.3}Fe_{0.7}O_3$	YSZ/GDC [a]	Ag	Wet H_2	800	215	400	122
$La_{0.3}Sr_{0.7}Ti_{0.3}Fe_{0.7}O_{3-\delta}$ – CeO_2	SSZ	Ag	CO + CO_2 (1 : 1)	850	357	70	122
$La_{0.7}Sr_{0.3}Fe_{0.7}Ga_{0.3}O_{3-\delta}$	LSGM	Ag	Wet H_2	800	489	320	101
$LaSr_2Fe_2CrO_{9-\delta}$	LSGM/LCO [a]	Ag	Wet H_2	800	224	500	102
$LaSr_2Fe_2CrO_{9-\delta}$ – GDC (50 : 50 mass %)	LSGM/LCO [a]	Ag	Wet H_2	800	264	500	102
$Sm_{0.9}Sr_{0.1}Fe_{0.9}Ru_{0.1}O_{3-\delta}$	SDC	Pt	Wet H_2	800	119.69	600	123
$Sm_{0.8}Sr_{0.2}Fe_{0.8}Ti_{0.15}Ru_{0.05}O_{3-\delta}$	SDC	Au	Wet H_2	800	271	600	106
$Sm_{0.7}Sr_{0.2}Fe_{0.8}Ti_{0.15}Ru_{0.05}O_{3-\delta}$	SDC	Au	Wet H_2	800	417	600	106
$(La_{0.6}Sr_{0.4})_{0.9}Co_{0.2}Fe_{0.6}Nb_{0.2}O_{3-\delta}$	LSGM/SDC [a]	Ag	H_2	800	539	200	107
	LSGM/SDC [a]	Ag	CO : H_2	800	207	200	107
	LSGM/SDC [a]	Ag	Wet CH_4	800	126	200	107
	LSGM/SDC [a]	Ag	Bioethanol	800	62	200	107
$La_{0.6}Sr_{0.4}Co_{0.2}Fe_{0.7}Mo_{0.1}O_{3-\delta}$	LSGM/SDC [a]	Ag	H_2	800	737	270	108
	LSGM/SDC [a]	Ag	Ethanol	800	405	270	108
	LSGM/SDC [a]	Ag	LPG (liquefied petroleum gas)	800	394	270	108
$PrBa(Fe_{0.8}Sc_{0.2})_2O_{5+\delta}$	LSGM	–	Wet H_2	850	921	275	124
	LSGM	–	Wet H_2	800	713	275	124
	LSGM	–	Wet H_2	750	398	275	124
$PrBaFe_2O_{5+\delta}$	SDC	Ag	Wet H_2	650	70	–	109
$PrBaFe_{1.6}Ni_{0.4}O_{5+\delta}$	SDC	Ag	Wet H_2	650	49	–	109
$PrBaFe_2O_{5+\delta}$ (cathode), $PrBaFe_{1.6}Ni_{0.4}O_{5+\delta}$ (anode)	SDC	Ag	Wet H_2	650	120	–	109
Materials for pseudosymmetrical SOFCs							
$LaCo_{0.3}Fe_{0.67}Pd_{0.03}O_{3-\delta}$ (see [e])	SDC	Ag	Wet H_2	750	535	300	130
$La_{0.5}Sr_{0.5}Fe_{0.8}Cu_{0.2}O_{3-\delta}$	SSZ/SDC [a]	–	Wet H_2	800	577	230	110
	SSZ/SDC [a]	–	Wet H_2 + CO (1 : 1)	800	482	230	110
$LaNi_{0.82}Fe_{0.18}O_3$ – NiO [f]	LSGM	Ag	H_2	650	928	20	125
$La_{0.6}Ca_{0.4}Fe_{0.8}Ni_{0.2}O_{3-\delta}$ – SDC	SDC	Ag	H_2	800	303	280	126
$La_{0.6}Ce_{0.1}Sr_{0.3}Fe_{0.9}Ni_{0.1}O_{3-\delta}$	LSGM	Ag	Wet CH_4	850	522	300	111
	LSGM	Ag	Wet H_2	850	889	300	111
$La_{0.7}Sr_{0.3}Fe_{0.9}Ni_{0.1}O_{3-\delta}$	LSGM	Ag	Wet CH_4	850	221	300	111
	LSGM	Ag	Wet H_2	850	907	300	111
$La_{0.6}Sr_{0.4}Fe_{0.9}Ni_{0.1}O_{3-\delta}$ (see [g])	YSZ	Ag	H_2	750	280	15	131
	YSZ	Ag	Wet CH_4	750	230	15	131
	YSZ	Ag	Wet C_3H_8	750	400	15	131

Table 4 (continued).

Composition of the electrode	Electrolyte	Current collector	Fuel	T, °C	P_{max}, mW cm^{-2}	L_e, μm	Ref.
Materials for pseudosymmetrical SOFCs							
$PrNi_{0.4}Fe_{0.6}O_{3-\delta}$	LSGM	Ag	Wet CH_4	800	663	30	132
$Pr_{0.5}Ba_{0.5}Co_{0.25}Fe_{0.75}O_{3-\delta}$–GDC (60 : 40 mass %)	LSGM	Ag	Wet H_2	700	500	300	112
$Pr_{0.6}Sr_{0.4}Fe_{0.8}Ni_{0.2}O_{3-\delta}$	LSGM/GDC [a]	Ag	Wet H_2	800	435	320	113
$Pr_{0.6}Sr_{0.4}Fe_{0.7}Ni_{0.2}Mo_{0.1}O_{3-\delta}$	LSGM/GDC [a]	Ag	Wet H_2	800	500	320	113
$Pr_{0.42}Sr_{0.6}Co_{0.2}Fe_{0.7}Nb_{0.1}O_{3-\delta}$	LSGM	Pt	Wet H_2 (O_2 at cathode)	850	940	245	114
	LSGM	Pt	Wet CH_4	900	670	245	114
$Pr_{0.4}Sr_{0.6}(Co_{0.2}Fe_{0.8})_{0.95}Mo_{0.05}O_{3-\delta}$	LSGM	Pt	Wet H_2	850	493	293	115
	LSGM	Pt	CH_4		160	293	115
$Pr_{0.42}Sr_{0.6}Co_{0.2}Fe_{0.7}Nb_{0.1}O_{3-\delta}$	LSGM	Pt	Wet H_2 (O_2 at cathode)	900	1133	265	133
$La_{0.4}Sr_{0.6}Co_{0.2}Fe_{0.7}Nb_{0.1}O_{3-\delta}$	LSGM	–	H_2	850	500	300	128
$La_{0.4}Sr_{0.6}Co_{0.2}Fe_{0.7}Nb_{0.1}O_{3-\delta}$–GDC [h]	LSGM	See [i]	Wet H_2	850	817	300	134
	LSGM	See [i]	CH_4	850	280	300	134
	LSGM	See [i]	CH_4 (90%) + CO_2 (10%)	850	455	300	134
$La_{0.4}Sr_{0.6}Co_{0.2}Fe_{0.7}Nb_{0.1}O_{3-\delta}$–GDC	YSZ/GDC [a]	Ag	Wet H_2	850	348	200	129
			Wet C_3H_8	850	324	200	129
$La_{0.4}Sr_{0.6}Co_{0.2}Fe_{0.7}Nb_{0.1}O_{3-\delta}$	YSZ/GDC [a]	–	Wet H_2	850	284	200	117
$La_{0.4}Sr_{0.6}Co_{0.2}Fe_{0.7}Nb_{0.1}O_{3-\delta}$–GDC (50 : 50 mass %)	YSZ/GDC [a]	–	Wet H_2	850	395	200	117
			Wet CH_4	850	124	200	117
$Ba_{0.5}Sr_{0.5}Fe_{0.8}Cu_{0.1}Ti_{0.1}O_{3-\delta}$	GDC	–	H_2	800	480	300	118

[a] The GDC, SDC or LCO protective layer. [b] Impregnated in the porous SSZ layer. [c] A copper metal layer (current collector) was deposited on the support. [d] The three-layer LSGM electrolyte composed of an 18-μm dense layer between two porous 200-μm LSGM layers. [e] Impregnated in the porous SDC layer. [f] Impregnated in the porous LSGM layer. [g] Impregnated in the porous YSZ layer. [h] Au as the anode current collector, Pt as the cathode current collector. [i] Pt as the cathode, Au as the anode.

composites with YSZ can be used as electrode materials for S-SOFCs (see Tables 3 and 4).

The main approach to increasing the stability of iron-containing perovskites under reducing atmosphere is based on the partial replacement of iron ions by cations with stable oxidation states under these conditions, such as Mg^{2+}, Sc^{3+}, Ti^{4+}, Nb^{5+}.[135,136] Thus, the replacement of 10% of iron ions by niobium and scandium cations, according to the formulas $La_{0.9}Ca_{0.1}Fe_{0.9}Nb_{0.1}O_{3-\delta}$ and $La_{0.6}Sr_{0.4}Fe_{0.9}Sc_{0.1}O_{3-\delta}$, respectively, leads to stabilization of perovskites under reducing atmosphere.[100,121] These oxides have reasonable electrical conductivity, and the polarization resistance of the electrode/electrolyte interface is low, particularly, in the case of composites with electrolyte materials (see Table 3). The power density of S-SOFCs with such materials is as high as 500 mW cm^{-2}; in the case of the composite $La_{0.9}Ca_{0.1}Fe_{0.9}Nb_{0.1}O_{3-\delta}$–SDC, this parameter depends only slightly on the nature of the fuel used (see Table 4).

Among Ti-substituted ferrites, perovskite $La_{0.3}Sr_{0.7}Ti_{0.3}Fe_{0.7}O_3$ (LSTF) showed stability in a wet Ar + H_2 gas mixture (20%) at 800 °C (20 h) and also had reasonable R_η values of the LSTF/YSZ interface (GDC protective layer) (see Table 3).[122] However, the power density of the model S-SOFC with this material was as low as 215 mW cm^{-2} at 800 °C (see Table 4). The composite material LSTF–CeO_2 infiltrated into the porous SSZ electrolyte layer was used in a reversible fuel cell and demonstrated good performance characteristics (see Table 4) when operating as a SOFC with CO + CO_2 fuel (1 : 1) and as an electrolyzer.[137] The replacement of iron ions by gallium cations, resulting in the composition $La_{0.7}Sr_{0.3}Fe_{0.7}Ga_{0.3}O_{3-\delta}$,[101] led to a decrease in the electrical conductivity to 47.45 S cm^{-1} at 800 °C in air. The material showed low TEC values (13.8×10^{-6} K^{-1}) in air and under reducing atmosphere; the power density of the model S-SOFC with an electrolyte based on LSGM was as high as 489 mW cm^{-2} at 800 °C with wet hydrogen as the fuel (see Tables 2 and 4).

Chromium-substituted ferrite $LaSr_2Fe_2CrO_{9-\delta}$ ($La_{0.33}Sr_{0.67}Fe_{0.67}Cr_{0.33}O_{3-\delta}$), which has been previously studied as the anode material for SOFCs,[138,139] was tested as the electrode material for S-SOFCs.[102] This perovskite has a high electrical conductivity in air, which significantly decreases under reducing atmosphere (see Table 2). The polarization resistance of the $LaSr_2Fe_2CrO_{9-\delta}$/LSGM interface in air and under reducing atmosphere is rather low, and this parameter can be further decreased using an electrode material with GDC (see Table 3). However, the power densities of model S-SOFCs containing the LSGM electrolyte and the LCO protective layer were low (264 mW cm^{-2} at 800 °C, see Table 4). This is probably due to a low electrical conductivity of the material under reducing atmosphere (0.16 S cm^{-1} at 800 °C, see Table 2) and a large thickness of the electrolyte (500 μm) used in S-SOFCs.

Perovskites (R,Ca)(Fe,Mg,Mo)$O_{3-\delta}$, where R = La, Pr and in which iron ions are replaced simultaneously with Mg^{2+} and Mo^{6+} cations, were synthesized and characterized.[103–105] The presence of Mo^{6+} cations in perovskite facilitates an increase in the electrical conductivity and catalytic activity at low partial pressures of oxygen. Actually, the electrical conductivity of such perovskites increases by several times under reducing atmosphere, which is indicative of the change from p-type to n-type conductivity due to the partial reduction of Mo^{6+} cations

to Mo^{5+} and of Fe^{3+} to Fe^{2+}. Thus, the electrical conductivity of $La_{0.3}Ca_{0.7}Fe_{0.6}Mg_{0.175}Mo_{0.225}O_{3-\delta}$ at 900 °C increases from 4.6 to 25 S cm^{-1} in going from air to an $Ar + H_2$ atmosphere (8%).[105] Perovskites (R,Ca)(Fe,Mg,Mo)$O_{3-\delta}$ have reasonable TEC values in air and under reducing atmosphere (see Table 2). It is worth noting that R_η of the electrode material/GDC interface in air for oxide $La_{0.3}Ca_{0.7}Fe_{0.6}Mg_{0.175}Mo_{0.225}O_{3-\delta}$ is rather high (3.6 Ω cm^2 at 900 °C), but it can be reduced to 1.2 Ω cm^2 by the partial replacement of iron ions with cobalt cations according to the formula $La_{0.3}Ca_{0.7}Fe_{0.55}Co_{0.05}Mg_{0.175}Mo_{0.225}O_{3-\delta}$ (see Table 3).

Fan *et al.*[106,123] studied materials based on $SmFeO_3$ doped with ruthenium cations, $Sm_{0.9}Sr_{0.1}Fe_{0.9}Ru_{0.1}O_{3-\delta}$ and $Sm_{0.8}Sr_{0.2}Fe_{0.8}Ti_{0.15}Ru_{0.05}O_{3-\delta}$. The perovskites showed stability at high temperature. It should be noted that no traces of ruthenium metal were detected. Oxide $Sm_{0.8}Sr_{0.2}Fe_{0.8}Ti_{0.15}Ru_{0.05}O_{3-\delta}$ had small TEC ($\sim 11 \times 10^{-6}$ K^{-1}) in air and under reducing atmosphere and a high electrical conductivity (see Table 2). Model S-SOFCs with these materials exhibited a low power density (see Table 4). Meanwhile, the use of A-deficient chemical compositions ($Sm_{0.7}Sr_{0.2}Fe_{0.8}Ti_{0.15}Ru_{0.05}O_{3-\delta}$) made it possible to increase the power density to 417 mW cm^{-2} at 800 °C. The authors attributed this fact to the appearance of ruthenium metal nanoparticles on the surface of the electrode under reducing atmosphere.

The stability of the conventional LSCF cathode material for intermediate-temperature SOFCs under reducing atmosphere can be increased by the partial replacement of iron ions by niobium and molybdenum cations.[107,108] These compounds were tested as electrode materials for S-SOFCs. The synthesized perovskites showed reasonable TEC values both in air and under reducing atmosphere (see Table 2). However, their electrical conductivity at 800 °C in air was lower than 8 S cm^{-1} and it sharply decreased to ~0.5 S cm^{-1} under reducing atmosphere for Nb-substituted compositions. The electrical conductivity of $La_{0.6}Sr_{0.4}Co_{0.2}Fe_{0.7}Mo_{0.1}O_{3-\delta}$ in an Ar + H_2 mixture (5%) was ~3.2 S cm^{-1}, which is associated with a change from p-type to n-type charge carriers.

Model S-SOFCs with $La_{0.6}Sr_{0.4}Co_{0.2}Fe_{0.7}Mo_{0.1}O_{3-\delta}$ showed a higher power density compared to $(La_{0.6}Sr_{0.4})_{0.9}Co_{0.2}Fe_{0.6}Nb_{0.2}O_{3-\delta}$ using hydrogen as the fuel source at 800 °C (737 and 539 mW cm^{-2}, respectively). This is due to a much higher electrical conductivity of Mo-containing perovskites under reducing atmosphere and a smaller polarization resistance of the electrode material/LSGM interface with the SDC protective layer both in air and under reducing atmosphere (see Table 3). It is worth noting that S-SOFCs with the electrode material $La_{0.6}Sr_{0.4}Co_{0.2}Fe_{0.7}Mo_{0.1}O_{3-\delta}$ also exhibited a high power density (800 °C) when ethanol (405 mW cm^{-2}) and LPG (394 mW cm^{-2}) are used as the fuel sources (see Table 4).

Ferrite $PrBaFe_2O_{5+\delta}$ (PBF) with a double perovskite structure was tested as the S-SOFC electrode material (see Fig. 6 *b*). In order to increase the stability of PBF under reducing atmosphere, iron ions were partially replaced by scandium cations according to the formula $PrBa(Fe_{0.8}Sc_{0.2})_2O_{5+\delta}$ (PBFSc).[124] This material showed reasonable electrochemical properties. Thus, the polarization resistance, which was measured using a symmetrical cell with the LSGM electrolyte and PBFSc electrodes at 800 °C, was 0.05 Ω cm^2 in air and 0.18 Ω cm^2 in wet hydrogen. The maximum power density (921 mW cm^{-2}) was achieved using wet hydrogen as the fuel source and air as the oxidant at 850 °C. Besides, the PBFc electrode was quite stable during the cycling of atmosphere at the anode.

Chen *et al.*[109] modified PBF by the partial replacement of iron ions with nickel cations, $PrBaFe_{1.6}Ni_{0.4}O_{5+\delta}$ (PBFN). The PBF and PBFN materials were found to be chemically and thermally compatible with the SDC electrolyte. In this case, PBF as the cathode showed higher activity towards oxygen reduction in air compared to that of the PBFN cathode. Meanwhile, the PBFN anode, unlike PBF, was more active towards hydrogen oxidation (see Table 3). Based on these compositions, a quasisymmetrical PBFN-configured fuel cell (anode)/SDC/PBF (cathode) was created. This fuel cell showed higher power characteristics compared to the symmetrical solid oxide fuel cells PBF/SDC/PBF and PBFN/SDC/PBFN (see Table 4).

Many compounds based on iron-containing perovskites can be assigned to materials for so-called pseudosymmetrical SOFCs. This is associated with the fact that the phase composition of the electrode material in the anode part of the fuel cell changes under reducing atmosphere. The partial oxide reduction on the surface of its particles affords metal and alloy nanoparticles (exsolution; for more details, see the review[140]). The *in situ* synthesized cermets exhibit high electrochemical activity towards fuel oxidation. Meanwhile, many such cermets show reversible oxidation giving a phase with the perovskite structure when changing the reducing for oxidizing atmosphere. Analogous behaviour was observed for perovskites $AFe_{1-x}B_xO_{3-\delta}$, where B = Co, Ni, Cu, Pd. Examples are $LaCo_{0.3}Fe_{0.67}Pd_{0.03}O_{3-\delta}$,[130] $La_{0.5}Sr_{0.5}Fe_{0.8}Cu_{0.2}O_{3-\delta}$,[110] $LaNi_{0.82}Fe_{0.18}O_3$,[125] $La_{0.6}Ca_{0.4}Fe_{0.8}Ni_{0.2}O_{3-\delta}$,[126] $(La,Ce)_{0.7}Sr_{0.3}Fe_{0.9}Ni_{0.1}O_{3-\delta}$,[111] $La_{0.6}Sr_{0.4}Fe_{0.9}Ni_{0.1}O_{3-\delta}$,[131] $PrNi_{0.4}Fe_{0.6}O_{3-\delta}$,[132] $Pr_{0.5}Ba_{0.5}Co_{0.25}Fe_{0.75}O_{3-\delta}$,[112] $Pr_{0.6}Sr_{0.4}(Fe,Mo)_{0.8}Ni_{0.2}O_{3-\delta}$ (see Ref. 113) and $Ba_{0.5}Sr_{0.5}Fe_{0.8}Cu_{0.1}Ti_{0.1}O_{3-\delta}$.[118] The high-temperature electrical conductivity, TEC values and characteristics of S-SOFCs with electrode materials based on these perovskites are given in Tables 2–4.

Among the above-mentioned materials, noteworthy is $La_{0.6}Ce_{0.1}Sr_{0.3}Fe_{0.9}Ni_{0.1}O_{3-\delta}$,[111] which is reduced to form a (Ni,Fe) alloy. The power characteristics of symmetrical solid oxide fuel cells with this electrode material using wet CH_4 as the fuel are among the best (522 mW cm^{-2} at 800 °C) in the series of materials based on substituted $LaFeO_3$. Symmetrical SOFC with CH_4-based fuel and a $PrNi_{0.4}Fe_{0.6}O_{3-\delta}$-based electrode material was characterized by an even higher power density at 800 °C (663 mW cm^{-2}).[132] However, a significant decrease in the power to 105 mW cm^{-2} was observed even at 750 °C, which was attributed to the degradation of the material and carbon deposition on their surface.

A series of studies[114,115,127,133] addressed electrode materials, including composite materials based on oxide $Pr_{0.4}Sr_{0.6}Co_{0.2}Fe_{0.7}Nb_{0.1}O_{3-\delta}$, which is reduced to form the (Co,Fe) alloy,[141] and $(Pr_{0.4}Sr_{0.6})_3(Fe_{0.85}Nb_{0.15})_2O_7$ (Ref. 142) with the structure of the second homologue of the Ruddlesden–Popper series. Besides, materials with chemically similar compositions, in which praseodymium ions are replaced by lanthanum cations, $La_{0.4}Sr_{0.6}Co_{0.2}Fe_{0.7}Nb_{0.1}O_{3-\delta}$, were studied.[116,117,128,129,134] Symmetrical SOFCs based on

these electrode materials showed a high power density, up to 1133 mW cm^{-2} at 900 °C, [133] using hydrogen as the fuel source and pure oxygen as the oxidant (see Table 4). It was mentioned that these S-SOFCs exhibited stable electrochemical performance with prolonged cycling of atmosphere at the anode.

Therefore, an analysis of the recent literature data shows that iron-containing perovskites have attracted great attention. However, perovskites containing exclusively iron cations in the B-site have limited stability under reducing atmosphere. One of the main approaches to improving single-phase materials based on such perovskites is the partial replacement of iron ions by cations with stable oxidation states under anode gas conditions, such as Mg^{2+}, Sc^{3+}, Nb^{5+} (see ‡).

These materials combine high stability under reducing atmosphere with reasonable electrical conductivity and TEC and also exhibit high electrochemical activity towards electrode reactions. Perovskites $(R,Ca)(Fe,Mg,Mo)O_{3-\delta}$, where R = La, Pr, containing molybdenum cations in the B-site also deserve notice. The electrical conductivity of these perovskites increases by several times under reducing atmosphere due to a change from p-type to n-type conductivity. Studies of materials for pseudosymmetrical SOFCs based on iron-containing perovskites involving cobalt, nickel, copper and palladium cations are also of interest. Cermets synthesized *in situ* based on these materials at the anode of SOFCs exhibit high electrochemical activity towards fuel oxidation.

‡ The Al^{3+} cation can be assigned to these cations; however, to the best of our knowledge, there are no studies on aluminium-substituted ferrites as electrode materials for S-SOFCs.

6.2. Electrode materials based on double perovskites $A_2(B,Mo)_2O_{6-\delta}$, where A = Sr; B = Fe, Co

In this Section, we discuss practical applications of materials based on double perovskites $A_2(B,Mo)_2O_{6-\delta}$, where A = Sr; B = Fe, Co, their derivatives with different substitution patterns of A and B cations, and composite electrodes based on these perovskites. The analysis is restricted to the publications in which these materials are considered as S-SOFC electrodes. It is worth noting that in most studies, these materials were investigated as either potential anodes (predominantly) or SOFC cathodes.

6.2.1. Single-phase oxide electrode materials

Among single-phase oxide compounds, materials based on $Sr_2Fe_{1.5}Mo_{0.5}O_{6-\delta}$ (SFM) have the highest potential for use as S-SOFC electrodes. In the crystal structures of these compounds, B-site cations can be ordered to form a double perovskite structure (see Fig. 5). These phases exhibit high stability during redox cycling due to a flexible change of the oxidation state and the coordination environment of iron cations.[143–145] Besides, it was noted [146] that the electronic structure of $Sr_2FeMoO_{6-\delta}$ is characterized by the formation of a common energy band derived simultaneously from the electronic states of iron and molybdenum. In the authors' opinion, this made it impossible to reduce all Fe^{3+} cations to Fe^{2+} in double perovskite, thereby providing high stability of this phase under reducing atmosphere.

There are contradictory literature data on stability of SFM under hydrogen atmosphere. For instance, it was reported [143] that SFM is stable during annealing in hydrogen at 1400 °C for 24 h. However, later it was shown that traces of iron metal appeared upon the thermal treatment of this oxide in hydrogen at a much lower temperature. For example, it was found [147] that SFM is already reduced

Table 5. Electrical conductivities and TECs of electrode materials based on double perovskites $Sr_2(B,Mo)_2O_{6-\delta}$, where B = Fe, Co, under oxidizing and reducing atmosphere.

Composition	*T*, °C	Atmosphere	σ, S cm^{-1}	Thermal expansion		Ref.
				temperature range, °C	TEC × 10^6, K^{-1} (in air)	
$Sr_2Fe_{1.5}Mo_{0.5}O_{6-\delta}$	780	Air	550	200–760	14.5	143, 144
	780	H_2	310	760–1200	21.4	143, 144
				200–1200	18.1	143, 144
	600	Air	17.6	—	—	148
	600	Wet H_2	11.1	—	—	148
$Sr_2Co_{1.1}Mo_{0.9}O_{6-\delta}$	850	Air	1.13	See [a]	See [a]	149
	850	H_2	7.83	See [a]	See [a]	149
$Sr_2Co_{1.15}Mo_{0.85}O_{6-\delta}$	850	Air	3.75	See [a]	See [a]	149
	850	H_2	8.52	See [a]	See [a]	149
$Sr_2Co_{1.2}Mo_{0.8}O_{6-\delta}$	850	Air	5.12	See [a]	See [a]	149
	850	H_2	4.16	See [a]	See [a]	149
$Sr_2Fe_{1.5-x}Co_xMo_{0.5}O_{6-\delta}$	750	Air	38.4 (x = 0)	—	—	150
	750	Air	54 (x = 0.5)	—	—	150
	800	Air	59.5 (x = 0.75)	—	—	150
	800	Air	52 (x = 1)	—	—	150
$Sr_2Fe_{1.4}Nb_{0.1}Mo_{0.5}O_{6-\delta}$	600	Air	27.6	—	—	148
		Wet H_2	15.9	—	—	148
$Sr_2Fe_{1.5}Mo_{0.5}O_{6-\delta}$–SDC	800	Air	10	—	—	151
(90 : 10 mass %)	800	Wet H_2	15	—	—	151

[a] For certain compositions considered by Wei *et al.*,[149] the TEC values were not reported, and it was only mentioned that these values, measured in the temperature range of 30–900 °C, are in the range of $(6–15) \times 10^{-6}$ K^{-1}.

at 800 °C (10 h) in wet hydrogen. Apparently, stability of SFM under reducing atmosphere has a kinetic nature and depends, in particular, on the size of its particles.

Materials based on SFM have high electrical conductivity under both oxidizing and reducing atmosphere (Table 5) and also change the type of electron-hole conductivity during redox cycling.[143] These materials also exhibited high electrocatalytic activity in oxygen reduction and H_2/CH_4 oxidation. The use of the material $Sr_2Fe_{1.5}Mo_{0.5}O_{6-\delta}$ as a promising electrode for S-SOFCs was first reported by Liu *et el.*[143] In the temperature range of 200 – 1200 °C, the average TEC value in air is 18.1×10^{-6} K^{-1} (see Table 5),[144] which is smaller than that for cobaltite-based cathode materials [*e.g.*, 20.5×10^{-6} K^{-1} for $La_{0.6}Sr_{0.4}CoO_{3-\delta}$ (Ref. 152)]. However, at temperatures of 200 – 760 °C, the thermal expansion coefficient of SFM decreases to 14.5×0^{6} K^{-1}, resulting in much smaller mismatch with TEC of the electrolyte during operation of the fuel cell in this temperature range.

A study of chemical compatibility of SFM with materials for solid electrolytes based on YSZ, LSGM, SDC and $BaZr_{0.1}Ce_{0.7}Y_{0.2}O_{3-\delta}$ (BZCY) during annealing at 1400 °C for 24 h in air demonstrated that secondary phases were absent in all cases, except YSZ. When using YSZ-based electrolytes, secondary phases with SFM formed after the thermal treatment at 1000 °C for 24 h in air. Taking into account a rather high conductivity of SFM at moderate temperatures (700 °C), LSGM was used as a solid electrolyte membrane to evaluate the polarization characteristics of the SFM electrode and performance characteristics of S-SOFCs with SFM-based electrodes. The polarization resistances of SFM electrodes in air and under wet hydrogen atmosphere (3% H_2O) are given in Table 6. In air, the R_η value of SFM is comparable with that of the composite cathode $(La_{0.8}Sr_{0.2})_{0.9}MnO_3 - YSZ$, whereas under wet hydrogen atmosphere, the R_η values are comparable with that of the conventional Ni – YSZ cermet anode.[157] The power densities of the electrolyte-supported symmetrical fuel cell with the SFM/LSGM/SFM configuration are given in Table 7. This fuel cell showed a power density of 835 and 230 mW cm^{-2} with humidified hydrogen and methane, respectively, as the fuel at 900 °C.[143] It should be noted that at a higher concentration of oxygen vacancies in the structure (according to the X-ray photoelectron spectroscopy, the oxygen content in the lattice varies from 5 to 5.75),[143] oxygen ion conductivity appears, thereby providing high electrochemical performance of S-SOFC electrodes.

The discovery of highly efficient SFM-based material has caused an interest in other double perovskites. Wei *et al.*[149] studied a series of new electrode materials for S-SOFCs based on nonstoichiometric double perovskites of the composition $Sr_2Co_{1+x}Mo_{1-x}O_{6-\delta}$ (SCM, $x = 0.1$, 0.15, 0.2). The electrical conductivity study demonstrated that, unlike SFM, the electrical conductivity of SCM under oxidizing and reducing conditions is at most 9 S cm^{-1} in the temperature range of 300 – 850 °C (see Table 5). The thermal expansion coefficients of SCM samples are in good agreement with TECs of solid electrolytes based on YSZ and LSGM (see Table 5). The TEC values vary from 6×10^{-6} to 15×10^{-6} K^{-1} in the temperature range from ambient temperature to 900 °C. These TEC values are smaller than those of conventional cobalt-containing perovskites, which are characterized by large TECs due to thermally induced transitions between low- and high-spin states of the Co^{3+} cation.[160]

Table 6. Polarization resistances of electrode materials based on double perovskites $Sr_2(B,Mo)_2O_{6-\delta}$, where B = Fe, Co, under oxidizing and reducing atmosphere.

Composition of the material	T, °C	Atmosphere	R_η, Ω cm^2	Ref.
$Sr_2Fe_{1.5}Mo_{0.5}O_{6-\delta}$	750	Air	0.66	143
	800	Air	0.24	143
	850	Air	0.10	143
	750	Wet H_2	0.46	143
	800	Wet H_2	0.27	143
	850	Wet H_2	0.21	143
	650	Air	0.90	148
	700	Air	0.45	148
	750	Air	0.24	148
	800	Air	0.13	148
	650	Wet Ar + H_2 (5%)	10.2	148
	700	Wet Ar + H_2 (5%)	5.4	148
	750	Wet Ar + H_2 (5%)	2.8	148
	800	Wet Ar + H_2 (5%)	1.9	148
$Sr_2Co_{1.1}Mo_{0.9}O_{6-\delta}$	800	Air	0.18	149
	800	H_2	0.35	149
$Sr_2Co_{1.15}Mo_{0.85}O_{6-\delta}$	800	Air	0.15	149
	800	H_2	0.45	149
$Sr_2Co_{1.2}Mo_{0.8}O_{6-\delta}$	800	Air	0.14	149
	800	H_2	0.69	149
$Sr_2Fe_{1.4}Nb_{0.1}Mo_{0.5}O_{6-\delta}$	650	Air	0.96	148
	700	Air	0.31	148
	750	Air	0.15	148
	800	Air	0.10	148
	650	Wet Ar + H_2 (5%)	6.2	148
	700	Wet Ar + H_2 (5%)	3.4	148
	750	Wet Ar + H_2 (5%)	2.1	148
	800	Wet Ar + H_2 (5%)	1.5	148
$Sr_2Fe_{1.5}Mo_{0.5}O_{6-\delta}$ – SDC	800	Air	0.26	151
(90 : 10 mass %)	800	Wet H_2	0.12	151
$Sr_2Fe_{1.5}Mo_{0.5}O_{6-\delta}$ – SDC	800	Air	0.06	153
(90 : 10 mass %) [a]				
$Sr_2Fe_{1.5}Mo_{0.5}O_{6-\delta}$ (see [b])	650	Air	0.13	154
	650	Wet H_2	0.62	154
	800	Air	0.04	154
	800	Wet H_2	0.22	154
$Sr_2Fe_{1.5}Mo_{0.5}O_{6-\delta}$ (see [c])	650	Air	0.16	155
	650	Wet H_2	0.45	155
	800	Air	0.05	155
	800	Wet H_2	0.09	155
$Sr_2Fe_{1.5}Mo_{0.5}O_{6-\delta}$ (see [d])	750	Air	0.064	156

[a] The electrode impregnated with Pr_6O_{11}. [b] The infiltration of the electrode material into the porous LSGM layer prepared by the film casting technique. [c] The infiltration of the electrode material into the porous LSGM layer prepared by the phase inversion technique. [d] The infiltration of the electrode material into the porous YSZ electrolyte layer.

The evaluation of the performance characteristics of S-SOFCs with SCM-based electrodes and LSGM solid electrolyte showed that the maximum power density of 460 mW cm^{-2} at 800 °C was achieved for the composition with $x = 0.15$. Rather low polarization resistances of SCM electrodes (see Table 6) together with high power density characteristics (see Table 7), despite rather low electrical

Table 7. Power densities of S-SOFCs with the LSGM solid electrolyte and electrode materials based on double perovskites $Sr_2(B,Mo)_2O_{6-\delta}$, where B = Fe, Co.

Composition of the material	Current collector	Fuel	T, °C	P_{max}, mW cm^{-2}	L_e, μm	Ref.
$Sr_2Fe_{1.5}Mo_{0.5}O_{6-\delta}$	Au	Wet H_2	900	835	265	143
	Au	Wet CH_4	900	230	265	143
	–	Wet H_2	650	92	236	148
	–	Wet H_2	700	156	236	148
	–	Wet H_2	750	228	236	148
	–	Wet H_2	800	374	236	148
$Sr_2Co_{1.15}Mo_{0.85}O_{6-\delta}$	Ag	H_2	800	460	300	149
$Sr_2Fe_{1.5}Mo_{0.5}O_{6-\delta}$	–	0.5% H_2S + 3% H_2	800	27.3	200	150
$Sr_2FeCo_{0.5}Mo_{0.5}O_{6-\delta}$	–	0.5% H_2S + 3% H_2	800	42.6	200	150
	–	0.05% H_2S + N_2	600	17.6	200	158
	–	0.05% H_2S + N_2	650	25.0	200	158
	–	0.05% H_2S + N_2	700	31.8	200	158
	–	0.05% H_2S + N_2	750	36.9	200	158
	–	0.05% H_2S + N_2	800	45.7	200	158
$Sr_2Fe_{1.4}Nb_{0.1}Mo_{0.5}O_{6-\delta}$	–	Wet H_2	650	124	243	148
	–	Wet H_2	700	244	243	148
	–	Wet H_2	750	365	143	148
	–	Wet H_2	800	532	243	148
$Sr_2Fe_{1.5}Mo_{0.5}O_{6-\delta}$ – SDC (90 : 10 mass %)	Pt	Wet H_2	800	500	300	151
$Sr_2Fe_{1.5}Mo_{0.5}O_{6-\delta}$ – SDC (90 : 10 mass %) [a]	Pt	Wet H_2	700	250	760	153
	Pt	Wet H_2	800	500	760	153
	Pt	CH_4	700	100	760	153
	Pt	CH_4	800	250	760	153
$Sr_2Fe_{1.5}Mo_{0.5}O_{6-\delta}$ – GDC (70 : 30 mass %) [a]	–	Wet H_2	650	60	300	159
	–	Wet H_2	700	191	300	159
	–	Wet H_2	750	113	300	159
$Sr_2Fe_{1.5}Mo_{0.5}O_6$ (see [b])	–	Wet H_2	650	390	15	154
	–	Wet H_2	700	600	15	154
	–	Wet H_2	750	850	15	154
	–	Wet H_2	800	970	15	154
	–	N_2 + C_8H_{18} (6%)	800	390	15	154
$Sr_2Fe_{1.5}Mo_{0.5}O_6$ (see [c])	Ag	Wet H_2	650	401	25	155
	Ag	Wet H_2	700	521	25	155
	Ag	Wet H_2	750	602	25	155
	Ag	Wet H_2	800	703	25	155
$Sr_2Fe_{1.5}Mo_{0.5}O_6$ (see [d])	Au	CO + CO_2 (1 : 1)	750	265	–	156

[a] The impregnation of Pr_6O_{11} into the cathode, the impregnation of Ni into the anode. [b] The infiltration of the electrode material into the porous LSGM layer prepared by the film casting technique. [c] The infiltration of the electrode material into the porous LSGM layer prepared by the phase inversion technique. [d] The infiltration of the electrode material into the porous YSZ electrolyte layer.

conductivity (see Table 5), are attributed to the presence of oxygen vacancies in the structure, which are responsible for reasonable oxygen-ion conductivity of the material.

Song *et al.*[150] considered a series of compositions $Sr_2Fe_{1.5-x}Co_xMo_{0.5}O_{6-\delta}$ with the partial replacement of iron ions with cobalt cations in SFM (SFCM, x = 0, 0.5, 0.75, 1). According to photoluminescence spectroscopy, an increase in the cobalt content from x = 0 to x = 0.75 in SFCM leads to an increase in the concentration of oxygen vacancies (δ) from 0.29 to 0.46. The evaluation of redox activity of SFCM in oxygen reduction and hydrogen oxidation by temperature-programmed desorption of oxygen and temperature-programmed reduction, respectively, demonstrated that the composition with x = 0.75 has the highest catalytic activity. Meanwhile, the partial replacement of iron ions by cobalt cations in SFM affects not only the catalytic activity but also the electronic and ionic conductivity. The electrical conductivity of cobalt-substituted materials is much higher than that of undoped SFM (see Table 5). It is interesting that the conductivity of the starting SFM[150] is more than an order of magnitude smaller than the values published earlier for the same composition.[143] Song *et al.*[150] did not comment on this discrepancy. Electrode materials for SFCMs (x = 0.5) were tested in electrolyte-supported S-SOFC using 200 μm-thick LSGM as a solid electrolyte membrane. In the case of SFCM electrodes, the maximum power density of the fuel cell fed with a 0.5% H_2S + 3% H_2 mixture was 42.6 mW cm^{-2} at 800 °C, which is 1.5 times higher compared to the corresponding characteristics of a fuel cell with SFM electrodes (27.3 mW cm^{-2}) under the same experimental conditions.[150] However, the performance characteristics of the fuel cell with SFM electrode fed with wet hydrogen were not evaluated,[150] which hinders the comparison of these results with those reported previously.[143]

The partial replacement of iron ions by cobalt cations in SFM contributes to an increase in tolerance of material

for H_2S impurities in the fuel gas. In this case, cobalt acts as a kind of an adsorbent of sulfur due to high affinity for formation of sulfide at high temperatures.[161,162] According to the X-ray powder diffraction and energy-dispersive X-ray spectroscopy, the formation of metal sulfides, particularly CoS, plays a key role in the increase in the rate of catalytic oxidation of H_2S in SOFC.[163]

As mentioned above, the main approach to increase the stability of iron-containing perovskites under reducing atmosphere is based on the partial replacement of iron ions by cations with stable oxidation states under reducing atmosphere. Hence, it can be suggested that the phase stability and electrocatalytic activity of SFM can be controlled by choosing an appropriate dopant, which will improve characteristics of the symmetrical electrode. Niobium was considered as a dopant for the partial replacement of iron ions in order to increase the stability and catalytic activity of the starting SFM electrode material.[148] In this study, the electrode material $Sr_2Fe_{1.4}Nb_{0.1}Mo_{0.5}O_{6-\delta}$ (SFNbM) was synthesized and prospects of its application in S-SOFCs were evaluated.

This material showed higher stability under reducing atmosphere compared to the staring SFM. Besides, as compared to SFM, the electrical conductivity of SFNbM increases from 17.6 to 27.6 S cm^{-1} in air and from 11.1 to 15.9 S cm^{-1} in wet hydrogen at 600 °C. In relation to electrochemical activity, SFNbM electrode material shows lower polarization resistance compared to SFM both under oxidizing and reducing atmosphere (see Table 6). A similar tendency is evident from a comparison of the performance characteristics of S-SOFCs with these electrode materials (see Table 7). The use of SFNbM enhances the electrochemical performance of fuel cells due to smaller polarization losses both under oxidizing and reducing atmosphere. Therefore, the partial replacement of iron ions by niobium cations in SFM enhances the phase stability under reducing atmosphere and the electrochemical performance of electrode material for S-SOFCs.

6.2.2. Composite SFM-based electrode materials

Materials prepared by mechanical mixing of components. The prospects of the creation of a promising composite electrode material SDC–$Sr_2Fe_{1.5}Mo_{0.5}O_{6-\delta}$ for S-SOFCs were considered by Osinkin *et al.*[151] The electrical conductivity of this composite at 800 °C was ~10 and 15 S cm^{-1} in air and under wet hydrogen atmosphere, respectively (see Table 5). A typical thermally activated behaviour was observed under reducing atmosphere. Thus, the electrical conductivity increases with increasing temperature due apparently to an increase in the contribution of electronic conductivity through the partial reduction of Ce^{4+} to Ce^{3+} and of Mo^{6+} to Mo^{5+}. The polarization resistance of electrodes in contact with LSGM electrolyte in air and in wet hydrogen atmosphere was 0.26 and 0.12 Ω cm^2, respectively (see Table 6).

It is worth noting that SFM–SDC electrodes, although having rather low electrical conductivity, exhibit reasonable activity and can compete with conventional electrode materials. The maximum power density estimated for S-SOFCs supported on 300 μm-thick LSGM electrolyte was ~500 mW cm^{-2} at 800 °C with air supplied to the cathode and wet hydrogen supplied to the anode (see Table 7). An analysis of polarization losses demonstrated that the polarization of the oxygen electrode, which is much higher than that of the anode, is the limiting factor. In a continuation of this study, the SFM–SDC composite electrode was modified by impregnation with an electrocatalytically active Pr_6O_{11} additive in order to improve the kinetics of oxygen electroreduction at the cathode.[153] This led to a significant decrease in the polarization resistance of the electrode in air from 0.26 to 0.06 Ω cm^2 at 800 °C (see Table 6). The voltage–current study of S-SOFCs with supporting LSGM electrolyte and SFM–SDC electrodes, which were modified by impregnation with praseodymium nitrate (impregnation of Pr_6O_{11} into the cathode layer) and nickel nitrate (impregnation of Ni into the anode layer) in the absence of buffer and current layers, showed that these fuel cells fed with wet hydrogen and methane have good power densities of 500 and 250 mW cm^{-2}, respectively, at 800 °C (see Table 7).

Another example of the application of a composite based on SFM–GDC as the S-SOFC electrode was reported by Guo *et al.*[159] The electrochemical performance study of YSZ electrolyte-supported S-SOFCs with GDC buffer layers and SFM–GDC electrodes demonstrated that these S-SOFCs have acceptable power density characteristics (see Table 7) despite the use of YSZ electrolyte, which has lower oxygen ion conductivity compared to LSGM. It was also mentioned that, due to excellent electrochemical performance, SFM–GDC symmetrical electrodes can be used in YSZ electrolyte-supported reversible SOFCs with GDC buffer layers.

Materials based on SFM prepared by infiltrations methods. Meng *et al.*[154] described the application of the SFM–LSGM composite, which was prepared by the impregnation of SFM into the porous LSGM skeleton, as electrode material for S-SOFCs. The authors produced three-layer LSGM-based ceramic structures composed of a 15 μm-thick dense layer of this oxide sandwiched between two porous 150 μm-thick layers. Porous LSGM layers were prepared by the film casting technique and impregnated with a solution containing strontium, iron and molybdenum cations in amounts corresponding to the SFM composition. In air, the infiltrate consisted predominantly of the SFM phase with a small portion of $SrMoO_4$; under hydrogen atmosphere, of the phase $SrFe_{0.675}Mo_{0.325}O_{3-\delta}$ with a minor portion of iron metal.[164,165] The anode and cathode polarization resistances under wet hydrogen and in air were 0.22 and 0.04 Ω cm^2, respectively, at 800 °C (see Table 6).

An analysis of the impedance data for symmetrical fuel cells depending on the partial pressure of hydrogen and the temperature showed that the hydrogen adsorption on the SFM electrocatalyst surface and the charge transfer across the SFM/LSGM interface were the rate-limiting steps for hydrogen oxidation reactions on SFM–LSGM composite electrodes prepared by infiltration of SFM at high (800 °C) and moderate (600 °C) temperatures, respectively. The power densities of S-SOFC with such electrodes are reasonably high (see Table 7). The power density using hydrogen as the fuel was 390 mW cm^{-2} at 650 °C and 970 mW cm^{-2} at 800 °C. It should be noted that the fuel cell with the maximum power density of 390 mW cm^{-2} at 800 °C showed stable power output with a C_8H_{18} (6%) + N_2 (94%) mixture as the fuel. This is evidence of good carbon tolerance of the SFM–LSGM composite electrode.

In a continuation of this study, Gao *et al.*[155] investigated S-SOFC, which had a similar composition but

differed in that porous LSGM layers for subsequent infiltration of SFM were prepared by the phase inversion method. As opposed to the film casting technique for the preparation of porous layers giving rise to a fine porous structure with a random pore distribution, the phase inversion method afforded a structure with larger columnar pores oriented along the normal to the electrolyte surface. The anode and cathode polarization resistances of the electrode under hydrogen atmosphere and in air are comparable with the corresponding values obtained earlier [157] (see Table 6). The performance study of S-SOFCs fed with wet hydrogen demonstrated good power densities (703, 602, 521 and 401 mW cm^{-2} at 800, 750, 700 and 650 °C, respectively; see Table 7). A somewhat lower electrochemical performance compared to that achieved earlier was accounted [154] for by the following factors:

— a decrease in open circuit voltage due to the formation of point microdefects that disturb the gas tightness of the thin-film layer of the electrolyte;

— an increase in the gas diffusion resistance at applied current due to a high content of the SFM electrocatalyst in the porous LSGM structure.

The possibility of producing composite electrodes for S-SOFCs by the infiltration of SFM was also considered by Li *et al.*[156] A three-layer support was composed of dense YSZ film electrolyte sandwiched between two porous YSZ layers. The authors investigated the influence of the infiltration of SFM into the porous YSZ scaffold on the polarization resistance of the composite electrode in air and found that the highest electrochemical performance of the electrode in oxygen reduction was achieved by the infiltration of 11.7 mass % SFM; R_η was 0.064 Ω cm^2 at 750 °C in air (see Table 6). A symmetrical solid oxide fuel cell with such electrodes showed the maximum power density of 265 mW cm^{-2} at 750 °C using a mixture of CO and CO_2 in a 1 : 1 ratio as the fuel (see Table 7). It is worth noting that S-SOFCs with SFM – YSZ electrodes prepared by the infiltration also exhibited high performance and cycling stability during reversible operation of SOFCs.

Therefore, the use of infiltration methods for the introduction of electroactive phases is a promising approach to create high-performance S-SOFC electrodes based on double perovskites $Sr_2(B,Mo)_2O_{6-\delta}$, where B = Fe, Co. These methods provide a decrease in R_η of the electrode and an increase in the power density of the fuel cell. However, the maintenance of high electrochemical characteristics of S-SOFCs under long-term operation and cycling of atmosphere at the anode remains a challenging problem.

6.3. Electrode materials based on chromium- and manganese-containing perovskites

Back in 2006, Bastidas *et al.*[166] reported that material based on $La_{0.75}Sr_{0.25}Cr_{0.5}Mn_{0.5}O_3$ (LSCM) can be used as electrode material for S-SOFCs. However, the total conductivity of LSCM in air and particularly under reducing conditions is rather low. Song *et al.*[167] found that the partial replacement of Sr^{2+} ions by Ce^{3+} cations in LSCM according to the formula $La_{0.75}Sr_{0.125}Ce_{0.125}Cr_{0.5}Mn_{0.5}O_{3-\delta}$ (LSCCM) leads to an increase in the total electrical conductivity in air and in wet hydrogen. Thus, the electrical conductivity at 900 °C in air increased from 14.6 S cm^{-1} for LSCM to 20.95 S cm^{-1} for LSCCM; in wet hydrogen, from 0.95 to 1.66 S cm^{-1} (see Table 8). However, model electrolyte-supported S-SOFC with LSCCM electrode material did not show improved performance characteristics compared to analogous S-SOFC with LSCM electrode material.[167]

Luo *et al.*[173] made an attempt to adapt the commercially available cathode material $La_{0.8}Sr_{0.2}MnO_{3-\delta}$ (LSM) to use it in S-SOFCs. However, it is well-known that LSM serves as material for high-temperature SOFC, and its efficiency decreases with decreasing operating temperature because of low oxygen ion conductivity and a rapid decrease in the electrocatalytic activity. This issue can be partially addressed using composite electrode material containing, apart from LSM, oxide with high oxygen ion conductivity (*e.g.*, SOFC electrolyte). This composite, LSM – GDC, was tested as electrode material for intermediate-temperature S-SOFC with YSZ electrolyte; however, the polarization resistance of the electrode/electrolyte interface under oxidizing and reducing atmos-

Table 8. Electrical conductivities of electrode materials based on chromium- and manganese-containing perovskites under oxidizing and reducing atmosphere.

Composition of the material	*T*, °C	Atmosphere	σ, S cm^{-1}	Ref.
$La_{0.75}Sr_{0.125}Ce_{0.125}Cr_{0.5}Mn_{0.5}O_{3-\delta}$	900	Air	20.95	167
	900	Wet H_2	1.66	167
$La_{0.75}Sr_{0.25}Cr_{0.5}Mn_{0.5}O_{3-\delta}$	900	Air	14.6	167
	900	Wet H_2	0.95	167
$(La_{0.8}Sr_{0.2})_{0.9}Sc_{0.2}Mn_{0.8}O_{3-\delta}$	850	Air	37.1	168
	850	N_2 + H_2 (5%)	5.7	168
$(La_{0.8}Sr_{0.2})_{0.9}Sc_{0.2}Mn_{0.75}Ru_{0.05}O_{3-\delta}$	850	Air	53	168
	850	N_2 + H_2 (5%)	9.3	168
$PrBaMn_2O_{5+\delta}$	800	Air	91.5	169
	800	Ar + H_2 (5%)	8.16	169
	800	Ar + H_2 (5%)	1.25	170
$PrBa_{0.8}Ca_{0.2}Mn_2O_{5+\delta}$	800	Air	13.4	171
	800	Ar + H_2 (5%)	5.48	171
$SmBaMn_2O_{5+\delta}$	900	Air	58.1	172
	900	Ar + H_2 (5%)	10.7	172
$PrBaMn_{1.5}Fe_{0.5}O_{5+\delta}$	800	Air	112.5	170
	800	Ar + H_2 (5%)	7.4	170

Table 9. Polarization resistances of electrode materials based on chromium- and manganese-containing perovskites under oxidizing and reducing atmosphere.

Composition of the material	Electrolyte	T, °C	Atmosphere	R_η, Ω cm^2	Ref.
$La_{0.8}Sr_{0.2}MnO_{3-\delta}$ – GDC (70 : 30 mass %)	YSZ	800	Air	1.44	173
	YSZ	800	Wet H_2	5.19	173
	YSZ	650	Air	8.62	173
	YSZ	650	Wet H_2	45.87	173
$La_{0.8}Sr_{0.2}MnO_{3-\delta}$	YSZ	800	Air	3.03	173
	YSZ	800	Wet H_2	10.49	173
	YSZ	650	Air	59.68	173
	YSZ	650	Wet H_2	112.23	173
$(La_{0.8}Sr_{0.2})_{0.9}Sc_{0.2}Mn_{0.75}Ru_{0.05}O_{3-\delta}$	SSZ	800	Air	0.23	168
	SSZ	800	N_2 + H_2 (5%)	0.52	168
$(La_{0.8}Sr_{0.2})_{0.9}Sc_{0.2}Mn_{0.8}O_{3-\delta}$	SSZ	800	Air	0.58	168
	SSZ	800	N_2 + H_2 (5%)	3.5	168
$PrBaMn_2O_{5+\delta}$	LSGM	800	Air	0.30	170
	LSGM	800	Wet H_2	0.78	170
$PrBaMn_2O_{5+\delta}$ – Pr_6O_{11}	YSZ	800	Air	0.016	174
	YSZ	800	Wet H_2	0.20	174
$SmBaMn_2O_{5+\delta}$	LSGM	900	Air	0.066	172
	LSGM	900	Wet H_2	0.314	172
	LSGM	800	Air	0.269	172
	LSGM	800	Wet H_2	1.226	172
$PrBaMn_{1.5}Fe_{0.5}O_{5+\delta}$	LSGM	800	Air	0.22	170
	LSGM	800	Wet H_2	0.68	170

Table 10. Power densities of S-SOFCs with electrode materials based on chromium- and manganese-containing perovskites.

Composition of the material	Electrolyte	Current collector	Fuel	T, °C	P_{max}, mW cm^{-2}	L_e, μm	Ref.
$La_{0.75}Sr_{0.125}Ce_{0.125}Cr_{0.5}Mn_{0.5}O_{3-\delta}$	YSZ	–	Wet H_2 (1% H_2S)	900	33.12	600	167
	YSZ	–	3% H_2 (1% H_2S)	900	20.05	600	167
	YSZ	–	3% H_2	900	52.1	600	167
	YSZ	–	Wet H_2	900	76.5	600	167
$La_{0.75}Sr_{0.25}Cr_{0.5}Mn_{0.5}O_{3-\delta}$	YSZ	–	Wet H_2 (1% H_2S)	900	23.47	–	167
	YSZ	–	3% H_2 (1% H_2S)	900	29.96	–	167
$La_{0.8}Sr_{0.2}MnO_{3-\delta}$ – GDC (70 : 30 mass %)	YSZ	Ag	Wet H_2	800	150.8	–	173
$La_{0.8}Sr_{0.2}MnO_{3-\delta}$	YSZ	Ag	Wet H_2	800	67.45	–	173
$(La_{0.8}Sr_{0.2})_{0.9}Sc_{0.2}Mn_{0.75}Ru_{0.05}O_{3-\delta}$	SSZ	Ag	Wet H_2	800	318	–	168
$PrBa_{0.8}Ca_{0.2}Mn_2O_{5+\delta}$ (see [a])	LSGM/LCO [b]	Ag	Wet H_2	800	1101	250	171
	LSGM/LCO [b]	Ag	Wet H_2	750	768	250	171
	LSGM/LCO [b]	Ag	Wet H_2	700	502	250	171
	LSGM/LCO [b]	Ag	Wet C_3H_8	800	740	250	171
	LSGM/LCO [b]	Ag	C_8H_{18}	800	470	250	171
$PrBaMn_2O_{5+\delta}$ – Pr_6O_{11} (see [c])	YSZ/GDC [b]	Ag	Wet H_2	800	423	–	174
	YSZ/GDC [b]	Ag	CH_4	800	227	–	174
$SmBaMn_2O_{5+\delta}$	LSGM/LCO [b]	Ag	Wet H_2	900	782	300	172
	LSGM/LCO [b]	Ag	Wet H_2	800	481	300	172
	LSGM/LCO [b]	Ag	Wet H_2	750	314	300	172
$PrBaMn_{1.5}Fe_{0.5}O_{5+\delta}$	LSGM	Pt	Wet H_2	800	540	520	170
	LSGM	Pt	CH_4	700	230	520	170

[a] The electrode layer impregnated with a solution of cobalt and iron nitrates (1 : 1). [b] The LCO or GDC protective layer. [c] The infiltration with a praseodymium nitrate solution.

phere is not encouraging (Table 9). The maximum power density was also low (Table 10).

Zheng *et al.*[175] demonstrated that the partial replacement of manganese ions by scandium cations in LSM according to the formula $La_{0.8}Sr_{0.2}Sc_{0.2}Mn_{0.8}O_{3-\delta}$ (LSSM) made it possible to prepare promising material for S-SOFCs showing high electrical conductivity and stability under reducing atmosphere. However, the power density of S-SOFC was as low as 220 mW cm^{-2} at 800 °C using wet hydrogen as the fuel. Therefore, this material

had to be improved. For this purpose, Zhou *et al.*[168] modified the chemical composition of LSSM and prepared A-deficient perovskites $(La_{0.8}Sr_{0.2})_{0.9}Sc_{0.2}Mn_{0.8}O_{3-\delta}$ (L72S18SM) and $(La_{0.8}Sr_{0.2})_{0.9}Sc_{0.2}Mn_{0.75}Ru_{0.05}O_{3-\delta}$ (L72S18SMR). At 850 °C, the maximum conductivity of L72S18SM in air and under $N_2 + H_2$ (5%) atmosphere was 37.1 and 5.7 S cm^{-1}, respectively (see Table 8). These values are larger than those for stoichiometric LSSM.[175] At 850°C, oxide L72S18SMR showed an even higher electrical conductivity both in air (53 S cm^{-1}) and under $N_2 + H_2$ (5%) atmosphere (9.3 S cm^{-1}) (see Table 8). The electrochemical characterization of L72S18SMR as the cathode demonstrated $R_\eta = 0.23$ Ω cm^2 at 800 °C, and this value is several times smaller than R_η for L72S18SM (0.58 Ω cm^2). Meanwhile, L72S18SMR at 800 °C exhibited high electrochemical activity under reducing atmosphere ($R_\eta = 0.52$ Ω cm^2), whereas $R_\eta = 3.5$ Ω cm^2 for L72S18SM (see Table 9). Apart from the improvement of electronic conductivity, this may be attributed mainly to significant changes in the morphology of the electrode surface. Ruthenium nanoparticles that emerge on the surface of L72S18SMR during heating under reducing atmosphere (exsolution) serve as a catalyst booster and significantly improve electrochemical performance of the electrode in hydrogen oxidation. The maximum power density of S-SOFC with SSZ electrolyte was 318 mW cm^{-2} at 800 °C (see Table 10).

Materials based on double perovskite $RBaMn_2O_{5+\delta}$, where R is a rare-earth element; $0 < \delta < 1$, with a layered structure (see Fig. 6 *b*) are currently attracting great interest because such oxides, unlike manganites $(La,Sr)MnO_{3-\delta}$, are characterized by easier oxygen exchange kinetics, which can be evaluated from such parameters as the surface exchange coefficient (k) and the bulk diffusion coefficient (D^*). Choi *et al.*[171] showed that the coefficients D^* and k for $PrBaMn_2O_{5+\delta}$ and $PrBa_{0.8}Ca_{0.2}Mn_2O_{5+\delta}$ are several orders of magnitude larger than those for $(La,Sr)MnO_{3-\delta}$ and are similar to those for LSCF cathode material. Besides, oxides $RBaMn_2O_{5+\delta}$ are characterized by phase stability over a wide oxygen partial pressure range.[74] Zhang *et al.*[172] proposed layered perovskite $SmBaMn_2O_{5+\delta}$ (SBM) as electrode material for S-SOFCs. This oxide remains stable under both reducing and oxidizing atmosphere at high temperatures. Besides, it exhibits high electrical conductivity in air and in a Ar + H_2 (5%) mixture in the temperature range of 750–900 °C (see Table 8) and shows good electrochemical activity in oxygen reduction and hydrogen oxidation (in air and under wet hydrogen atmosphere, R_η is 0.066 and 0.314 Ω cm^2, respectively, at 900 °C; see Table 9). The power density of the LSGM electrolyte-supported fuel cell with SBM as the symmetrical electrode at 900 °C is as high as 782 mW cm^{-2} with hydrogen as the fuel.

Sengodan *et al.*[169] were the first to demonstrate that double perovskite $PrBaMn_2O_{5+\delta}$ (PBM) can be used as anode material for SOFCs. In order to provide carbon and hydrogen sulfide poisoning tolerance of electrodes and good electrochemical characteristics of SOFC fed with hydrocarbon fuel, the authors created new anode material based on PBM. The advantages of this material are high thermal and chemical stability under reducing atmosphere,[176, 177] total electrical conductivity and oxygen ion conductivity (see Table 8).

Choi *et al.*[171] modified the chemical composition of PMB by the partial replacement of Ba^{2+} ions with Ca^{2+} cations and prepared the new material $PrBa_{0.8}Ca_{0.2}Mn_2O_{5+\delta}$ (PBCM). It showed phase stability under reducing atmosphere (see Table 8), which made it possible to test this material as an electrode in LSGM electrolyte-supported S-SOFC. The maximum power density of S-SOFC, which contained the LGSM electrolyte layer with a thickness of ~250 μm and was prepared by the infiltration of the porous electrode layer with cobalt and iron nitrate solutions followed by annealing in air, was 1101 mW cm^{-2} at 800 °C; in the case of hydrocarbon fuels, namely, humidified C_3H_8 and C_8H_{18}, the maximum power density was 740 and 470 mW cm^{-2}, respectively. These characteristics are among the best achieved to date.

Zhao *et al.*[170] modified the chemical composition of PMB by the partial replacement of manganese ions by iron cations according to the formula $PrBaMn_{1.5}Fe_{0.5}O_{5+\delta}$ (PBMF). The electrical conductivity of PBMF in air was higher than that of PBM, and this material was resistant to contact with LSGM and showed good thermo-mechanical compatibility with LSGM (see Table 8). The maximum power density of 540 mW cm^{-2} at 800 °C was achieved for S-SOFCs with PBMF electrode material and 520 μm-thick LSGM electrolyte using wet hydrogen as the fuel. This power density is smaller than that achieved with PBCM, which is apparently because the thickness of LSGM electrolyte is more than two times larger. It should be noted that PBMF electrode material fed with hydrocarbon fuel showed good redox stability and high carbon tolerance.

Kim *et al.*[178] examined the possibility of using oxide $PrBaMn_{1.7}Co_{0.3}O_{5+\delta}$ (PBMCo) as electrode material for pseudosymmetrical SOFC, assuming that PBMCo should decompose under reducing atmosphere to form cobalt metal and should retain the initial structure in air. This material for S-SOFCs showed promising electrochemical characteristics: the power density of 1100 mW cm^{-2} at 800 °C and good operational lifetime over 100 h.

As electrode material for S-SOFC, Gu *et al.*[174] proposed PBM-based composite material modified by Pr_6O_{11} (Pr-PBM). Praseodymium oxide was added as an electrocatalyst through infiltration of a praseodymium nitrate solution into the porous PBM cathode and anode layers followed by annealing. The R_η values for Pr-PBM electrode material under both oxidizing and reducing atmosphere are given in Table 9. It is seen that the polarization resistance of Pr-PBM under reducing atmosphere is higher than that of SFM-based electrode material[143] (see Table 6), the cathode polarization resistance is much higher than that of LSCF (0.064 Ω cm^2 at 800 °C in air[179]). At 800 °C, the power density of S-SOFC with YSZ electrolyte and the GDC protective layer was 423 and 227 mW cm^{-2} using wet hydrogen and methane as the fuel (see Table 10). The authors mentioned carbon tolerance of the anode when using methane as the fuel source.

Therefore, among chromium- and manganese-containing perovskites, oxides $RBaMn_2O_{5+\delta}$, where R is a rare-earth element, with the double perovskite structure, are of most interest as electrode materials for S-SOFCs. These oxides are characterized by the highest power densities (> 1000 mW cm^{-2}). However, these oxides contain barium cations, making materials susceptible to different types of chemical degradation, resulting in the formation

of $BaCO_3$ on the cathode surface and a possible chemical reaction with electrolyte material. Hence, particular attention should be given to investigation of the lifetime of S-SOFCs with such electrode materials.

6.4. Materials based on oxides with the K_2NiF_4 structure

Oxides with the K_2NiF_4 structure (Fig. 7 *a*) have attracted attention as promising electrode materials for S-SOFCs due to the presence of a rock salt unit in their crystal structures. This unit has anion vacancies through which oxygen ions can diffuse. These oxides can have high oxygen-ion conductivity and, consequently, they are highly efficient in the cathode reaction, particularly in the moderate temperature range. Main examples are nickelates $R_2NiO_{4+\delta}$, where R = La, Pr and Nd. In this series, $Pr_2NiO_{4+\delta}$ has the highest oxygen-ion conductivity.[82] Cathode materials based on $Pr_2NiO_{4+\delta}$ are characterized by very low polarization resistance of the cathode/electrolyte interface even at 600 °C (0.08 Ω cm^2), and the model fuel cells with this material show a power density of ~400 mW cm^{-2}.[180]

Oxides $R_2NiO_{4+\delta}$, where R = La, Pr, were tested as electrode materials for S-SOFCs.[181,182] Taking into account low stability of nickelates $R_2NiO_{4+\delta}$ in anode gas atmosphere under operating conditions of S-SOFCs, these phases are reduced to form oxide R_2O_3 and nickel metal nanoparticles. Yang *et al.*[181] infiltrated $La_2NiO_{4+\delta}$ into porous LSGM or SDC layers that formed on the surface of the corresponding solid electrolyte membranes. The resulting model S-SOFCs showed a power density of ~550 mW cm^{-2} at 800 °C with wet hydrogen as the fuel. The short-duration testing demonstrated that the power output characteristics were stable for a period of 210 h.

Gao *et al.*[182] employed another approach. Thus, SDC solid electrolyte was infiltrated into the porous layer of $Pr_2NiO_{4+\delta}$ electrode material deposited on the gas-tight SDC membrane. Model S-SOFCs with $Pr_2NiO_{4+\delta}$–SDC (40 mass %) electrode material had the best power density characteristics (375 mW cm^{-2} at 800 °C, hydrogen as the fuel source). Symmetrical SOFCs showed the stability of cell voltage for 168 h and high cycling stability after switching hydrogen and air at the anode.

Unlike nickelates $R_2NiO_{4+\delta}$, manganites $La_xSr_{2-x}MnO_{4\pm\delta}$ exhibit phase stability in reducing atmosphere under operating conditions of SOFC. Manganite $La_{0.6}Sr_{1.4}MnO_{4\pm\delta}$ was tested as anode[183] and cathode[184] materials for SOFCs. Similar compositions with $x = 0.5$ and 0.6 were evaluated as electrode materials for S-SOFCs. These chemical compositions were chosen because they can be synthesized in air and have well-balanced characteristics (Table 11). These materials show stability under operating conditions of fuel cells in reducing atmosphere and in air. Their TEC values in air and under reducing atmosphere are comparable with the TEC values for conventional SOFC electrolytes. Besides, these materials have reasonable electrical conductivity in air. It was reported that $La_{0.5}Sr_{1.5}MnO_{4\pm\delta}$ reacts with YSZ and LSGM at 900 °C, but does not exhibit noticeable reactivity towards GDC up to 1300 °C.[190] The composite $La_{0.6}Sr_{1.4}MnO_{4\pm\delta}$ with a higher lanthanum content does not react with LSGM at 900 °C.[187] The main drawbacks of these materials are low electrical conductivity under reducing atmosphere (see Table 11), which is evidence that holes serve as the main charge carriers, and high polarization resistance of the electrode/electrolyte interface, particularly under reducing atmosphere (Table 12). This leads to a very low power density of S-SOFCs, lower than 70 mW cm^{-2} at 800 °C (Table 13).

It is worth noting that the surface modification of electrode material $La_{0.6}Sr_{1.4}MnO_{4\pm\delta}$ with such oxides as SDC and NiO[191] promotes a significant increase in the power density of S-SOFCs to 614 mW cm^{-2} at 800 °C using hydrogen as the fuel (see Table 13). This is primarily due to a decrease in the polarization resistance of the electrode/electrolyte interface at the cathode side of S-SOFCs (see Table 12). The produced S-SOFCs fed

Table 11. Electrical conductivities and TECs of electrode materials based on oxides with the K_2NiF_4 structure under oxidizing and reducing atmosphere (T = 800 °C).

Composition	Atmosphere	σ, S cm^{-1}	Thermal expansion		Ref.
			temperature range, °C	TEC × 10^6, K^{-1}	
$La_xSr_{2-x}MnO_{4\pm\delta}$ (x = 0.25–0.6)	Air	28.8 (x = 0.6)	25–800	12.3–12.9	185
	Air	38.6 (x = 0.25)	25–800	12.3–12.9	185
	Ar + H_2 (3%)	0.4 (x = 0.25)	25–800	13.7–13.8	185
	Ar + H_2 (3%)	1.9 (x = 0.5)	25–800	13.7–13.8	185
	Ar + H_2 (3%)	0.8 (x = 0.6)	25–800	13.7–13.8	185
$La_{0.5}Sr_{1.5}MnO_{4+\delta}$	Air	22.9	–	–	186
	Ar + H_2 (5%)	1.98	–	–	186
	Ar + H_2 (10%)	1.70	–	–	186
$(La_{0.5}Sr_{1.5}Mn)Ni_{0.1}O_{4+\delta}$	Air	18	–	–	186
$La_{0.6}Sr_{1.4}MnO_{4+\delta}$	Air	5.5	–	–	187
	Ar + H_2 (5%)	4×10^{-3}	–	–	187
$La_{0.6}Sr_{1.4}FeO_{4-\delta}$	Air	23	–	–	188
	Ar + H_2 (5%)	~0.018	–	–	188
$La_{1.4}Sr_{0.6}FeO_{4-\delta}$	Air	11	–	–	188
	Ar + H_2 (5%)	~0.007	–	–	188
$La_{0.8}Sr_{1.2}FeO_{4-\delta}$	Ar + H_2 (5%)	0.2	–	–	188
$La_{0.8}Sr_{1.2}Fe_{0.9}Co_{0.1}O_{4-\delta}$	Air	44.29	–	–	189
	Ar + H_2	0.032	–	–	189

Table 12. Polarization resistances of electrode materials based on oxides with the K_2NiF_4 structure under oxidizing and reducing atmosphere (T = 800°C).

Composition of the material	Electrolyte	Atmosphere	R_η, Ω cm^2	Ref.
$La_{0.5}Sr_{1.5}MnO_{4\pm\delta}$	YSZ/GDC	Air	1.2	185
	YSZ/GDC	Wet H_2	0.57	185
	YSZ/GDC	Air	1.32	190
	LSGM	Air	0.884	186
	LSGM	Ar + H_2 (5%)	8.7	186
$La_{0.5}Sr_{1.5}MnO_{4\pm\delta}$ – SDC	LSGM	Air	0.813	186
	LSGM	Ar + H_2 (5%)	5.99	186
$(La_{0.5}Sr_{1.5}Mn)Ni_{0.1}O_{4+\delta}$	LSGM	Air	0.676	186
	LSGM	Ar + H_2 (5%)	5.12	186
$(La_{0.5}Sr_{1.5}Mn)Ni_{0.1}O_{4+\delta}$ – SDC	LSGM	Air	0.603	186
	LSGM	Ar + H_2 (5%)	3.51	186
$La_{0.6}Sr_{1.4}MnO_{4+\delta}$	LSGM	Air	0.87	187
	LSGM	Ar + H_2 (5%)	2.07	187
$La_{0.6}Sr_{1.4}MnO_{4+\delta}$	SDC	Air	0.46	191
$La_{0.6}Sr_{1.4}MnO_{4+\delta}$ – NiO (90 : 10 mass %) [a]	SDC	Air	0.16	191
$La_{0.6}Sr_{1.4}MnO_{4+\delta}$ – SDC (80 : 20 mass %) [a]	SDC	Air	0.021	191
$La_{0.6}Sr_{1.4}MnO_{4+\delta}$ – SDC – NiO (70 : 20 : 10 mass %) [a]	SDC	Air	0.020	191
$La_{0.6}Sr_{1.4}MnO_{4+\delta}$ – SDC (20 : 80 mass %) [b]	SDC	Air	0.026	192
$La_{0.6}Sr_{1.4}MnO_{4+\delta}$ – SDC – NiO (20 : 75 : 5 mass %) [b]	SDC	Air	0.0099	192
$La_{0.6}Sr_{1.4}FeO_{4-\delta}$	LSGM	Air	1.85	188
	LSGM	Ar + H_2 (5%)	9.8	188
$La_{1.4}Sr_{0.6}FeO_{4-\delta}$	LSGM	Air	5.82	188
$La_{0.8}Sr_{1.2}FeO_{4-\delta}$	LSGM	Ar + H_2 (5%)	7.9	188
$La_{0.8}Sr_{1.2}Fe_{0.9}Co_{0.1}O_{4-\delta}$	LSGM	Air	0.29	189
	LSGM	N_2 + H_2 (5%)	1.14	
$La_{0.8}Sr_{1.2}Fe_{0.9}Co_{0.1}O_{4-\delta}$ – GDC (70 : 30 mass %)	LSGM	Air	0.21	189
	LSGM	N_2 + H_2 (5%)	0.93	189
$La_{0.8}Sr_{1.2}FeO_{4-\delta}$	LSGM	Air	1.27	189
	LSGM	N_2 + H_2 (5%)	4.01	189

[a] The porous layer of electrode material impregnated with NiO and(or) SDC. [b] The porous SDC layer impregnated with electrode material and NiO.

Table 13. Power densities of S-SOFCs with electrode materials based on oxides with the K_2NiF_4 structure (T = 800 °C, Ag as the current collector).

Composition of the material	Electrolyte	Fuel	P_{max}, mW cm^{-2}	L_e, μm	Ref.
$La_{0.5}Sr_{1.5}MnO_{4\pm\delta}$ – SDC (60 : 40 mass %)	LSGM	Wet H_2	30.7	300	186
$(La_{0.5}Sr_{1.5}Mn)Ni_{0.1}O_{4+\delta}$ – SDC (60 : 40 mass %)	LSGM	Wet H_2	126.7	300	186
	LSGM	CO + H_2 (1 : 2)	61.1	300	186
	LSGM	H_2 (H_2S 50 ppm)	81.3	300	186
$La_{0.6}Sr_{1.4}MnO_{4\pm\delta}$	LSGM	Wet H_2	59	1100	187
	SDC	H_2	67	300	191
$La_{0.6}Sr_{1.4}MnO_{4\pm\delta}$ – NiO (90 : 10 mass %) [a]	SDC	H_2	340	300	191
$La_{0.6}Sr_{1.4}MnO_{4\pm\delta}$ – SDC (80 : 20 mass %) [a]	SDC	H_2	294	300	191
	SDC	CH_4	32	300	191
$La_{0.6}Sr_{1.4}MnO_{4+\delta}$ – SDC – NiO (70 : 20 : 10 mass %) [a]	SDC	H_2	614	300	191
	SDC	CH_4	378	300	191
$La_{0.6}Sr_{1.4}MnO_{4+\delta}$ – SDC (20 : 80 mass %) [b]	SDC	H_2	479	300	192
$La_{0.6}Sr_{1.4}MnO_{4+\delta}$ – SDC – NiO (20 : 75 : 5 mass %) [b]	SDC	H_2	714	300	192
$La_{0.6}Sr_{1.4}FeO_{4-\delta}$ – LSGM (70 : 30 mass %)	LSGM	H_2	73	1100	188
$La_{0.8}Sr_{1.2}Fe_{0.9}Co_{0.1}O_{4-\delta}$	LSGM	Wet H_2	237	1000	189
$La_{0.8}Sr_{1.2}Fe_{0.9}Co_{0.1}O_{4-\delta}$ – GDC (70 : 30 mass %)	LSGM	Wet H_2	325	1000	189

[a] The porous layer of electrode material impregnated with NiO and(or) SDC. [b] The porous SDC layer impregnated with $La_{0.6}Sr_{1.4}MnO_{4+\delta}$ electrode material and NiO.

with methane as the fuel also showed rather high power density (378 mW cm^{-2} at 800 °C). Another efficient approach to improve the performance characteristics of S-SOFCs is based on the use of a porous layer of SDC electrolyte impregnated with $La_{0.6}Sr_{1.4}MnO_{4\pm\delta}$ and NiO as the electrode (see Tables 12 and 13).[192] This made it possible to increase the power density to 714 mW cm^{-2} at 800 °C using hydrogen as the fuel. However, these characteristics were much lower (104 mW cm^{-2} at the same temperature) in the case of methane as the fuel.

Ferrites of the composition $La_xSr_{2-x}FeO_{4-\delta}$, where $x = 0.6$, 0.8, 1.0, 1.2 and 1.4, also showed phase stability under reducing atmosphere [$Ar + H_2$ (5%)] at 850 °C[188] and were evaluated as electrode materials for S-SOFCs. These oxides have quite high electrical conductivity in air, which is much lower under reducing atmosphere (see Table 11). The polarization resistance of the $La_xSr_{2-x}FeO_{4-\delta}$/electrolyte interface in air is higher than that of electrode materials based on $La_xSr_{2-x}MnO_{4\pm\delta}$ (see Table 12). Meanwhile, an increase in the lanthanum content results in an increase in R_η at 800 °C in air from 1.85 (for $x = 0.6$) to 5.82 Ω cm^2 (for $x = 1.4$). Under reducing atmosphere, the polarization resistance of the electrode material/electrolyte interface sharply increases; the minimum R_η value (7.9 Ω cm^2) is observed for $x = 0.8$. This is indicative of low efficiency of single-phase $La_{0.8}Sr_{1.2}FeO_{4-\delta}$ as electrode material for S-SOFCs.

The study of model S-SOFC with electrode material based on the composite $La_{0.6}Sr_{1.4}FeO_{4-\delta}$–LSGM showed the power density of 73 mW cm^{-2} at 800 °C. Zhou *et al.*[189] found that the characteristics of $La_{0.8}Sr_{1.2}FeO_{4-\delta}$ can be improved by the replacement of 10% iron ions with cobalt cations (see Tables 11 and 12). The investigation of $La_{0.8}Sr_{1.2}Fe_{0.9}Co_{0.1}O_{4-\delta}$ under reducing atmosphere demonstrated the formation of cobalt metal nanoparticles (exsolution) on the oxide surface.[189] This modification of the composition and surface structure of electrode material leads to a significant decrease in R_η of the electrode/electrolyte interface in air and under reducing atmosphere (see Table 12). The power density of model S-SOFC increases to 237 mW cm^{-2} at 800 °C and can be increased to 325 mW cm^{-2} by using the composite $La_{0.8}Sr_{1.2}Fe_{0.9}Co_{0.1}O_{4-\delta}$–GDC as electrode material (see Table 13).

Therefore, single-phase ferrites and manganites with the K_2NiF_4 structure have no obvious advantages over materials based on perovskites. Moreover, these materials are characterized by low total electrical conductivity, while the oxygen ion conductivity, even if present, does not contribute to an increase in the electrochemical activity in electrode processes. Apparently, these issues can be addressed using new materials based on higher homologues of the Ruddlesden–Popper series.

6.5. Oxides with non-perovskite structures

Studies of oxides with non-perovskite structures as electrode materials are scarce. This is because most of these compounds do not meet the requirements for S-SOFC electrode materials. This primarily concerns the requirements for stability under reducing atmosphere of anode gases and high electrical conductivity. Several publications addressed pseudosymmetrical SOFCs with electrode materials based on non-perovskite d-metal oxides. For instance, Chen *et al.*[193,194] used $Ni_{0.7}Co_{0.3}O$–SDC and $LiNi_{0.8}Co_{0.15}Al_{0.05}O_2$ cermets as such materials. In this section, we consider rare examples of investigations of single-phase materials based on oxides with non-perovskite structures showing stability under operating conditions of SOFCs.

Ni *et al.*[195] investigated oxide $Fe_{0.5}Mg_{0.25}Ti_{0.25}Nb_{0.9}Mo_{0.1}O_{4-\delta}$ (FMTMN) with the α-PbO_2 structure as material for S-SOFCs (Fig. 15 *a*). This composition was chosen because one phase of $FeNbO_4$ with the α-PbO_2 structure has quite high electrical conductivity at room temperature (0.025 S cm^{-1}). The partial replacement of Fe^{3+} ions with Mg^{2+} and Ti^{4+} cations in the ratio Mg : Ti = 1 : 1 should enhance the phase stability under reducing atmosphere. The partial heterovalent replacement of Nb^{5+} ions with Mo^{6+} cations was performed for the same purpose. Oxide FMTMN showed stability under $Ar + H_2$ (5%) atmosphere at 750 °C and in the reaction with GDC at 1000 °C. It also has a small TEC value in air (8.6×10^{-6} K^{-1}). Under reducing atmosphere, the oxide showed significant chemical expansion during the first annealing cycle at > 600 °C. However, TEC of the reduced phase remained low (8.19×10^{-6} K^{-1}). The electrical conductivity of FMTMN at 750 °C is 0.025 and 0.29 S cm^{-1} in air and under reducing atmosphere, respectively. The polarization resistance of the FMTMN/GDC interface at 700 °C is quite large (3.9 Ω cm^2 in air and 13.4 Ω cm^2 under wet hydrogen atmosphere), which hinders the use of this material for S-SOFCs.

Oxides with the fluorite structure could be an alternative to oxides with the perovskite structure as electrode materials for S-SOFCs. This is particularly true for intermediate-temperature SOFCs because high oxygen ion conductivity of fluorite-like oxides should promote a significant decrease in polarization losses at the electrodes. However, such oxides are characterized by too low electronic conductivity. This drawback can be partially overcome by introducing d-block metal cations into the oxide structure to ensure the electronic conductivity through a decrease in the oxidation state of such metal cations. These phases include oxides $R_5Mo_3O_{16+\delta}$, where R = La–Tb, $\delta = 0$–0.5,[197,198] with the fluorite-like structure. The crystal structures of these phases contain isolated MoO_4 tetrahedra and R^{3+} cations in the cubic

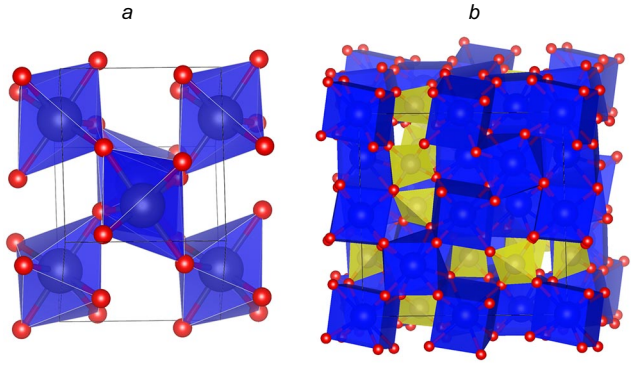


Figure 15. Crystal structures of α-PbO_2 (*a*) and $Pr_5Mo_3O_{16+\delta}$ (*b*). Lead cations are in blue octahedra; molybdenum cations are in yellow tetrahedra; praseodymium cations are in blue cubes. The Figure was prepared by the authors using the data of Refs 195 and 196.

coordination environment (Fig. 15 *b*). In the stoichiometric phase $R_5Mo_3O_{16}$ (R is a rare-earth metal cation in oxidation state +3), synthesized in air, the formal oxidation state of molybdenum is +5.67, which promotes the formation of hyperstoichiometric oxygen in the phase. The latter can occupy octahedral voids in the fluorite crystal structure. The maximum oxygen content is characterized by $\delta = 0.5$, which corresponds to oxidation state +6 of molybdenum cations.

It was shown [196, 199] that hyperstoichiometric oxygen is bound only to R^{3+} cations, thereby ensuring the appearance of oxygen ion conductivity in phases $R_5Mo_3O_{16+\delta}$, which reaches 10^{-2} S cm^{-1} at 700–900 °C.[200] It was found [201] that $Pr_5Mo_3O_{16+\delta}$ is stable under reducing Ar + H_2 (8%) atmosphere at 900 °C. It is worth noting that the annealing of $R_5Mo_3O_{16+\delta}$ under reducing atmosphere led to a decrease in the unit cell parameter,[198, 201] *i.e.*, the reduction is accompanied by the chemical contraction rather than expansion typical of oxides with the perovskite structure. Thus, under reducing atmosphere in the temperature range of 30–683 °C, the TEC value for $Pr_5Mo_3O_{16+\delta}$ is 9.4×10^{-6} K^{-1}, while at higher temperatures (725–900 °C), the linear sizes of the sample are smaller and TEC is -17.1×10^{-6} K^{-1}.[201] Under oxidizing conditions, the electrical conductivity of oxides $R_5Mo_3O_{16+\delta}$, associated primarily with oxygen ion conductivity, is $\sim 10^{-2}$ S cm^{-1} at 800 °C.[198, 200, 201] Under reducing atmosphere [Ar + H_2 (5%)], a considerable increase in the electrical conductivity of oxides is observed. The electrical conductivity of $Pr_5Mo_3O_{16+\delta}$ increases by two orders of magnitude ($\sigma \approx 1.2$ S cm^{-1} at 800 °C). Apparently, this is due to an increase in the concentration of charge carriers (electrons) upon reduction of molybdenum cations ($Mo^{+6} \rightarrow Mo^{+5}$).

Recently, it was shown [202] that the polarization resistance of the $Pr_5Mo_3O_{16+\delta}$/GDC interface at 800 °C is rather high (8.8 Ω cm^2 in air and 4.8 Ω cm^2 under reducing atmosphere). However, the use of composite materials $Pr_5Mo_3O_{16+\delta}$–Pr_6O_{11} (50 mass %) causes a decrease in R_η in air by more than an order of magnitude (to 0.6 Ω cm^2 at the same temperature). Therefore, oxides $R_5Mo_3O_{16+\delta}$ may be of interest as electrode materials for S-SOFCs in composites with Pr_6O_{11}.

7. Conclusion

Perovskite-like oxides containing manganese and iron cations are electrode materials of choice for S-SOFCs due to a combination of such properties as high stability, reasonable TEC values and high-temperature electrical conductivity under oxidizing and reducing atmosphere. The presence of two cations with different crystal chemical characteristics in oxides with the perovskite structure provides opportunities to vary practically important properties of such materials through iso- and heterovalent substitution of A and B cations.

Among single-phase compounds, double perovskites $RBaMn_2O_{5+\delta}$ (R are rare-earth elements) and iron-containing perovskites are of most interest as promising electrode materials for S-SOFCs. These compounds are characterized by high oxygen-ion conductivity and, consequently, electrode materials based on these compounds can show high electrochemical performance in S-SOFCs. It is worth noting that iron-containing electrode materials for S-SOFCs have recently attracted interest. However, thermodynamic stability of perovskite-like ferrites under reducing atmosphere at high temperatures is not sufficiently high. It can be enhanced by the partial heterovalent replacement of iron ions with cations with stable oxidation states under these conditions (Mg^{2+}, Sc^{3+}, Ti^{4+}, Nb^{5+}). Such single-phase electrode materials show high stability under reducing atmosphere and exhibit electrochemical activity in electrode processes in S-SOFCs. Besides, perovskites containing, apart from iron cations, molybdenum cations in B-sites deserve attention. The electrical conductivity of these perovskites increases several-fold under reducing atmosphere due to a change from p-type to n-type conductivity.

It should be noted that the nature of the single-phase materials is an obstacle to meeting all requirements for S-SOFC electrodes. As in the case of conventional SOFCs, this issue can be addressed using composite electrodes containing, apart from perovskite-like oxide, oxides with high oxygen-ion conductivity. The latter generally include solid electrolyte materials for SOFCs based on doped CeO_2 and stabilized ZrO_2 with the fluorite structure and also perovskite LSGM. In recent years, there has been a tendency to use efficient composite electrodes created by the infiltration (impregnation) of electroactive material particles into the porous support, which is produced using solid electrolyte or perovskite-like oxide materials.

Another approach to the production of composite electrodes for S-SOFCs, which has gained popularity in recent years, is based on the use of perovskites containing a small number of d metal B-site cations (*e.g.*, cobalt, nickel, copper, ruthenium, palladium), oxides of which are unstable at high temperature under reducing atmosphere of anode gases. These oxides belong to materials for pseudosymmetrical SOFCs, because they have different phase compositions at the cathode and anode sides due to the partial reduction of oxide at the anode. The reduction of oxide material particles on the surface affords metal or alloy nanoparticles (exsolution). The components thus prepared exhibit high electrochemical activity towards fuel oxidation. Besides, many oxides undergo reversible oxidation to form a phase with the perovskite structure upon a change from reducing to oxidizing atmosphere. This behaviour provides high stability of electrode material during the cycling of atmosphere at the anode.

Oxides that crystallize in structure types other than perovskite have been poorly studied as electrode materials for S-SOFCs, because most of these compounds do not meet the requirements for high electrical conductivity and thermodynamic stability simultaneously under reducing and oxidizing atmosphere. It should be noted that, taking into account a combination of properties, oxides $R_5Mo_3O_{16+\delta}$ (R = La, Nd, Pr) with fluorite-like structures may be of interest as potential electrode materials for S-SOFCs. This example offers hope that the search for new materials based on oxides with non-perovskite structures can lead to success.

Hence, it can be concluded that, in terms of their properties, iron- and manganese-containing perovskites meet, to a large extent, the main requirements for using S-SOFC electrode materials. However, the operating lifetime of these materials remains a challenging problem because laboratory tests are generally limited to a few hundred hours. Nevertheless, due to extensive studies

aimed at improving the properties of known electrode materials and searching for new compounds, it would be expected that new S-SOFC-based power devices will be available in the market in the near future.

This review was written with the financial support of the Russian Foundation for Basic Research (Grant No. 19-13-50240).

8. List of acronyms and designations

BZCY — $BaZr_{0.1}Ce_{0.7}Y_{0.2}O_{3-\delta}$ electrolyte,
CN — coordination number,
EASs — electrochemically active sites,
FMTMN — $Fe_{0.5}Mg_{0.25}Ti_{0.25}Nb_{0.9}Mo_{0.1}O_{4-\delta}$ electrode material,
GDC — $Ce_{0.9}Gd_{0.1}O_{2-\delta}$ electrolyte,
LCO — $La_{0.4}Ce_{0.6}O_{2-\delta}$ electrolyte,
LHB — lower Hubbard band,
LPG — liquefied petroleum gas,
LSCCM — $La_{0.75}Sr_{0.125}Ce_{0.125}Cr_{0.5}Mn_{0.5}O_{3-\delta}$ electrode material,
LSCF — $La_{0.6}Sr_{0.4}Co_{0.2}Fe_{0.8}O_{3-\delta}$ cathode material,
LSCM — $La_{0.75}Sr_{0.25}Cr_{0.5}Mn_{0.5}O_3$ electrode material,
LSGM — $La_{0.9}Sr_{0.1}Ga_{0.8}Mg_{0.2}O_{2.85}$ electrolyte,
LSM — $La_{1-x}Sr_xMnO_{3-\delta}$ cathode material,
LSSM — $La_{0.8}Sr_{0.2}Sc_{0.2}Mn_{0.8}O_{3-\delta}$ electrode material,
LSTF — $La_{0.3}Sr_{0.7}Ti_{0.3}Fe_{0.7}O_3$ electrode material,
L72S18SM — $(La_{0.8}Sr_{0.2})_{0.9}Sc_{0.2}Mn_{0.8}O_{3-\delta}$ electrode material,
L72S18SMR — $(La_{0.8}Sr_{0.2})_{0.9}Sc_{0.2}Mn_{0.75}Ru_{0.05}O_{3-\delta}$ electrode material,
OCV — open circuit voltage,
PBCM — $PrBa_{0.8}Ca_{0.2}Mn_2O_{5+\delta}$ electrode material,
PBF — $PrBaFe_2O_{5+\delta}$ electrode material,
PBFN — $PrBaFe_{1.6}Ni_{0.4}O_{5+\delta}$ electrode material,
PBFSc — $PrBa(Fe_{0.8}Sc_{0.2})_2O_{5+\delta}$ electrode material,
PBM — $PrBaMn_2O_{5+\delta}$ electrode material,
PBMCo — $PrBaMn_{1.7}Co_{0.3}O_{5+\delta}$ electrode material,
PBMF — $PrBaMn_{1.5}Fe_{0.5}O_{5+\delta}$ electrode material,
Pr-PBM — Pr_6O_{11}-modified $PrBaMn_2O_{5+\delta}$ electrode material,
SBM — $SmBaMn_2O_{5+\delta}$ electrode material,
SCM — $Sr_2Co_{1+x}Mo_{1-x}O_{6-\delta}$ electrode material,
SDC — $Ce_{0.8}Sm_{0.2}O_{2-\delta}$ electrolyte,
SFCM — $Sr_2Fe_{1.5-x}Co_xMo_{0.5}O_{6-\delta}$ electrode material,
SFM — $Sr_2Fe_{1.5}Mo_{0.5}O_{6-\delta}$ electrode material,
SFNbM — $Sr_2Fe_{1.4}Nb_{0.1}Mo_{0.5}O_{6-\delta}$,
SOFC — solid oxide fuel cell,
S-SOFC — symmetrical solid oxide fuel cell,
SSZ — $Zr_{0.8}Sc_{0.2}O_{1.9}$ electrolyte,
TEC — thermal expansion coefficient,
TPB — triple phase boundary,
UHB — upper Hubbard band,
YSZ — $Zr_{0.84}Y_{0.16}O_{1.92}$ electrolyte,
a_h — unit cell parameter of cubic perovskite,
a_h, c_h — hexagonal unit cell parameters,
a_o, b_o, c_o — orthorhombic unit cell parameters,
D^* — oxygen diffusion coefficient determined by secondary ion mass spectrometry combined with $^{18}O_2$ isotope labeling,
L_e — electrolyte thickness,
P_{max} — maximum power density,
r_A — ionic radius of the A cation,
r_B — ionic radius of the B cation,
r_O — ionic radius of oxide-ion,
R_η — polarization resistance of the electrode material/electrolyte interface,
T — temperature,
σ — specific electrical conductivity.

References

1. S.C.Singhal, K.Kendall. In *High Temperature Solid Oxide Fuel Cells: Fundamentals, Design and Applications*. (Eds S.C.Singhal, K.Kendall). (Oxford: Elsevier, 2003). P. 1
2. J.C.Larminie, A.Dicks. *Fuel Cell Systems Explained*. (New York: Wiley, 2003)
3. *Solid Oxide Fuel Cells*. https://www.energy.gov/fe/science-innovation/clean-coal-research/solid-oxide-fuel-cells (last accessed 25.05.2021)
4. *Report to Congress on Status of Solid Oxide Fuel Cell Program*. https://www.energy.gov/sites/prod/files/2019/09/f66/EXEC-2019-002655_Signed%20Report%201.pdf (last accessed 25.05.2021)
5. Q.Fang, L.Blum, D.Stolten. *ECS Trans.*, **91**, 687 (2019)
6. C.Su, W.Wang, M.Liu, M.O.Tadé, Z. Shao. *Adv. Energy Mater.*, **5**, 1500188 (2015)
7. J.C.Ruiz-Morales, D.Marrero-Lopez, J. Canales-Vazquez, J.T.A.Irvine. *RSC Adv.*, **1**, 1403 (2011)
8. P.I.Cowin, C.T.Petit, R.Lan, J.T.Irvine, S.Tao. *Adv. Energy Mater.*, **1**, 314 (2011)
9. X.-M.Ge, S.-H.Chan, Q.-L.Liu, Q.Sun. *Adv. Energy Mater.*, **2**, 1156 (2012)
10. S.Ya.Istomin, E.V.Antipov. *Russ. Chem. Rev.*, **82**, 686 (2013)
11. N.Q.Minh. *J. Am. Ceram. Soc.*, **76**, 563 (1993)
12. N.Q.Minh, T.Takahashi. *Science and Technology of Ceramic Fuel Cells*. (Amsterdam: Elsevier, 1995)
13. J.A.Kilner, M.Burriel. *Annu. Rev. Mater. Res.*, **44**, 365 (2014)
14. B.C.H.Steele, A.Heinzel. *Nature (London)*, **414**, 345 (2001)
15. Y.Takeda, R.Kanno, M.Noda, Y.Tomida, O.Yamamoto. *J. Electrochem. Soc.*, **134**, 2656 (1987)
16. E.Siebert, A.Hammouche, M.Kleitz. *Electrochim. Acta*, **40**, 1741 (1995)
17. S.B.Adler, J.A.Lane, B.C.H.Steele. *J. Electrochem. Soc.*, **143**, 3554 (1996)
18. S.B.Adler. *Chem. Rev.*, **104**, 4791 (2004)
19. L.Shu, J.Sunarso, S.S.Hashim, J.Mao, W.Zhou, F.Liang. *Int. J. Hydrogen Energy*, **44**, 31275 (2019)
20. S.Afroze, A.Karim, Q.Cheok, S.Eriksson, A.K.Azad. *Front. Energy*, **13**, 770 (2019)
21. E.J.L.Schouler, M.Kleitz. *J. Electrochem. Soc.*, **134**, 1045 (1987)
22. T.Setoguchi, K.Okamoto, K.Eguchi, H.Arai. *J. Electrochem. Soc.*, **139**, 2875 (1992)
23. T.Inoue, T.Setoguchi, K.Eguchi, H.Arai. *Solid State Ionics*, **35**, 285 (1989)
24. S.P.Jiang, S.P.S.Badwal. *J. Electrochem. Soc.*, **144**, 3777 (1997)
25. X.M.Ge, S.H.Chan, Q.L.Liu, Q.Sun. *Adv. Energy Mater.*, **2**, 1156 (2012)
26. T.Kenjo, S.Osawa, K.Fujikawa. *J. Electrochem. Soc.*, **138**, 349 (1991)

27. C.W.Tanner, K.Z.Fung, A.V.Virkar. *J. Electrochem. Soc.*, **144**, 21 (1997)
28. D.Ding, X. Li, S.Y.Lai, K.Gerdes, M.Liu. *Energy Environ. Sci.*, **7**, 552 (2014)
29. C.Nicollet, A.Flura, V.Vibhu, A.Rougier, J.M.Bassat, J.C.Grenier. *J. Power Sources*, **294**, 473 (2015)
30. J.G.Railsback, Z.Gao, S.A.Barnett. *Solid State Ionics*, **274**, 134 (2015)
31. K.J.Yoon, M.Biswas, H.Kim, M.Park, J.Hong, H.Kim, J.Son, J.Lee, B.Kim, H.Lee. *Nano Energy*, **36**, 9 (2017)
32. A.Chrzan, S.Ovtar, P.Jasinski, M.Chen, A.Hauch. *J. Power Sources*, **353**, 67 (2017)
33. M.Cassidy. *WIREs Energy Environ.*, **6**, e248 (2017)
34. A.Chrzan, J.Karczewski, M.Gazda, D.Szymczewska, P.Jasinski. *J. Eur. Ceram. Soc.*, **37**, 3559 (2017)
35. A.Giuliano, M.P.Carpanese, D.Clematis, M.Boaro, A.Pappacena, F.Deganello, L.F.Liotta, A.Barbuccia. *J. Electrochem. Soc.*, **164**, F3114 (2017)
36. P.A.Connor, X.Yue, C.D.Savaniu, R.Price, G.Triantafyllou, M.Cassidy, G.Kerherve, D.J. Payne, R.C.Maher, L.F.Cohen, R.I.Tomov, B.A.Glowacki, R.V.Kumar, J.T.S.Irvine. *Adv. Energy Mater.*, **8**, 1800120 (2018)
37. A.F.Wells. *Structural Inorganic Chemistry*. (Oxford: Oxford University Press, 1975)
38. R.H.Mitchell. *Perovskites Modern and Ancient*. (Thunder Bay, Ontario: Almaz Press, 2002)
39. R.J.D.Tilley. *Perovskites: Structure – Property Relationships*. (Wiley, 2016)
40. V.M.Goldschmidt. *Naturwissenschaften*, **14**, 477 (1926)
41. A.M.Glazer. *Acta Crystallogr., Sect. B*, **28**, 3384 (1972)
42. K.A.Aleksandrov. *Kristallografiya*, **21**, 249 (1976)
43. P.M.Woodward. *Acta Crystallogr., Sect. B*, **53**, 32 (1997)
44. C.J.Howard, H.T.Stokes. *Acta Crystallogr., Sect. B*, **54**, 782 (1998)
45. M.W.Lufaso, P.M.Woodward. *Acta Crystallogr. Sect. B*, **57**, 725 (2001)
46. J.-S.Zhou, J.B.Goodenough. *Phys. Rev. Lett.*, **94**, 065501 (2005)
47. G.Thornton, B.C.Tofield, A.W.Hewat. *J. Solid State Chem.*, **61**, 301 (1986)
48. J.L.García-Muñoz, J.Rodríguez-Carvajal, P.Lacorre, J.B.Torrance. *Phys. Rev. B*, **46**, 4414 (1992)
49. R.P.Liferovich, R.H.Mitchell. *J. Solid State Chem.*, **177**, 2188 (2004)
50. M.Cwik, F.Bouree, T.Lorenz, J.Baier, R.Mueller, G.Andre, F.Lichtenberg, M.Braden, E.Mueller-Hartmann, R.Schmitz, A.Freimuth. *Phys. Rev. B*, **68**, 060401(R) (2003)
51. P.Bordet, C.Chaillout, M.Marezio, Q.Huang, A.Santoro, S.-W.Cheong, H.Takagi, C.S.Oglesby, B.Batlogg. *J. Solid State Chem.*, **106**, 253 (1993)
52. K.Oikawa, T.Kamiyama, T.Hashimoto, Y.Shimojyo, Y.Morii. *J. Solid State Chem.*, **154** 524 (2000)
53. J.Rodriguez-Carvajal, M.Hennion, F.Moussa, A.H.Moudden, L.Pinsard, A.Revcolevschi. *Phys. Rev. B*, **57**, 3189 (1998)
54. C.A.L.Dixon, C.M.Kavanagh, K.S.Knight, W.Kockelmann, F.D.Morrison, Ph. Lightfoot. *J. Solid State Chem.*, **230** 337 (2015)
55. J.A.Alonso, M.J.Martínez-Lope, M.T.Casais, M.T.Fernández-Díaz. *Inorg. Chem.*, **39**, 917 (2000)
56. E.J.Cussen, P.D.Battle. *Chem. Mater.*, **12**, 831 (2000)
57. J.J.Lander. *Acta Crystallogr.*, **4**, 148 (1951)
58. C.Felser, K.Yamaura, R.J.Cava. *J. Solid State Chem.*, **146**, 411 (1999)
59. J.J.Adkin, M.A.Hayward. *Chem. Mater.*, **19**, 755 (2007)
60. T.Negas, M.S.Roth. *J. Solid State Chem.*, **3**, 323 (1971)
61. G.King, P.M.Woodward. *J. Mater. Chem.*, **20**, 5785 (2010)
62. M.T.Anderson, K.B.Greenwood, G.A.Taylor, K.R.Poeppelmeier. *Prog. Solid State Chem.*, **22**, 197 (1993)
63. C.J.Howard, B.J.Kennedy, P.M.Woodward. *Acta Crystallogr., Sect. B*, **59**, 463 (2003)
64. M.Karppinen, H.Yamauchi. In *Frontiers in Magnetic Materials*. (Ed. A.V.Narlikar). (Berlin, Heidelberg: Springer, 2005). P. 153
65. G.Y.Liu, G.H.Rao, X.M.Feng, H.F.Yang, Z.W.Ouyang, W.F.Liu, J.K.Liang. *J. Alloys Compd.*, **42** 353 (2003)
66. J.P.Hodges, S.Short, J.D.Jorgensen, X.Xiong, B.Dabrowski, S.M.Mini, C.W.Kimball. *J. Solid State Chem.*, **151**, 190 (2000)
67. Y.Tsujimoto, C.Tassel, N.Hayashi, T.Watanabe, H.Kageyama, K.Yoshimura, M.Takano, M.Ceretti, C.Ritter, W.Paulus. *Nature (London)*, **450**, 1062 (2007)
68. E.V.Antipov, A.M.Abakumov, S.Ya.Istomin. *Inorg. Chem.*, **47**, 8543 (2008)
69. A.M.Abakumov, M.G.Rozova, B.P.Pavlyuk, M.V.Lobanov, E.V.Antipov, O.I.Lebedev, G.van Tendeloo, O.L.Ignatchik, E.A.Ovtchenkov, Yu.A.Koksharov, A.N.Vasil'ev. *J. Solid State Chem.*, **160**, 353 (2001)
70. A.M.Abakumov, M.G.Rozova, B.P.Pavlyuk, M.V.Lobanov, E.V.Antipov, O.I.Lebedev, G.van Tendeloo, D.V.Sheptyakov, A.M.Balagurov, F.Bouree. *J. Solid State Chem.*, **158**, 100 (2001)
71. C.Greaves, A.J. Jacobson, B.C.Toéeld, B.E.F.Fender. *Acta Crystallogr., Sect. B*, **31**, 641 (1975)
72. F.Bertaut, P.Blum, A.Sagnieres. *C.R. Acad. Sci.*, **244**, 2944 (1957)
73. R.D.Shannon. *Acta Crystallogr., Sect. A*, 32, 751 (1976)
74. A.C.Tomkiewicz, M.A.Tamimi, A.Huq, S.McIntosh. *J. Power Sources*, **330** 240 (2016)
75. A.C.Tomkiewicz, M.Meloni, S.McIntosh. *Solid State Ionics*, **260**, 55 (2014)
76. P.Karen, P.M.Woodward. *J. Mater. Chem.*, **9**, 789 (1998)
77. R.Frison, S.Poltier, M.Martin, K.Conder. *Nucl. Instrum. Methods Phys. Res., Sect. B*, 273, 142 (2012)
78. A.Tarancón, S.J.Skinner, R.J.Chater, F.Hernández-Ramírez, J.A.Kilner. *J. Mater. Chem.*, **17**, 3175 (2007)
79. R.K.Li, C.Greaves. *J. Solid State Chem.*, **153**, 34 (2000)
80. T.Broux, C.Prestipino, M.Bahout, O.Hernandez, D.Swain, S.Paofai, T.Hansen, C.Greaves. *Chem. Mater.*, **25**, 4053 (2013)
81. C.N.Munnings, S.J.Skinner, G.Amow, P.S.Whitfield, I.J.Davidson. *Solid State Ionics*, **176**, 1895 (2005)
82. E.Boehm, J.-M.Bassat, P.Dordor, F.Mauvy, J.-C.Grenier, P.Stevens. *Solid State Ionics*, **176**, 2717 (2005)
83. S.J.Skinner, J.A.Kilner. *Solid State Ionics*, **135**, 709 (2000)
84. J.Cheng, A.Navrotsky. *J. Mater. Res.*, **18**, 2501 (2003)
85. J.Cheng, A.Navrotsky, X.-D.Zhou, H.U.Anderson. *J. Mater. Res.*, **20**, 191 (2005)
86. Ch.Laberty, A.Navrotsky, C.N.R.Rao, P.Alphonse. *J. Solid State Chem.*, **145**, 77 (1999)

87. L.Rørmark, S.Stølen, K.Wiik, T.Grande. *J. Solid State Chem.*, **163**, 186 (2002)
88. H.Yokokawa, T.Kawada, M.Dokiya. *J. Am. Ceram. Soc.*, **72**, 152 (1989)
89. S.Stølen, E.Bakken, C.E.Mohn. *Phys. Chem. Chem. Phys.*, **8**, 429 (2006)
90. R.Hoffmann. *Solids and Surfaces: A Chemist's View of Bonding in Extended Structures*. (Willy-VCH, 1989)
91. J.B.Goodenough. In *Progress in Solid State Chemistry*. Vol. 5. (Ed. H.Reiss). (Pergamon Press, Oxford, 1971). P. 145
92. C.Yang, A.Grimaud. *Catalysts*, **7**, 149 (2017)
93. J.B.Torrance, P.Lacorre, A.I.Nazzal, E.J.Ansaldo, C.Niedermayer. *Phys. Rev. B*, **45**, 8209 (1992)
94. N.F.Mott. *Metal–Insulator Transition*. (American Physical Society, 1968)
95. J.Zaanen, G.A.Sawatzky, J.W.Allen. *Phys. Rev. Lett.*, **55**, 418 (1985)
96. A.E.Bocquet, T.Mizokawa, K.Morikawa, A.Fujimori, S.R.Barman, K.Maiti, D.D.Sarma, Y.Tokura, M.Onoda. *Phys. Rev. B*, **53**, 1161 (1996)
97. Y.-L.Lee, J.Kleis, J. Rossmeisl, Y.Shao-Horn, D.Morgan. *Energy Environ. Sci.*, **4**, 3966 (2011)
98. S.Ya.Istomin, V.V.Chernova, E.V.Antipov, M.V.Lobanov, I.A.Bobrikov, V.Yu.Yushankhai, A.M.Balagurov, K.Y.Hsu, J.-Y.Lin, J.M.Chen, J.F.Lee, O.S.Volkova, A.N.Vasiliev. *Eur. J. Inorg. Chem.*, 2942 (2016)
99. D.Tian, B.Lin, Y.Yang, Y.Chen, X.Lu, Z.Wang, W.Liu, E.Traversa. *Electrochim. Acta*, **208**, 318 (2016)
100. X.Liu, D.Han, Y.Zhou, X.Meng, H.Wu, J.Li, F.Zeng, Z.Zhan. *J. Power Sources*, **246**, 457 (2014)
101. Z.Yang, Y.Chen, C.Jin, G.Xiao, M.Han, F.Chen. *RSC Adv.*, **5**, 2702 (2015).
102. Q.Zhou, C.Yuan, D.Han, T.Luo, J. Li, Z.Zhan. *Electrochim. Acta*, **133**, 453 (2014).
103. S.Ya.Istomin, A.P.Ber, N.V.Lyskov, E.V.Antipov. *Russ. J. Inorg. Chem.*, **62**, 1021 (2017)
104. S.Ya.Istomin, A.V.Morozov, M.M.Abdullayev, M.Batuk, J.Hadermann, S.M.Kazakov, A.V.Sobolev, I.A.Presniakov, E.V.Antipov. *J. Solid State Chem.*, **258**, 1 (2018)
105. A.V.Morozov, S.Ya.Istomin, D.A.Strebkov, N.V.Lyskov, M.M.Abdulaev, E.V.Antipov. *Russ. J. Electrochem.*, **56**, 100 (2020)
106. W.Fan, Z.Sun, Y.Bai, K.Wu, Y.Cheng, *ACS Appl. Mater. Interfaces*, **11**, 23168 (2019)
107. B.Niu, F.Jin, T.Feng, L.Zhang, Y.Zhang, T.He. *Electrochim. Acta*, **270**, 174 (2018)
108. C.Lu, B.Niu, S.Yu, W.Yi, S.Luo, B.Xu, Y.Ji. *Electrochim. Acta*, **323**, 134857 (2019)
109. Y.Chen, Z.Cheng, Y.Yang, Q.Gu, D.Tian, X.Lu, W.Yu, B.Lin. *J. Power Sources*, **310**, 109 (2016)
110. J.Lu, Y.-M.Yin, J.Li, L.Xu, Z.-F.Ma. *Electrochem. Commun.*, **61**, 18 (2015)
111. L.Bian, C.Duan, L.Wang, R.O'Hayre, J.Cheng, K.-C.Chou. *J. Mater. Chem. A*, **5**, 15253 (2017)
112. Y.Tao, Y.Zhou, W.Li, J. Shao, L.Bai, X.Liu. *J. Alloys Compd.*, **741**, 1091 (2018)
113. X.Lu, Y.Yang, Y.Ding, Y.Chen, Q.Gu, D.Tian, W.Yu, B.Lin. *Electrochim. Acta*, **227**, 33 (2017)
114. P.Zhang, G.Guan, D.S.Khaerudini, X.Hao, M.Han, Y.Kasai, K.Sasagawa, A.Abudula. *J. Power Sources*, **248**, 163 (2014)
115. P.Zhang, G.Guan, D.S.Khaerudini, X.Hao, C.Xue, M.Han, Y.Kasai, A.Abudula. *J. Power Sources*, **276**, 347 (2015)
116. Z.Yang, Y.Chen, N.Xu, Y.Niu, M.Han, F.Chen. *J. Electrochem. Soc.*, **162**, F718 (2015)
117. N.Xu, T.Zhu, Z.Yang, M.Han. *J. Mater. Sci. Technol.*, **33**, 1329 (2017)
118. G.Yang, J.Shen, Y.Chen, M.O.Tadé, Z.Shao. *J. Power Sources*, **298**, 184 (2015)
119. V.A.Kolotygin, E.V.Tsipis, M.V.Patrikeev, A.I.Ivanov, V.V.Kharton. *Russ. J. Electrochem.*, **52**, 628 (2016)
120. W.Fan, Z.Sun, J.Wang, J.Zhou, K.Wu, Y.Cheng. *J. Power Sources*, **312**, 223 (2016)
121. X.Kong, X.Zhou, Y.Tian, X.Wu, J.Zhang, W.Zuo. *J. Power Sources*, **326**, 35 (2016)
122. Z.Cao, Y.Zhang, J.Miao, Z.Wang, Z.Lü, Y.Sui, X.Yu, Y.Sui, X.Huang, W.Jiang. *Int. J. Hydrogen Energy*, **40**, 16572 (2015)
123. W.Fan, Z.Sun, J.Zhou, K.Wu, Y.Cheng. *J. Power Sources*, **348**, 94 (2017)
124. W.He, X.Wu, F.Dong, M.Ni. *J. Power Sources*, **363**, 16 (2017)
125. D.Han, J.Liu, Y.-B.He, H.Wang, X.-Z.Zhang, S.-R.Wang. *Int. J. Hydrogen Energy*, **43**, 960 (2018)
126. X.Ding, H.Liu, Z.Gao, G.Hua, L.Wang, L.Ding, G.Yuan. *Int. J. Hydrogen Energy*, **42**, 24968 (2017)
127. X.Liu, E.Zhao, Z.Wang, K.Gao, Y.Xiong. *Ceram. Int.*, **43**, 10960 (2017)
128. Z.Yang, N.Xu, M.Han, F.Chen. *Int. J. Hydrogen Energy*, **39**, 7402 (2014)
129. N.Xu, T.Zhu, Z.Yang, M.Han. *Electrochim. Acta*, **265**, 259 (2018)
130. J.Shen, Y.Chen, G.Yang, W.Zhou, M.O.Tade, Z.Shao. *J. Power Sources*, **306** 92 (2016)
131. Z.Ma, C.Sun, C.Ma, H.Wu, Z.Zhan, L.Chen. *Chin. J. Catal.*, **37**, 1347 (2016)
132. Tao, J.Xie, Y.Wu, S.Wang. *Int. J. Hydrogen Energy*, **43**, 15423 (2018)
133. P.Zhang, G.Guan, D.S.Khaerudini, X.Hao, C.Xue, M.Han, Y.Kasai, A.Abudula. *J. Power Sources*, **266**, 241 (2014)
134. T.Zhu, Z.Yang, M.Han. *Fuel*, **161**, 168 (2015)
135. B.He, Z.Wang, L.Zhao, X.Pan, X.Wu, C.Xia. *J. Power Sources*, **241**, 627 (2013)
136. B.Niu, F.Jin, X.Yang, T.Feng, T.He. *Int. J. Hydrogen Energy*, **43**, 3280 (2018)
137. J.Xu, X.Zhou, J.Cheng, L.Pan, M.Wu, X.Dong, K.Sun. *Electrochim. Acta*, **257**, 64 (2017)
138. D.M.Bierschenk, J.M.Haag, K.R.Poeppelmeier, S.A.Barnett. *J. Electrochem. Soc.*, **160**, F90 (2013)
139. J.M.Haag, B.D.Madsen, S.A.Barnett, K.R.Poeppelmeier. *Electrochem. Solid State Let.*, **11**, B51 (2008)
140. B.A.Rosen. *Electrochem*, **1**, 32 (2020)
141. L.Zhang, C.Yang, A.I.Frenkel, S.Wang, G.Xiao, K.Brinkman, F.Chen. *J. Power Sources*, **262**, 421 (2014)
142. Z.Yang, J.Li, Y.Lin, J.Liu, F.Chen, M.Liu. *Nano Energy*, **11**, 704 (2015)
143. Q.Liu, X.Dong, G.Xiao, F.Zhao, F.Chen. *Adv. Mater.*, **22**, 5478 (2010)

144. G.Xiao, Q.Liu, F.Zhao, L.Zhang, C.Xia, F.Chen. *J. Electrochem. Soc.*, **158**, B455 (2011)
145. H.Li, Y.Tian, Z.Wang, F.Qie, Y.Li. *RSC Adv.*, **2**, 3857 (2012)
146. J.B.Goodenough, Y.H.Huang. *J. Power Sources*, **173**, 1 (2007)
147. G.Miao, C.Yuan, T.Chen, Y.Zhou, W.Zhan, S.Wang. *Int. J. Hydrogen Energy*, **41**, 1104 (2016)
148. M.Gou, R.Ren, W.Sun, C.Xu, X.Meng, Z.Wang, J.Qiao, K.Sun. *Ceram. Int.*, **45**, 15696 (2019)
149. T.Wei, Q.Zhang, Y.H.Huang, J.B.Goodenough. *J. Mater. Chem.*, **22**, 225 (2012)
150. Y.Song, Q.Zhong, W.Tan, C.Pan. *Electrochim. Acta*, **139**, 13 (2014)
151. D.A.Osinkin, S.M.Beresnev, N.I.Lobachevskaya. *Russ. J. Electrochem.*, **53**, 665 (2017)
152. C.Sun, R.Hui, J.Roller. *J. Solid State Electrochem.*, **14**, 1125 (2010)
153. D.A.Osinkin, S.M.Beresnev, N.M.Bogdanovich. *J. Power Sources*, **392**, 41 (2018)
154. X.Meng, X.Liu, D.Han, H.Wu, J.Li, Z.Zhan. *J. Power Sources*, **252**, 58 (2014)
155. J.Gao, X.Meng, T.Luo, H.Wu, Z.Zhan. *Int. J. Hydrogen Energy*, **42**, 18499 (2017)
156. Y.Li, S.Zou, J.Ju, C.Xia. *Solid State Ionics*, **319**, 98 (2018)
157. T.Suzuki, M.Awano, P.Jasinski, V.Petrovsky, H.-U.Anderson. *Solid State Ionics*, **177**, 2071 (2006)
158. Y.Song, Q.Zhong, D.Wang, Y.Xu, W.Tan. *Int. J. Hydrogen Energy*, **42**, 22266 (2017)
159. Y.Guo, T.Guo, S.Zhou, Y.Wu, H.Chen, X.Ou, Y.Ling. *Ceram. Int.*, **45**, 10969 (2019)
160. S.Uhlenbruck, F.Tietz. *Mater. Sci. Eng., B*, **107**, 277 (2004)
161. A.B.Muñoz-García, D.E.Bugaris, M.Pavone, J.P.Hodges, A.Huq, F.Chen, H.C.zur Loye, E.A.Carter. *J. Am. Chem. Soc.*, **134**, 6826 (2012)
162. Q.Zhang, T.Wei, Y.H.Huang. *J. Power Sources*, **198**, 59 (2012)
163. M.Roushanafshar, N.Yan, K.T.Chuang, J.L.Luo. *Appl. Catal., B*, **176**, 627 (2015)
164. X.Meng, D.Han, H.Wu, J.Li, Z.Zhan. *J. Power Sources*, **246**, 906 (2014)
165. Y.C.Zhou, X.Meng, X.J.Liu, X.Pan, J.L.Li, X.F.Ye, H.W.Nie, C.R.Xia, S.R.Wang, Z.L.Zhan. *J. Power Sources*, **267**, 148 (2014)
166. D.M.Bastidas, S.Tao, J.T.S.Irvine. *J. Mater. Chem.*, **16**, 1603 (2006)
167. Y.Song, Q.Zhong, W.Tan. *Int. J. Hydrogen Energy*, **39**, 13694 (2014)
168. J.Zhou, N.Wang, J.Cui, J.Wang, J.Yang, Z.Zong, Z.Zhang, Q.Chen, X.Zheng, K.Wu. *J. Alloys Compd.*, **792**, 1132 (2019)
169. S.Sengodan, S.Choi, A.Jun, T.H.Shin, Y.W.Ju, H.Y.Jeong, J.Shin, J.T.S.Irvine, G.Kim. *Nat. Mater.*, **14**, 205 (2015)
170. L.Zhao, K.Chen, Y.Liu, B.He. *J. Power Sources*, **342**, 313 (2017)
171. S.Choi, S.Sengodan, S.Park, Y.-W.Ju, J.Kim, J.Hyodo, H.Y.Jeong, T.Ishihara, G.Kim. *J. Mater. Chem. A*, **4**, 1747 (2016)
172. Y.Zhang, H.Zhao, Z.Du, K.Swierczek, Y.Li. *Chem. Mater.*, **31**, 3784 (2019)
173. X.Luo, Y.Yang, Y.Yang, D.Tian, X.Lu, Y.Chen, B.Huang, B.Lin. *Electrochim. Acta*, **260**, 121 (2018)
174. Y.Gu, Y.Zhang, Y.Zheng, H.Chen, L.Ge, L.Guo. *Appl. Catal., B*, **257**, 117868 (2019)
175. Y.Zheng, C.Zhang, R.Ran, R.Cai, Z.Shao, D.Farrusseng. *Acta Mater.*, **57**, 1165 (2009)
176. S.V.Trukhanov, L.S.Lobanovski, M.V.Bushinsky, V.V.Fedotova, I.O.Troyanchuk, A.V.Trukhanov, V.A.Ryzhov, H.Szymczak, R.Szymczak, M.Baran. *J. Phys. Condens. Matter*, **17**, 6495 (2005)
177. S.V.Trukhanov, A.V.Trukhanov, H.Szymczak, R.Szymczak, M.Baran. *J. Phys. Chem. Solids*, **67**, 675 (2006)
178. S.Kim, S.Lee, J.Kim, J.Shin, G.Kim. *Sci. Rep.*, **8**, 17149 (2018)
179. L.Nie, M.Liu, Y.Zhang, M.Liu. *J. Power Sources*, **195**, 4704 (2010)
180. C.Ferchaud, J.-C.Grenier, Y.Zhang-Steenwinkel, M.M.A.van Tuel, F.P.F.van Berkel, J.-M.Bassat. *J. Power Sources*, **196**, 1872 (2011)
181. G.Yang, C.Su, R.Ran, M.O.Tade, Z.Shao. *Energy Fuels*, **28**, 356 (2014)
182. Z.Gao, X.Ding, D.Ding, L.Ding, S.Zhang, G.Yuan. *Int. J. Hydrogen Energy*, **43**, 8953 (2018)
183. C.Jin, Z.Yang, H.Zheng, C.Yang, F.Chen. *Electrochem. Commun.*, **14**, 75 (2012)
184. L.Sun, L.Huo, H.Zhao, Q.Li, P.Christophe. *J. Power Sources*, **179**, 96 (2008)
185. M.V.Sandoval, C.Pirovano, E.Capoen, R.Jooris, F.Porcher, P.Roussel, G.H.Gauthier. *Int. J. Hydrogen Energy*, **42**, 21930 (2017)
186. Z.Xu, Y.Li, Y.Wan, S.Zhang, C.Xia. *J. Power Sources*, **425**, 153 (2019)
187. J.Zhou, G.Chen, K.Wu, Y.Cheng. *J. Power Sources*, **270**, 418 (2014)
188. J.Zhou, Y.Chen, G.Chen, K.Wu, Y.Cheng. *J. Alloys Compd.*, **647**, 778 (2015)
189. J.Zhou, T.-H.Shin, C.Ni, G.Chen, K.Wu, Y.Cheng, J.T.S.Irvine. *Chem. Mater.*, **28**, 2981 (2016)
190. M.V.Sandoval, C.Cárdenas, E.Capoen, C.Pirovano, P.Roussel, G.H.Gauthier. *Electrochim. Acta*, **304**, 415 (2019)
191. J.Shen, G.Yang, Z.Zhang, W.Zhou, W.Wang, Z.Shao. *J. Mater. Chem. A*, **4**, 10641 (2016)
192. J.Shen, G.Yang, Z.Zhang, M.O.Tadé, W.Zhou, Z.Shao. *J. Power Sources*, **342**, 644 (2017)
193. Y.Chen, Z.Cheng, Y.Yang, W.Yu, D.Tian, X.Lu, B.Lin. *Mater. Lett.*, **188**, 413 (2017)
194. G.Chen, W.Sun, Y.Luo, H.Liu, S.Geng, K.Yu, G.Liu. *Int. J. Hydrogen Energy*, **43**, 417 (2018)
195. C.Ni, J.Feng, J.Cui, J.Zhou, J.Ni. *J. Electrochem. Soc.*, **164**, F283 (2017)
196. A.M.Antipin, O.A.Alekseeva, N.I.Sorokina, A.N.Kuskova, V.V.Artemov, V.Y.Murzin, E.P.Kharitonava, E.A.Orlova, V.I.Voronkova. *Crystallogr. Rep.*, **60**, 640 (2015)
197. P.H.Hubert, P.Michel, A.Thozet. *C.R. Acad. Sci. Paris Ser.*, **276**, 1779 (1973)
198. M.Tsai, M.Greenblatt, W.H.McCarroll. *Chem. Mater.*, **1**, 253 (1989)
199. A.M.Antipin, N.I.Sorokina, O.A.Alekseeva, A.N.Kuskova, E.P.Kharitonova, E.I.Orlova, V.I.Voronkova. *Acta Crystallogr., Sect. B*, **71**, 186 (2015)

200. V.I.Voronkova, I.A.Leonidov, E.P.Kharitonova, D.A.Belov, M.V.Patrakeev, O.N.Leonidova, V.L.Kozhevnikov. *J. Alloys Compd.*, **615**, 395 (2014)
201. S.Ya.Istomin, A.I.Kotova, N.V.Lyskov, G.N.Mazo, E.V.Antipov. *Russ. J. Inorg. Chem.*, **63**, 1291 (2018)
202. N.V.Lyskov, A.I.Kotova, S.Ya.Istomin, G.N.Mazo, E.V.Antipov. *Russ. J. Electrochem.*, **56**, 93 (2020)